Synchrotron Radiation Based Multi-Scale Structural Characterization of $CoPt_3$ Colloidal Nanoparticles

by

Ardalan Zargham

University of Bremen

2010

Synchrotron Radiation Based Multi-Scale Structural Characterization of $CoPt_3$ Colloidal Nanoparticles

Vom Fachbereich für Physik und Elektrotechnik
der Universität Bremen

zur Erlangung des akademischen Grades
Doktor der Naturwissenschaften
– Dr. rer. nat. –
genehmigte Dissertation

von

Dipl.-Ing. Ardalan Zargham

aus Teheran, Iran

1. Gutachter:	Prof. Dr. Jens Falta
2. Gutachter:	Prof. Dr. Marcus Bäumer
Eingereicht am:	17.06.2010
Tag des Promotionskolloquiums:	05.08.2010

The work described in this thesis has been performed in the Surface Science Group of Prof. Dr. J. Falta at the institute of Solid State Physics, University of Bremen, Germany.

Synchrotron Radiation Based Multi-Scale Structural Characterization of $CoPt_3$ Colloidal Nanoparticles

A dissertation submitted to the
Department of Physics and Electrical Engineering
of
University of Bremen

in partial fulfillment of the requirements for the degree of
Doctor of Natural Science
– Dr. rer. nat. –
in Solid State Physics

by

Ardalan Zargham

from Tehran, Iran

1. Examiner:	Prof. Dr. Jens Falta
2. Examiner:	Prof. Dr. Marcus Bäumer
Date of submission:	17.06.2010
Date of defense:	05.08.2010

The memory be green

W. Shakespeare,Hamlet

Abstract

Bimetallic $CoPt_3$ nanoparticles represent a category of colloidal nanoparticles with high application potentials in, e.g., heterogeneous catalysis, sensor technology, and magnetic storage media. Deposition of this system on functionalized supports delivers opportunities for controlled immobilization of the nanoparticles.

In this work, self-assembled monolayers (SAMs) of n-alkanethiol molecules served as functionalizing material for the Au covered Si substrates. Deposition of the ligand-terminated nanoparticles took place by means of spin and dip coating and has been optimized for each of the mentioned methods so that monolayers of nanoparticles on supports were fabricated with a well-controlled coverage

The morphology of the nanoparticle film arranged is addressed by grazing-incidence small angle x-ray scattering (GISAXS). This together with x-ray standing waves in total external reflection (TER-XSW) enables a 3D structural characterization of such nanoparticle films, so that the mean particle size, mean distance of the arranged nanoparticle films to the substrate, as well as the mean particle-particle distance in lateral direction have been determined.

TER-XSW, being an element-specific position-sensitive method, also reveals the elemental distribution of the particles which complementary provides a fundamental understanding of their internal structure. The $CoPt_3$ nanoparticles investigated here exhibit a core-shell-like structure with cores of $CoPt_3$ and shells mainly comprise Co. The results regarding the internal structure of the nanoparticles were then verified by extended X-ray absorption fine structure (EXAFS) measurements.

I sought in my heart to give you
the ivory letters that say "siempre"

F. G. Lorca, Gacela of Unforseen Love.

Acknowledgements

'Solitude is the profoundest fact of the human condition'. Yet, it is hardly possible to go through life all alone. Looking back to the last three years in the surface physics group and in Bremen, I always felt the warmth of support, and thus, feel obliged to express my gratitude to all those who shaped this period of my life.
Prof. Jens Falta has kindly accepted me in his group, helped me take the first steps toward a field of countless unknowns and let free, yet always backing up. With his exceptional understanding of research he taught me the possibility of unifying freedom and discipline.
I am also grateful to Prof. Marcus Bäumer for providing samples and many valuable discussions and suggestions. His never exhaustible will to search, research, and help is admirable.
I would have regretted it, if I had not known some people in life. Dr. Thomas Schmidt is one of the few. His extraordinary physical acumen together with an amazing brainpower and practical expertise makes him irreplaceable. It is a pleasure to thank Thomas for all the support during the beamtimes, all the discussions in the office, and his careful corrections and suggestions during manuscripts preparation as well as writing this thesis. 'Men of few words are the best men.'
I am thankful to Dr. Jan Ingo Flege and Dr. Edyta Piskorska-Hommel for fruitful discussions and ideas, to Radowan Hildebrand and Moritz Speckmann for many good shared hours and experiences during the beamtimes, to Susanne Müller-Schröter for her support, and to Jürgen Lauckner whose unbelievable understanding of the machines has always fascinated me.
I profited from the constructive cooperation with Torsten Laurus, Marc Sauerbrey, Sarah Röhe, and Aschkan Allahgholi. Without Torsten's help in EXAFS data analysis, Marc's in TER-XSW, Sarah's in coating processes and Aschkan's in XRR this work could have never find an end. Thanks for all the job we have done together.
Many thanks to all my colleagues for creating a comfortable atmosphere in our group.
I am very thankful to all my friends for all what they are.
I owe my deepest gratitude to my family, my magnificent parents, lovely brother and gorgeous sister. How could Words ever express my feelings to them. And last but not least, I am indebted to Solmaz for her love and endurance. Thank you.

Nothing is
But what is not.

W. Shakespeare, Macbeth

Preface

It has never been an easy task to evidence the existence of things. Nor has it been trivial to prove the converse, the nonexistence, even if seemingly less complicated. The barriers of being are hence subjectively limited to the empirical apperception of the observer. Sense organs, and to be more precise, apprehending of things by the sence organs, constitute the environment of the observer, so that, things begin to subjectively exist after having been discovered by the observer. Man observes, possibly due to an instinctual drive, to expand his territory. The drive knows no limits, nor does the observation; even if the sense organs reach their barriers, man moves on and utilizes things to discover more. The known turns out to be a medium of knowledge expansion regarding the yet nonexistent and the medium itself. Understanding light, for instance, tears it away from being nothing and embodies an existence in the first step. This, then, can be utilized to be able to take further steps, endeavoring further discoveries on the one hand and a better knowing of the light itself, on the other hand. The utilization of the known is stated as engineering.

Nano-engineering is an emerging area of scientifical importance in our age. Further, a large potential of diverse possible applications in this area is foreseen, and partially realized, which itself impels the science to keep track of it. In order to understand the behavior of structures as their dimensions approach the nanoscale, better characterization tools are a continuing need. In structural characterization of nano-sized objects, properties like chemical structure, atomic or molecular density, and uniformity and size are of interest. In case, the nano-sized objects are deposited on a substrate, in addition to the mentioned properties, the lateral and vertical ordering of the objects would also be of interest.

In this thesis both issues of fabricating nanostructures and their structural characterization are discussed, yet differently emphasized. Chapter 1, glimpsing some possible fabrication methods of nanostructures, introduces the $CoPt_3$ bimetallic nanoparticles taken as a basis here. The idea of depositing these nanoparticles on functionalized substrates is initiated and some possible deposition methods are described.

X-ray based methods delineate the main investigation tools for characterization of nanostructures in this thesis. Chapter 2 deals with theories of X-ray standing waves in total external reflection regime (TER-XSW), extended X-ray absorption fine structure (EXAFS) and grazing-incidence small-angle X-ray scattering (GISAXS). The variety of the performed methods shows the different questions addressed regarding the structure of the nanoparticles. While EXAFS reveals the atomic-scale structure of the nanoparticles, TER-XSW and GISAXS state mainly their vertical and lateral ordering after deposition, respectively.

Chapter 3, pursuing the general deposition ideas introduced in Chapter 1, deals with

experimental sample preparation. Two nanoparticle coating methods are compared with each other, after each has been optimized for our purposes.

The X-ray-based measurements within the scope of this thesis were performed at diverse synchrotron radiation facilities and different beamlines. Chapter 4 introduces the measurement setups and also delivers information about the data evaluation steps ranging from the mathematical models to the computer software codes developed.

The results of applying the mentioned methods to the introduced system are discussed in Chapter 5. This thesis presents the possibility of scanning the internal structure of deposited nanoparticles of size less than 10 nm by using TER-XSW. This demonstrates the strength and diverse application fields of TER-XSW far beyond being merely a yard stick.

And finally Chapter 6 gives an overview over the obtained results and proposes an outlook.

Contents

Chapter 1

Nanoparticles

1.1 Introduction

Quantum dots are of great scientific and technological interest since they can be considered to link between bulk materials and atomic and molecular structures since their properties are different from those of single atoms or molecules and simultaneously not the same as in bulk solids. The number of atoms on the crystal surface of structures in this size regime is a significant fraction of the total atom number in the crystal, and therefore have e.g. a higher chemical reactivity and lower melting temperatures. Due to the quantum size effect, the electrical, optical and magnetical properties of these particles are functions of their chemical composition and their size and are thus specifically tunable [1].

The ultimate method for fabrication of quantum dots should be able to produce monodisperse nanoparticles with a high size and shape control. There are different established techniques leading to different typologies of nanoparticles, from embedded into a matrix or grown onto a substrate to free standing ones, depending on the preparation method. Lithographically defined quantum dots are fabricated by confining a two-dimensional electron system, already composed by growing different materials on top each other using epitaxial methods. Quantum dot systems fabricated this way can be arranged laterally by local electrostatic depletion offering a relatively high degree of freedom for design of different structures by chosing electrode geometry [2, 3, 4], or vertically by etching away the structure around offering structures with very few electrons [5].

Epitaxially self-assembled quantum dots, which are nanometer size islands of semiconductor materials, are obtained by growing a thin layer of a material over another material with a significant lattice mismatch, using MBE[i] or MOCVD[ii] techniques [6, 7]. After having reached a critical thickness, the strained film formed during the growth makes a 2D to 3D transition due to this lattice mismatch (wetting layer), forming an array of nanometer-sized islands. This so-called Stranski-Krastanov regime leads to a partial release of the existing strain.

Colloidal quantum dots are synthesized chemically using wet chemistry and thus different from the systems introduced before, as it is possible to make free standing nanoparticles

[i] Molecular Beam Epitaxy
[ii] Metalorganic Chemical Vapour Deposition

in solution this way [8]. The fabrication of such nanoparticles is accomplished in a chemical reactor containing a liquid mixture of compounds responsible for growth control, whereas the atomic species forming the nanocrystals are introduced in form of precursors[iii] into the reactor. These precursors decompose after being introduced into the reactor due to energy gained by thermal collisions or chemical reactions and form monomers which nucleate and cause nanocrystal growth [9]. Controlled growth of the nanoparticles implies the existence of molecules in the reactor adsorbing on the surface of the growing nanocrystals. These so-called surfactant molecules should neither bind too strongly to the surface as they would then stop the growth process, nor too weakly, as an aggregation would then occur [10]. Having stopped the growth process, e.g. by lowering temperature in the reactor, the surfactants bind more strongly to the surface of nanoparticles and provide their solubility in solvents with the same polarity as of the surfactants' functional group. Furthermore, it is possible to carry out ligand exchange processes [11] or even remove the ligand shell temporarily [12]. Colloidal nanocrystals can be produced in large quantities in a reaction flask and, since dispersed in solution, they can later be transferred to any desired substrate.

1.2 Metallic Colloidal Nanoparticles

Colloidal metals and most specifically colloidal gold have attracted notable interest in ancient times due to their aesthetic value for making glass and ceramics as well as less documented alchemical and therapeutic properties [13].

The scientific age of metal colloids has begun with the experiments of Michael Faraday on gold sols[iv] in the nineteenth centruy, demonstrating the formation of colloidal gold solution by chloroaurate[v] solution reduction using phosphorus as reduction agent [14]. Faraday himself did not have the possibility to determine the size of the gold particles he produced. This was done by reproducing those preparations in Faraday's original laboratory in the late twentieth century, coming to the result that the so-produced solution contains particles of 3-30 nm in diameter [15].

Twentieth century begins with increasing interest and attention on preparation and investigation of colloidal metal sols. Ostwald's pioneering papers in 1907 have put the colloid science on a firm base [17]. Ostwald begins the description of colloidal state with imagining a metallic cube of one centimeter on each edge. By assuming approximate density, atomic weight and atomic diameter values for iron, as has been taken as an example, one comes to the conclusion that atoms residing on the surface of the cube would only be 10^{-5}% of the total number of atoms. By dividing the cube into smaller cubes the number of the surface atoms increases such that in case of deviding the original cube into 10^{18} cubes of 10 nm on each edge, the fraction of surface atoms would be 10% (c.f. Fig. 1.1). This geometric phenomenon is the basis for catalysis by dispersed supported metals.

Furthermore, Zsigmondy's physical investigations of colloidal solutions and his invention of ultramicroscope[vi] enabled to carry out precise studies on the effect of preparation

[iii] A *precursor* is a molecule or complex containing at least one required atom for the growth.

[iv] A *sol* is a colloidal suspension of solid particles in liquid.

[v] $[AuCl_4]^-$

[vi] The *ultramicroscope* is a system for observing the colloidal particles whose diameter is in the range of visible light wavelengths, and therefore can not be resolved by ordinary microscopes. Here, the colloidal

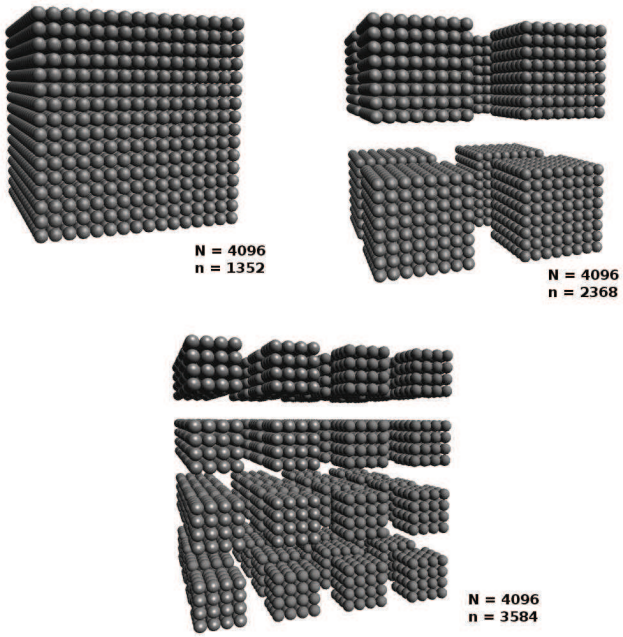

Figure 1.1: *Dividing a cube with 16 atoms on each side. N is the total atom number and n is the number of surface atoms. [16]*

conditions on particle size [18], which lead to a Chemistry Nobel Prize in 1925 [19].

Since Faraday's experiments, many different methods for preparation of colloidal metals have been developed ranging from electric arc between gold electrodes under water to action of carbon monoxide on chloroauric acid [20]. The particle size found for these colloids, depending on preparative conditions vary between 2-100 nm, mostly in the larger diameter range. But the interest in the intrinsic physics and chemistry of metal nanoparticles have been the propulsive force for establishment of a new synthetic metal colloid chemistry.

In the last years, many successful synthetical approaches for preparation of monodisperse metallic colloids with well-defined compositions have been introduced [21, 22, 23, 24, 25, 26].

Self-assembled ordered layers of such particles have got high application potential and can be employed, e.g., in heterogeneous catalysis[vii][27, 28, 29, 30], future generation magnetic data storage devices [31], or as sensors [32]. Especially in case of bimetallic colloids the chemical and physical properties of the particles have turned out to be very well adjustable. This makes, e.g., fabrication of corrosion-resistant magnetic particles or selective catalysts with large surfaces possible. The activity and selectivity of the particles in a catalytic active layer, as an example, can be adjusted by particle stoichiometry[viii] [30, 33]

solution in a light absorbing ambient is illuminated by a converging beam. Light hitting the colloid particles gets scattered and is then viewed through an optical microscope placed in a right angle to the light beam.

[vii] *Heterogeneous catalysis* is referred to as catalysis where the catalyst is in a different phase (i.e. solid, liquid, gas) than the reactants.

[viii] *Stoichiometry* (from Greek $\sigma\tau o\iota\chi\varepsilon\tilde{\iota}o\nu$, "element" and $\mu\acute{\varepsilon}\tau\rho o\nu$, "measure") descibes the quantitative (mass) relationships among elements in compounds.

as well as particle size and distance [27, 29, 34, 35, 36]. Furthermore, high monodispersity makes the self ordering of the particles into regular-ordered colloidal crystals on suitable substrates much easier [37, 38, 39]. This all describes the extraordinary importance of optimised control in fabrication of nanoparticles and their deposition on suitable supports into ordered layers.

1.2.1 Cobalt-Platinum Colloidal Nanoparticles

Bimetallic cobalt-platinum nanoparticles are due to their potential for application in catalysis as well as magnetic devices very well known and characterised [40, 41, 42, 43]. Thus, most of the investigations carried out within the framework of this thesis were based on the $CoPt_3$ system synthesized after a recipe of Shevchenko et al. [44, 45]. In this method the bimetallic nanoparticles are synthesized via simultaneous reduction of platinum(II)-acetylacetonate[ix] and thermodecomposition of cobalt carbonyl[x] at 220 °C under dry argon and in the presence of 1-adamantanecarboxylic acid[xi] and hexadecylamine[xii] as stabilizing agents. The size of the nanoparticles can be varied by controlling the experimental conditions like reaction temperature, concentration of stabilizing agents, ratio between cobalt and platinum precursors, etc. It has been shown [45] that the size of the nanoparticles can be then precisely tuned from ∼3 nm up to ∼18 nm in a predictable and reproducible way. After cooling down to room temperature, multiple washing and centrifugating with chloroform and isopropanol, the reaction mixture is precipitated and redissolved in hexane[xiii]. This mixture can then be stored stably for days due to the stabilizing effect of the ligands [46] . The stability time can be increased to a couple of weeks by cooling down the suspension. After prolonged storage, the particles precipitated on the container walls into a brown sediment and can not be redispersed again.

The crystal of bulk $CoPt_3$ is an fcc structure described by the space group $pm\overline{3}m$. In the unit cell the Pt atoms occupy the 3c sites $(0,\frac{1}{2},\frac{1}{2})$a, $(\frac{1}{2},0,\frac{1}{2})$a and $(\frac{1}{2},\frac{1}{2},0)$a and the Co atoms occupy the 1a site (0,0,0) with a unit cell dimension of $a = 3.8540$ Å [47] (cf. Fig. 1.2).

1.3 Deposition of Nanoparticles

Deposition of the colloidal nanoparticles, which are due to their synthetical manufacturing origin (cf. 1.2.1) in a liquid solvent, of enormous importance for characterization of these particles and subsequent device fabrication. Functionalizing the substrate delivers opportunities for controlled immobilization of the nanoparticles as interaction between the ligand shell and substrate functionalizing molecules influence the particle-particle distance

[ix] Pt-$(acac)_2$
[x] $Co_2(CO)_8$
[xi] 1-ACA
[xii] HDA
[xiii] In principal it is possible to take any nonpolar solvent, as the ligand shell is nonpolar. Here we took hexane due to its relatively high vapour pressure, and thus volatility, which turned out to be more suitable for subsequent coating processes (cf. 3.3.2)

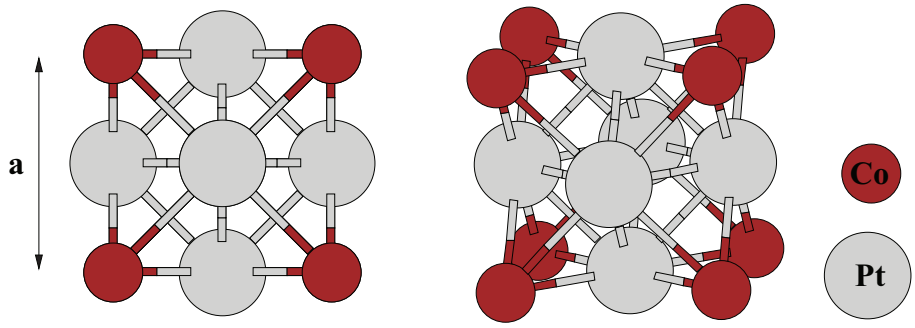

Figure 1.2: *$CoPt_3$ bulk fcc crystal structure with Co atoms on the corners and Pt atoms on the surfaces of the cube. The lattice constant of the unit cell is $a = 3.854$ Å.*

as well as the mean particle distance to the substrate.

1.3.1 Self-Assembled Monolayers

One easy and manifold possibility for substrate functionalization is the employment of self-assembled monolayers (SAMs). The ability to tailor both head and tail group of the SAM molecules make them versatilely applicable on different systems; while the head group has an affinity to the substrate the end group stands [48]. Fig. 1.3 shows an array of a self-assembled molecules into a monolayer with thiol[xiv] head groups and non-polar methyl[xv] end groups. Due to the easy preparation and well-defined order of thiol molecules on Au(1 1 1) substrate, this has become a model system for SAMs [49]. The (1 1 1) surface is the lowest-energy surface, and thus preferred in the growth of thin Au films. Its is relatively easy and inexpensive to prepare Au films and use them in applications instead of single crystals.

The self-assembled organic material employed within the scope of this thesis was hexadecanethiol[xvi] (HDT) on a commercially available standard 4 inch Si(1 0 0) substrate coated with 30 nm Au layer with nominal roughness of 1 nm on 9 nm Ti as adhesive layer [50] (cf. Fig. 1.4). HDT has got a molecule length of 24.5 Å [51]. After self-assembling, thiol head groups are covalently bound to Au atoms and the non-polar aliphatic chain stands upright with a tilt of about 30 ° from the surface normal [48, 52, 53, 54, 55]. This, thus, leads to an effective SAM thickness of about 21.22 Å. Due to the non-polar end groups of both organic ligands of the nanoparticles as well as HDT SAMs, the interaction between them is governed by van der Waals forces [xvii].

[xiv] A *thiol* is a compound that contains the functional group composed of a sulfur-hydrogen bond (-SH).
[xv] A *methyl* is a hydrophobic alkyl functional group with the formula -CH_3.
[xvi] $CH_3(CH_2)_{15}SH$
[xvii] In order to immobilize the nanoparticles, beside the already introduced non-polar van der Waals force, another method would be to take advantage of polar electrostatic interactions as well as complexation or covalent binding of the end groups of ligand shells and SAMs. This approach would eliminate the most prominent disadvantage of non-covalent immobilization of nanoparticles, which is the instability of the film due to their relatively weak mutual interaction. Conversely, the covalent binding of the nanoparticles with the SAMs, in case of appropriate choice of ligands and SAMs reactive groups, is expected to result

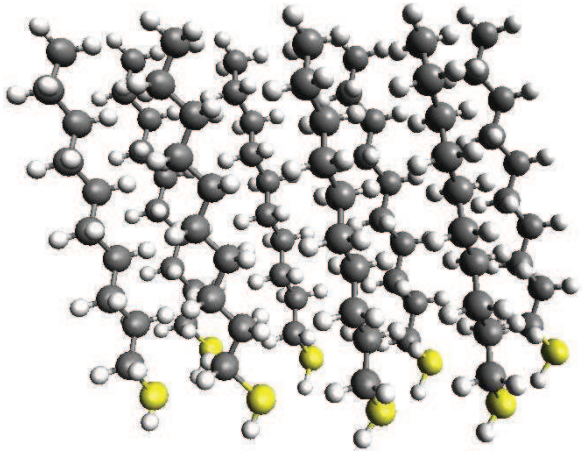

Figure 1.3: *Array of n-alkanethiol molecules self-assembeled on a substrate (not shown here).*

1.3.2 Spin Coating

One of the common methods of deposition and ordering control of nanoparticles on a support is spin coating. A spin coater is a machine consisting of a rotating disk connected to control electronics in order to regulate the rotation speed. After fixing a substrate on this disk a small amount of the solution planned to be coated is brought on top. During disk rotation the fluid spins off the edges of the substrate due to centripetal force. The applicable solvent is often volatile and evaporates while the disk rotates with a high angular speed. Thus, by controling the speed and amount of the applied solution the ordering can be controlled. Three different stages can be distinguished during the spin coating process:

- deposition
- acceleration
- spinning at a constant rate

Deposition of the solvent on the substrate can be performed without sample spinning or with sample spinning in a constant, relatively low velocity. At this stage two factors are of importance: providing the necessary amount of solvent and substrate wettability.

in high stability and specificity, significantly extending the realm of possible applications in future devices based on nanotechnology.

One of the possible approaches for making covalent links is the so-called Huisgen reaction [56], a subset of click reactions, which is distinguished by its relatively high yield and feasibility and sparse by-products. Generally, the reaction of an organic azide with an alkyne makes stable triazoles. By using alcanethiols and alcanethiols with terminal azides in a defined combination as SAM, the coverage of the surface with nanoparticles can precisely be tuned [57]. This is due to the fact that the azide terminated thiols are uniformly distributed on the surface because of sterical interactions .

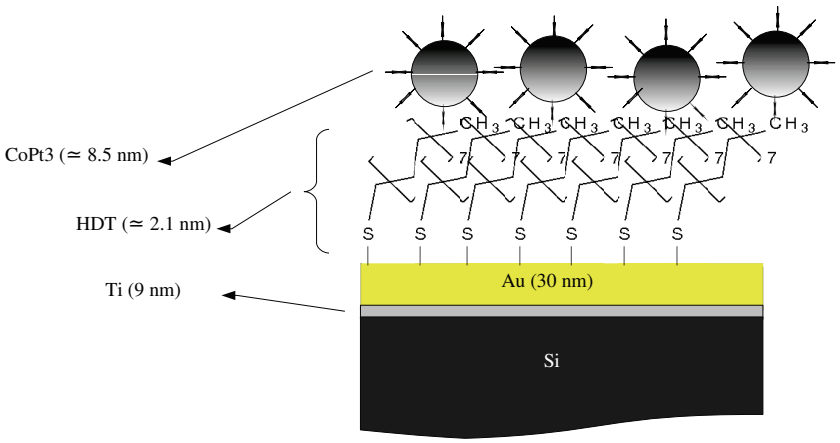

Figure 1.4: *Sketch of the structure characterized within the scope of this thesis. A Si substrate coated with Ti and Au and subsequently functionalized with HDT. The sketch also shows the $CoPt_3$ NPs on top of the mentioned sandwich structure.*

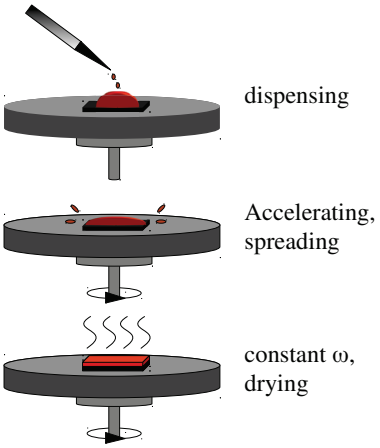

Figure 1.5: *Simplified scheme of a spin coating process in three steps.*

During the acceleration phase the substrate reaches its end spinning velocity. Our investigations have shown that the best results are obtained by using very low acceleration times (of about 1 s). This was the case in all investigations of this work.

During the last stage, spinning at constant rate, the solvents evaporates completely and the film reaches its final form.

1.3.3 Dip Coating

Dip coating is a method for preparation of thin films on substrates widely used in industy due to its simplicity and relatively high throughput. In this method substrates wettable by the sample solution are withdrawn from a liquid reservoir.

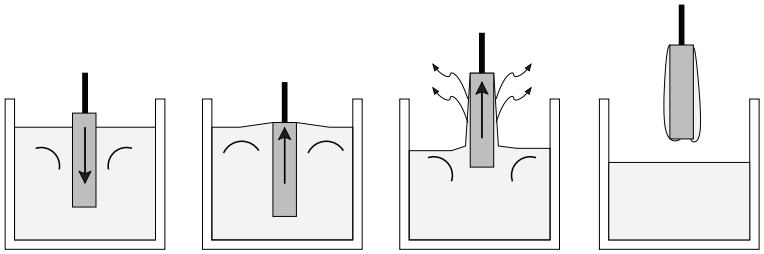

Figure 1.6: *Simplified scheme of a dip coating process in four steps. From left to right: immersion, start up, deposition and evaporation, drainage.*

The film preparation by dip coating can be devided into four steps:

- immersion
- start up
- deposition and evaporation
- drainage

A thin film of particle solution remains on the substrate surface during the dip coating. Then by evaporation of the solvent the particles are left on the substrate. Dewetting effects can cause formation of islands of particles on the surface and therefore has to be prevented. To avoid dewetting not only an appropriate combination of substrate and solution but also diffusion of nanoparticles across the substrate and forming self-assembled structures is necessary. In this respect, the concentration of surfactants has turned out to be important for particle self-assembly [58].

Chapter 2

Methods

In this chapter the theory and background of different experimental methods used in this thesis are discussed with the main focus on X-ray standing waves in total external reflection regime, abbreviated TER-XSW, because of two main reasons. First, this was the main method adapted and applied for the purpose of this work. Second, XSW in general, and TER-XSW in particular, are still not that common and still denoted as exotic, despite their mightiness in the field of X-ray characterization.

Furthermore, the theory of X-ray absorption fine structure (XAFS) and grazing incidence small angle X-ray scattering (GISAXS) as complementary X-ray methods will be briefly discussed.

2.1 X-ray Standing Waves in Total External Reflection (TER-XSW)

The X-ray standing wave technique provides an element-specific structural probe by using X-ray reflectivity to generate a two-beam interference field that in turn induces a spatial dependence to the x-ray spectroscopic yields from atoms within the field [59, 60]. While XSW generated by diffraction from a single crystal provides a high-resolution probe well-suited for atomic-scale structural determination, this XSW period is too small to profile larger, nano structures, and organic self-assembled multilayers. To extend the XSW technique to the nanoscale and beyond, one can employ a long-period XSW generated by total external reflection (TER) from a mirror surface [61, 62, 63, 64, 65, 66, 67] or generated by Bragg diffraction from a periodically layered synthetic microstructure (LSM) [68, 69, 70, 71, 72, 73, 74]. In this section the basic principals for understanding TER-XSW and finally the method itself as used in this work are introduced.

2.1.1 Introduction into Basic Principles

The interaction of electromagnetic waves with matter is described by the complex dielectric[i] polarizability $\chi(\mathbf{r},\omega)$ which can be expressed as

$$\chi(\mathbf{r},\omega) = \frac{r_0 N_A \lambda^2}{\pi A}\varrho_m(\mathbf{r})[f_0 + f'(\omega) - if''(\omega)]. \tag{2.1}$$

Here, r_0 is the classical electron radius, also known as Thomson scattering length, and is given by $r_0 = e^2/(4\pi\epsilon_0 m c_0^2) = 2.818 \times 10^{-5}$Å. Furthermore, N_A is Avogadro's number, λ the electromagnetic wavelength, A the molar atomic mass, and $\varrho_m(\mathbf{r})$ the mass density. f_0 is the atomic form factor and defined as

$$f_0 = \int \varrho_A(\mathbf{r}) e^{i\mathbf{q}\cdot\mathbf{r}} dV, \tag{2.2}$$

with $\varrho_A(\mathbf{r})$ the electron density of a single atom and $\mathbf{q}$ the wave vector transfer. $f'(\omega)$ and $f''(\omega)$ are energy dependent dispersion and absorption correction factors known as Hönl corrections [75]. These factors are interconnected by Kramers-Kronig relations[ii] and gain in importance at absorption edges.
In case of materials with more than a single atomic species Equation 2.1 loses its validity and a more general form has to be extracted. In this case of different atomic species k in the material, partial mass densities $\varrho_{m,k}$ replace the mentioned mass density with corresponding $f_{0,k}, f'_k, f''_k$ and partial molar atomic masses A_k, leading to

$$\chi(\mathbf{r},\omega) = \frac{r_0 N_A \lambda^2}{\pi}\sum_k \frac{\varrho_{m,k}(\mathbf{r})}{A_k}[f_{0,k} + f'_k(\omega) - if''_k(\omega)]. \tag{2.3}$$

Far away from absorption edges this expression can be simplified written as

$$\chi(\mathbf{r},\omega) = \chi(\mathbf{r}) = -r_0\frac{\lambda^2}{\pi}\varrho(\mathbf{r}), \tag{2.4}$$

with $\varrho(\mathbf{r})$ the electron density of the material. In case of a periodic crystal, it is clear that $\chi(\mathbf{r})$ can be expressed as a Fourier series over the reciprocal lattice as

$$\chi(\mathbf{r}) = \sum_{\mathbf{h}} \chi_{\mathbf{h}} e^{i\mathbf{h}\cdot\mathbf{r}}. \tag{2.5}$$

This can then be split into a constant part χ_0 (zeroth Fourier coefficient) and the local deviation $\Delta\chi(\mathbf{r})$ from it and be expressed as

$$\chi(\mathbf{r}) = \chi_0 + \Delta\chi(\mathbf{r}). \tag{2.6}$$

[i] Magnetic scattering or magneting dichroism can be described by complex magnetic polarizability which is not to be dealt with as not in the focus of this thesis.

[ii] For a complex function $\zeta(\omega) = \zeta_1(\omega) + i\zeta_2(\omega)$ the Kramers-Kronig relations are given by
$\zeta_1(\omega) = \frac{1}{\pi}\mathcal{P}\int_{-\infty}^{\infty}\frac{\zeta_2(\omega')}{\omega'-\omega}d\omega'$
and
$\zeta_2(\omega) = -\frac{1}{\pi}\mathcal{P}\int_{-\infty}^{\infty}\frac{\zeta_1(\omega')}{\omega'-\omega}d\omega'$
where $\mathcal{P}$ denotes the Cauchy principal value.

χ_0 represents the average polarizability value over the elementary unit cell of the crystal whereas $\Delta\chi(\mathbf{r})$ takes the crystalline structure into account. At small scattering angles, as the case in all experiments in this thesis, X-rays average over the elementary unit cell which leads to the determination that merely the constant part χ_0 of the polarizability $\chi(\mathbf{r})$ needs to be considered.
Scattering and refractive properties of matter can be interconnected via polarizability knowing that in general $n = (1+\chi)^{1/2}$, with n the complex refractive index. It also has to be considered that the typical values for $\Re(\chi)$ and $\Im(\chi)$ are in ranges of 10^{-5} and 10^{-7} units, respectively. Thus, in general according to Equation 2.1

$$n_0 = (1+\chi_0)^{1/2} \approx 1 + \frac{1}{2}\chi_0 = 1 - \delta + i\beta \tag{2.7}$$

with

$$\delta = \lambda^2 \frac{r_0 N_A \varrho_m}{2\pi A}(f_0 + f') \tag{2.8}$$

and

$$\beta = \lambda^2 \frac{r_0 N_A \varrho_m}{2\pi A} f'' = \frac{\lambda\mu}{4\pi}, \tag{2.9}$$

with μ the linear absorption coefficient.

δ as noted in Equation 2.7 is a positive real term and, as mentioned, about 5 orders of magnitude smaller than unity. Thus, the refractive index becomes less than unity, with a small deviation, though. As the electromagnetic wave velocity in matter is given by c_0/n, this would imply that the speed of light is higher in matter than in vacuum. However, it should be noted that c_0/n is the phase velocity and not the group velocity[iii]. Furthermore, since the refractive index is smaller than unity, total external reflection occurs below the X-ray critical angle of total external reflection, α_c. According to the small deviation of the refractive index from unity, α_c is in the range of only a few milli-radians. To obtain the critical angle, the law of refraction at the interface of vacuum and a medium with refractive index n_0 and by neglecting absorption can be written as[iv]:

$$\cos\alpha_i = (1-\delta)\cos\alpha_t, \tag{2.10}$$

with α_t angle of the transmitted wave (cf. Fig. 2.1). Now let $\alpha_t = 0$. Equation 2.10, knowing that $\alpha_c \ll \frac{\pi}{2}$ can then be written as

$$\alpha_c \approx (2\delta)^{1/2} = \lambda(r_0\varrho/\pi)^{1/2}. \tag{2.11}$$

Let an incoming plane electromagnetic wave $\mathbf{E}_i(\mathbf{r},t)$ with frequency ω illuminate a flat surface of a medium with a refractive index of n_0 at a glancing angle α_i (cf. Fig. 2.1). For $\alpha_i \geq \alpha_c$, a part of the incoming wave $\mathbf{E}_r(\mathbf{r},t)$ is reflected and a part $\mathbf{E}_t(\mathbf{r},t)$ is transmitted into the medium. This can all be described as

$$\mathbf{E}_i(\mathbf{r},t) = \mathbf{E}_i e^{i(\omega t - \mathbf{k}_i\cdot\mathbf{r})}, \tag{2.12}$$

$$\mathbf{E}_r(\mathbf{r},t) = \mathbf{E}_r e^{i(\omega t - \mathbf{k}_r\cdot\mathbf{r})}, \tag{2.13}$$

$$\mathbf{E}_t(\mathbf{r},t) = \mathbf{E}_t e^{i(\omega t - \mathbf{k}_t\cdot\mathbf{r})}, \tag{2.14}$$

[iii] Group velocity is evaluated as $d\omega/dk$ and is indeed less than c_0.

[iv] Note that for X-rays the angle is measured to the surface and not to the normal of the surface as in the case by visible light (cf. Fig. 2.1).

whereas for the wave vectors $\mathbf{k}_i, \mathbf{k}_r, \mathbf{k}_t$ the following relations are valid:

$$|\mathbf{k}_i| = |\mathbf{k}_r| = k_i = \frac{2\pi}{\lambda} = \frac{\omega}{c_0}; \qquad |\mathbf{k}_t| = k_t = \frac{2\pi}{\lambda_t} = \frac{\omega}{c_0} n_0, \tag{2.15}$$

with c_0 the speed of light in vacuum.

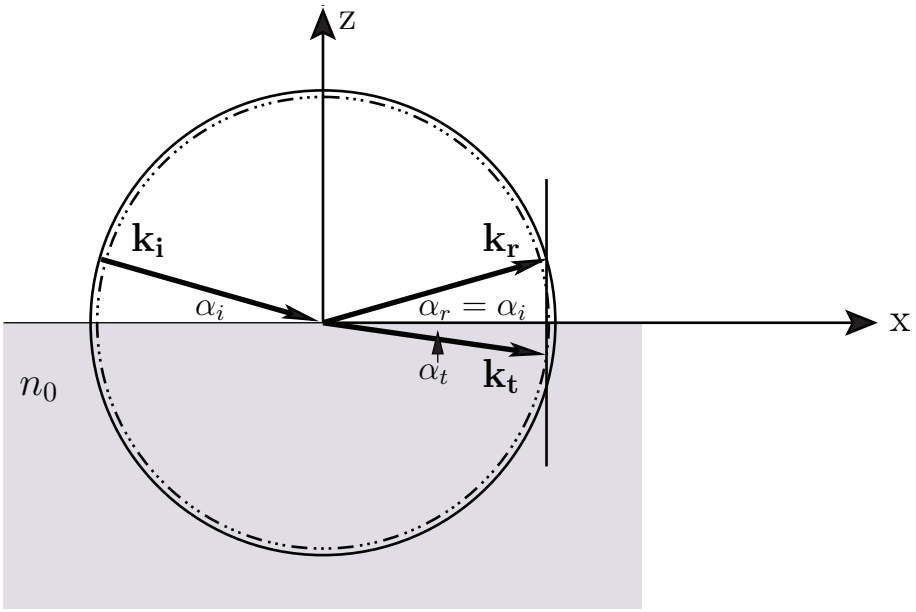

Figure 2.1: *Reflection and refraction of an X-ray plane wave at a smooth surface. The Ewald spheres of incoming and reflected (solid line) as well as refracted (dashed line) waves are sketched with radii given by $2\pi/\lambda$ and $2\pi n_0/\lambda$, respectively. The wave vector components parallel to the surface are preserved.*

The tangential components of the electric (and magnetic) fields have to be continuous at the surface. Considering Snell's law, the z components of the wave vectors can be written as

$$k_{i,z} = \frac{2\pi}{\lambda} \sin \alpha_i, \tag{2.16}$$

$$k_{t,z} = \frac{2\pi}{\lambda} (n_0^2 - \cos \alpha_i)^{1/2}. \tag{2.17}$$

For small angles of incidence compared to the Brewster angle, the Fresnel reflection and refraction coefficients are independent of the polarization state of the X-rays [76] and can be obtained as follows

$$r_F := \frac{E_r}{E_i} = \frac{k_{i,z} - k_{t,z}}{k_{i,z} + k_{t,z}}, \tag{2.18}$$

$$t_F := \frac{E_t}{E_i} = \frac{2k_{i,z}}{k_{i,z} + k_{t,z}}. \tag{2.19}$$

The experimentally accessible quantities are the intensities of the reflected and transmitted beam, $R_F = |r_F|^2$ and $T_F = |t_F|^2$, respectively, and not their amplitudes.

Fig. 2.2, left, shows the reflected intensity for CuK$_\alpha$ radiation[v] and different ratios of β/δ as a function of normalized incident angle α_i/α_c. As visible, in case of no absoption, the reflectivity remains constants and complete in the regime of total external reflection, i.e., until reaching the critical angle. R_F decreases rapidly for incident angles. Absorprtion only plays a role in the vicinity of the critical angle. On the right side of Fig. 2.2 the penetration depth of the X-ray is depicted. For angles of incidence below the critical angle, the transmitted wave has got a purely imaginary z-component of the wave vector. Therefore, an evanescent wave field is generated below the surface which is exponentially damped. This has a penetration depth, Λ, in the order of $10-100$ Å, and is related to total external reflection. For α_i values much larger than the critical angle, i.e. the case where the wave transmits into the medium, the penetration depth is described by the absorption as defined in Equation 2.9. The penetration depth, Λ, can generally be expressed as

$$\Lambda = \frac{\lambda}{2\pi l} \tag{2.20}$$

with (considering Equation 2.11 and small α_i)

$$l = \frac{\alpha_c}{\sqrt{2}} \left\{ (1-x^2) + \sqrt{(x^2-1)^2 + (\beta/\delta)^2} \right\}^{1/2}, \tag{2.21}$$

with $x = \alpha_i/\alpha_c$.

Above the critical angle $\alpha_c\Lambda$ scales with β/δ (cf. Fig. 2.2 right). For $\alpha_i \to 0$, l tends to α_c and thus, $\alpha_c\Lambda = \lambda/2\pi$ [vi]. According to Equation 2.11, this means that the penetration depth below the critical angle ($\Lambda_0 = 1/\sqrt{4\pi r_0 \varrho}$) is wavelength independent and merely a function of electron density of the material.

2.1.2 Roughness

Surfaces taken as basis in 2.1.1 where assumed to be sharp, i.e. to show no roughness. In practice, surfaces and interfaces are always rough. In order to model this roughness mathematically, the constant refractive index representing a jump to its value from the previous one, has to be replaced by a continuous variation of the refractive index. Assuming a multi-layer system, the refractive index of the jth layer can then be written as $n_j(x,y,z)$ corresponding to a continuous variation of electron density $\varrho_j(x,y,z)$. As the lateral inhomogenities give merely rise to off-specular diffuse scattering and in this section only specular scattering is of interest, the surface structure of an arbitary structure is laterally averaged over (x,y) and the one-dimensional refractive index turns out to

$$n_j(z) = \iint n_j(x,y,z)dxdy. \tag{2.22}$$

The rough interface can be modelled as an ensemble of smooth interfaces, each having a probability density $P_j(z)$ with mean value z_j and root mean square (rms) σ_j^2 (cf. Pic.

[v] Corresponds to a photon energy of 8048 eV. At this energy, $\delta^{Au} = 4.6147 \times 10^{-5}$ and $\alpha_c^{Au} = 0.556°$ [77].

[vi] For the X-ray wavelength taken as a basis in this section, $\lambda = 1.54$ Å, $\alpha_c\Lambda = 0.254$ Å rad (cf. Fig. 2.2).

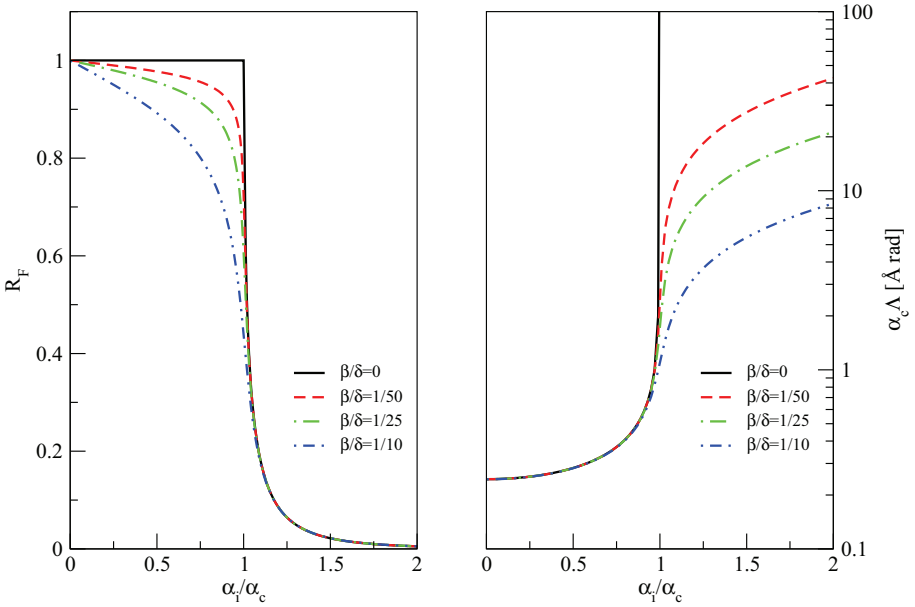

Figure 2.2: ***Left:*** *Fresnel reflectivity R_F versus normalized angle of incidence, for an X-ray beam of wavelength $\lambda = 1.54$ Å and different β/δ ratios.* ***right:*** *$\alpha_c\Lambda$ versus normalized angle of incidense, for an X-ray beam of wavelength $\lambda = 1.54$ Å and different β/δ ratios (after [78].*

2.3) as follows

$$z_j = \int z P_j(z) dz, \tag{2.23}$$

$$\sigma_j^2 = \int (z - z_j)^2 P_j(z) dz. \tag{2.24}$$

If the mentioned probability density function is assumed to be Gaussian with $z_j = 0$, $P_j(z)$ can be expressed as

$$P_j(z) = \frac{1}{\sqrt{2\pi}\sigma_j} \exp\left(\frac{-z^2}{2\sigma_j^2}\right). \tag{2.25}$$

Thus, the continuous refractive index between the two layers j and $j+1$ turns out to

$$n_j(z) = \frac{n_j + n_{j+1}}{2} - \frac{n_j - n_{j+1}}{2} \mathrm{erf}\left(\frac{z - z_j}{\sqrt{2}\sigma_j}\right), \tag{2.26}$$

with the error function defined by

$$\mathrm{erf}(z) = \frac{2}{\sqrt{\pi}} \int_0^z \exp(-\zeta^2) d\zeta, \tag{2.27}$$

and this results into the modified Fresnel coefficients, yielding [78]

$$\tilde{r}_j = r_j S_j = r_j \exp\left(-2k_{j,z}k_{j+1,z}\sigma_j^2\right), \tag{2.28}$$

$$\tilde{t}_j = t_j T_j = t_j \exp\left(+(k_{j,z} - k_{j+1,z})^2 \sigma_j^2/2\right), \tag{2.29}$$

with S_j and T_j the so-called Névot - Croce factors [79, 80].

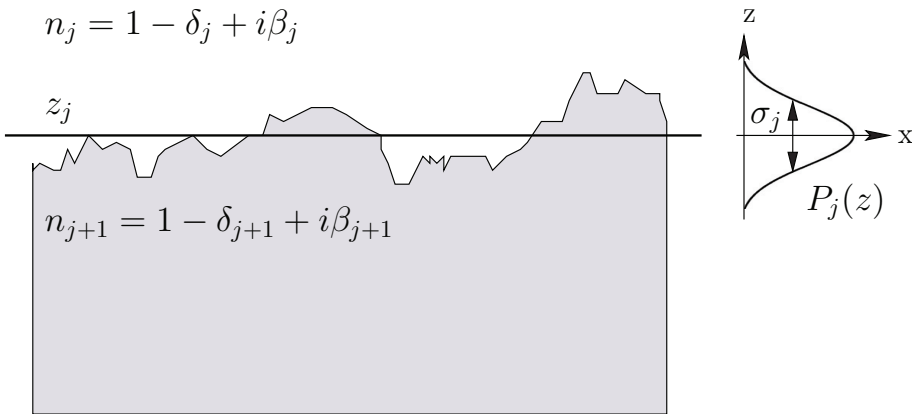

Figure 2.3: *Rough interface with a mean z coordinate value, z_j. The surface can be replaced by an ensemble of smooth surfaces weighted by probability density $P_j(z)$.*

2.1.3 Multilayers

In most of the practical cases one does not cope with a single layer but with a stratified medium, where all the layers contribute to the reflectivity detected. In this section scattering from a multilayer system, consisting of m rough layers modeled after Névot - Croce (cf. Sec. 2.1.2), is studied. Vacuum poses the 0th layer with the first interface at $z_0 = 0$ and the substrate counts as the mth layer (cf. Fig. 2.4). The refractive index of each layer, with thickness $d_j = z_{j-1} - z_j$, is $n_j = 1 - \delta_j + i\beta_j$. At the interface of any two successive smooth layers j and $j+1$, an electromagnetic wave traveling in j impinging at an angle α_j^i larger than the critical angle of the layer α_j^c, splits into a reflected wave outgoing at the same angle ($\alpha_j^r = \alpha_j^i$) and a refractive wave transmitted at α_j^t. The generalised z component of the wave vector in each layer can be written as

$$k_{j,z} = \frac{2\pi n_j}{\lambda} \sin(\alpha_j^i) \tag{2.30}$$

$$k_{j+1,z} = \frac{2\pi}{\lambda} \left((\frac{n_{j+1}}{n_j})^2 - \cos^2(\alpha_j^i) \right)^{1/2}. \tag{2.31}$$

Hence, the Fresnel reflection and refraction coefficients in each layer can be stated as

$$r_j = \frac{k_{j,z} - k_{j+1,z}}{k_{j,z} + k_{j+1,z}}, \tag{2.32}$$

$$t_j = \frac{2k_{j,z}}{k_{j,z} + k_{j+1,z}}. \tag{2.33}$$

An X-ray beam impinging on the 0th layer at a grazing incidence angle larger than the critical angle gets partially reflected and refracted. The refracted part experiences the same scenario, until the beam has reached the substrate which, due to its thickness, is assumed not to reflect at all. Thus, the reflectivity measured by these systems is a result of reflections and transmissions in all layers. The electric field intensity for reflected and transmitted beams in each layer can be obtained by a recursive approach first described in

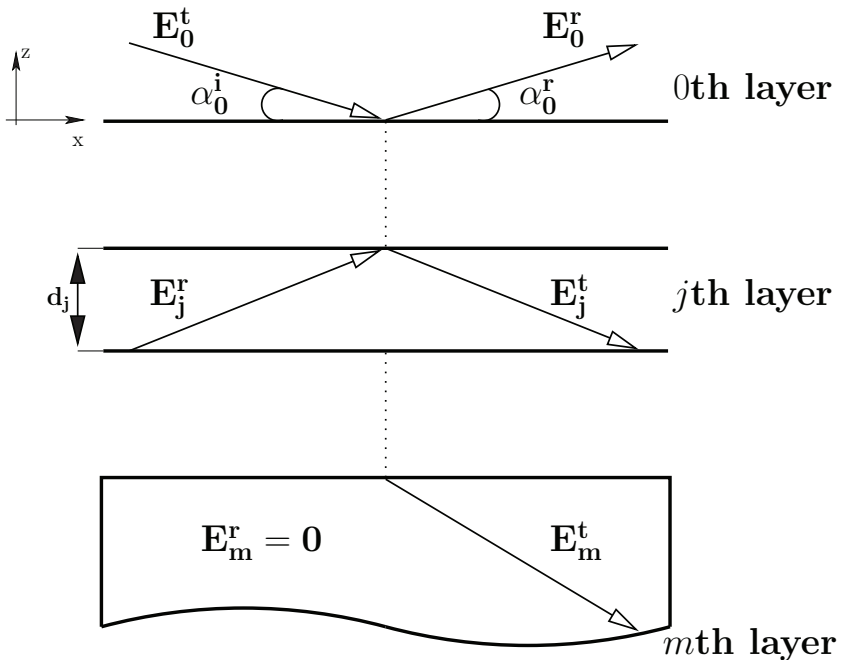

Figure 2.4: *Schematic multilayer system of m layers. In each layer only one transmitted as well as reflected term, shown as a vector, represents all others.*

1954 by Parratt [81]. In this method the reflected electric field, E_j^r, and the transmitted electric field, E_j^t at the top of the jth layer, considering Equations 2.28 and 2.29, are given by

$$E_j^r = a_j^2 \Xi_j E_j^t, \tag{2.34}$$

$$E_{j+1}^t = \frac{a_j E_j^t \tilde{t}_j}{1 + a_{j+1}^2 \Xi_{j+1} \tilde{r}_j}. \tag{2.35}$$

Ξ_j is an auxiliary parameter for recursion described as

$$\Xi_j = \frac{\tilde{r}_j + a_{j+1}^2 \Xi_{j+1}}{1 + a_{j+1}^2 \Xi_{j+1} \tilde{r}_j}, \tag{2.36}$$

and

$$a_j = \exp\left(-ik_{j,z} d_j\right), \tag{2.37}$$

with d_j the thickness of jth layer.

There is no reflection in the substrate such that $E_m^r = \Xi_m = 0$ [82]. For calculating the reflection intensity at the top of the structure, one begins from the substrate with the information given [83, 84, 85]. Knowing λ and α_0^i together with n_j and d_j of each layer, the reflectivity R can then be obtained as following

$$R(\alpha_0^i) = |E_0^r / E_0^t|^2. \tag{2.38}$$

2.1.4 Formation of Standing Waves

As it can be extracted from Eqs. 2.30 and 2.31, $k_{j,z}$ contains both real part, $\Re(k_{j,z})$, and imaginary part, $\Im(k_{j,z})$, whereas absorption of the layer, (β_j), contributes to the latter. According to this, the total field intensity in each layer j can be obtained by

$$\begin{aligned} I(\alpha_j^i, z) &= |E_j^r(\mathbf{r}) + E_j^t(\mathbf{r})|^2 \\ &= |E_j^t(0)|^2\{\exp[-2\Im(k_{j,z})z] \\ &\quad + R\exp[2\Im(k_{j,z})z] + 2\sqrt{R}\cos[\nu - 2\Re(k_{j,z})z]\}, \end{aligned} \tag{2.39}$$

where ν is the relative phase between the incident and reflected E-field amplitudes. It is obvious from Equation 2.39 that a standing wave forms in the jth layer. Interaction of antinodes of this standing wave field with the core electrons of the atoms in the jth layer (or above layer $j+1$) excites the atoms and leads, inter alia, to fluorescence radiation. This fluorescence yield is detectable and can be calculated as follows

$$Y(\alpha_j^i) \propto \int I(\alpha_j^i, z)\rho_j^A(z)dz, \tag{2.40}$$

where $\rho_j^A(z)$ is the atomic density distribution as a function of z [86]. It is generally not possible to deconvolute $\rho_j^A(z)$ when $Y(\alpha_j^i)$ is known. Therefore, a model density distribution function has to be established and get verified by being inserted in relation 2.40 while performing fitting steps.

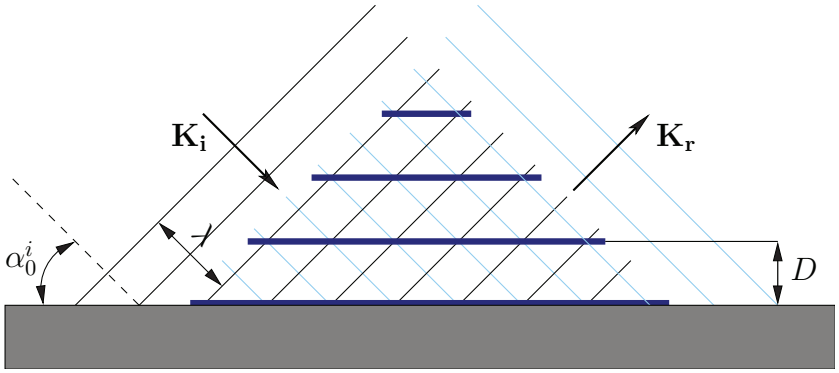

Figure 2.5: *X-ray standing wave field formed on top of a mirror by interference of an incoming and a specular-reflected beam.*

Neglecting the absorption of the jth layer and in total external reflection regime leads to $\Im(k_{j,z}) = 0$. Considering Equation 2.39, the standing waves intensity on top of the layer $j+1$ increases from 0 to $4|E_j^t(0)|^2$ as α_j^i is increased from 0 to $\alpha_j^i = \alpha_j^c$. For $j = 0$, i.e. in vacuum, refering to Equation 2.30, Equation 2.39 can be simplified to [62, 83, 87, 88, 89]

$$I(\alpha_0^i, z) = |E_j^t(0)|^2[1 + R + 2\sqrt{R}\cos(\nu - 2\pi z/D(\alpha_0^i))], \tag{2.41}$$

with $D(\alpha_0^i)$ the period of the planes with maximum intensity parallel to the surface (cf. Fig. 2.5), given by:

$$D(\alpha_0^i) = \lambda/2\sin(\alpha_0^i). \tag{2.42}$$

Element (density $[g/cm^3]$)	Al Kα 1486.7 eV (8.34 Å) α_c [°]	Al Kα 1486.7 eV (8.34 Å) D_c [nm]	Ag Lα 2984.3 eV (4.15 Å) α_c [°]	Ag Lα 2984.3 eV (4.15 Å) D_c [nm]	Cu Kα 8047.8 eV (1.54 Å) α_c [°]	Cu Kα 8047.8 eV (1.54 Å) D_c [nm]
Si (2.33)	1.11	21.4	0.6	20.1	0.223	19.3
Au (19.32)	2.59	9.2	1.35	8.9	0.556	7.7
Pt (21.45)	2.64	9.0	1.46	8.2	0.584	7.4
Ir (22.42)	2.68	8.9	1.51	8.0	0.597	7.2

Table 2.1: Critical angle and critical period of different elements calculated for three x-ray energies [77].

By increasing the incidence angle from zero, the first antinodal plane propagates from infinity towards the surface until the critical angle is reached. Thus, the larger the critical angle is, the smaller are the reachable periods, as extractable from Equation 2.42, and therefore, smaller structures on the surface can be investigated. Having tunable intensity period is predominent advantage of TER-XSW method in comparison to the conventional XSW. Decreasing the wavelength hardly decreases the critical period $D_c := D(\alpha_0^c)$, despite the seeming linear dependency in Equation 2.42, as the critical angle is also wavelength dependent:

$$D_c = \frac{\lambda}{2\sin\alpha_0^c} \approx \frac{\lambda}{2\alpha_0^c} \approx \frac{\lambda}{2\lambda\sqrt{r_e\rho/\pi}} = \frac{1}{2\sqrt{r_e\rho/\pi}}. \tag{2.43}$$

Equation 2.43 clearly demonstrates that if absorption is negligible, the critical period depends exclusively on the material. It is reciprocally proportional to the square root of the electron density. Thus, the denser the mirror is, the smaller is the critical period. Table 2.1 shows the critical angle and period for Si, as a standard substrate material in comparison to three of the densest elements at common x-ray energies. Si has, as expected, the smallest critical angle and the largest period of all of them. This makes Si inappropriate for investigation of structures smaller than about 20 nm. Ir on the other hand, exhibits, together with Au and Pt, critical periods down to 7 nm. This is the physical size limitation of structures which can be resolved, if brought directly onto a mirror surface to be investigated.

Figure 2.6 shows the contour plot of the standing wave field intensity on top of a smooth Au mirror Cu K_α radiation as a function normalized incidence angle and the distance to the mirror, together with the intensity oscillation at two fixed distances from the mirror, $z = 8$ nm and $z = 23$ nm. These two distances were chosen as examples for positions where for $\alpha_0^i = \alpha_0^c$, antinodes exist. It can easily be obtained that the atoms at higher distances to the surface of the mirror get more often excited as more antinodes pass them by.

2.2 X-ray Absorption Fine Structure

In this section we briefly describe the theoretical background for XAFS measurements carried out in this work, beginning with some general information about X-ray absorption,

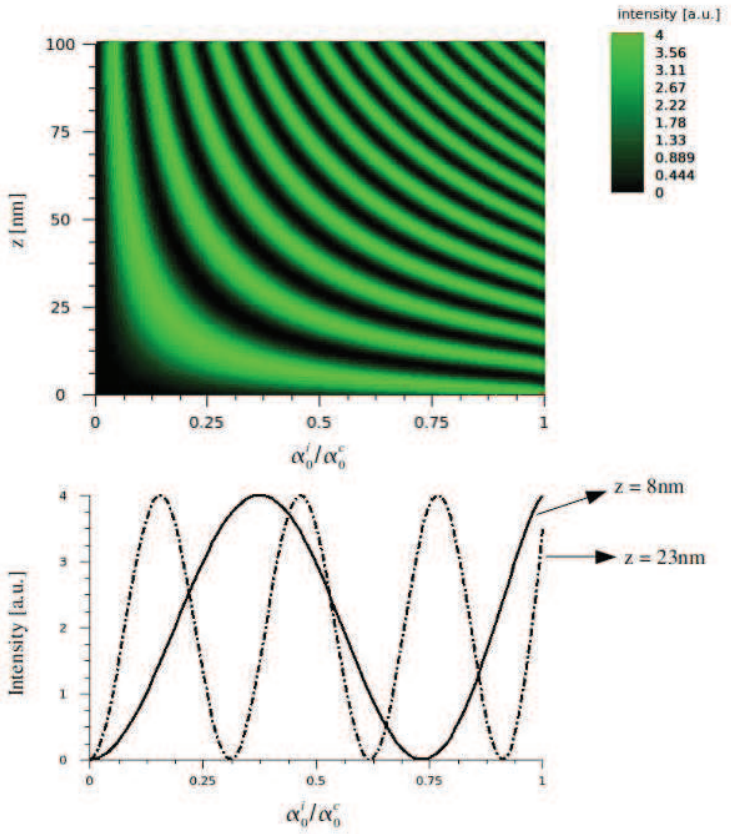

Figure 2.6: *TER-XSW intensity above a Au mirror at 8048 eV.* ***Top****: The intensity is shown as a function of the normalized incidence angle and the distance to the surface.* ***Bottom****: The intensity of the standing waves at two fixed distances to the mirror as a function of normalized incidence angle.*

carrying on to EXAFS method.

2.2.1 X-ray Absorption

An X-ray penetrating into a material loses intensity due to elastic scattering (Rayleigh scattering), inelastic scattering (Compton scattering) and especially due to photoelectric absorption, where the X-ray photon is absorbed by the atom, and the excess energy is transferred to an electron, which is expelled from the atom, leaving the atom ionized.

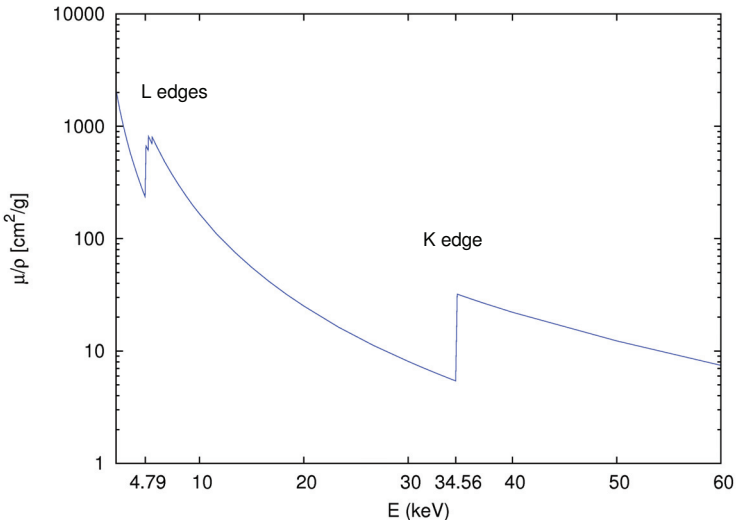

Figure 2.7: *Mass attenuation coefficient (μ/ϱ) of xenon vs. photon energy [90].*

The intensity loss occuring due to penetrating in an absorbing material of thickness d can be described by Lambert-Beer law as

$$I = I_0 \exp(-\mu d), \tag{2.44}$$

with I_0 intensity of the incoming beam, I intensity of the transmitted beam and μ the linear absorption coefficient (cf. Equation 2.9). By determination of the absorption coefficient over a large energy range, big jumps in the course are apparent. Fig. 2.7 shows, as an example, course of the mass attenuation coefficient μ_ϱ[vii] of a noble gas vs. energy. These so-called absorption edges come about precisely there as the photon energy is enough to merge an electron from a specific shell into the continuum, leaving a hole behind. Thereafter, one of the electrons in an outer shell fills the hole. The excessive energy can be then emitted as a photon, i.e., fluorescent X-ray emission, or excite another electron from

[vii]The mass attenuation coefficient is a measurement of how strongly a chemical species or substance absorbs or scatters light at a given wavelength, per unit mass. It is after $\mu d = (\mu/\varrho)\varrho d = \mu_\varrho \varrho d$ proportional to linear absorption coefficient μ.

a higher shell into the continuum, i.e., Auger electron emission.

With two detectors, that measure the intensity in front of and behind the sample, μd gets extractable. Having a non-transparent sample, fluorescent emission, photo electrons, or Auger electrons can also be measured, as these signals are also proportional to X-ray photon absorption.

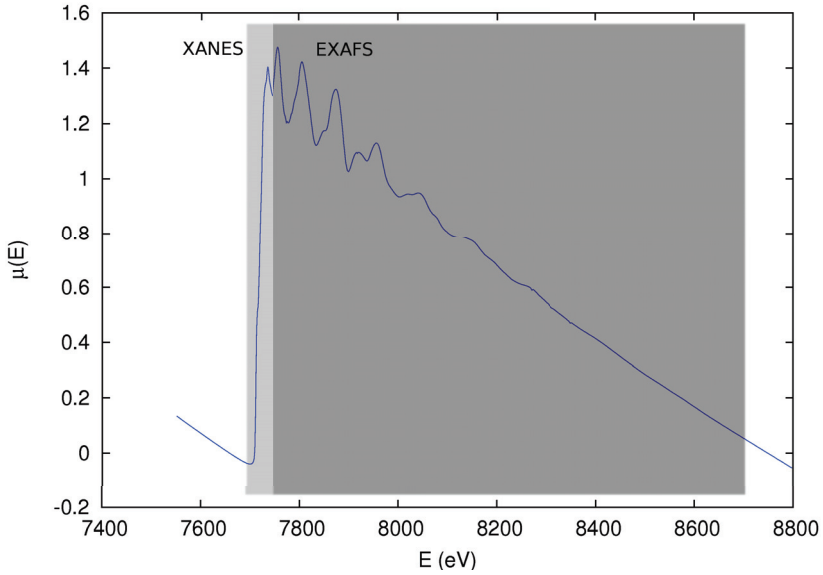

Figure 2.8: *XAFS spectrum of Co K-edge, subdevided in to XANES and EXAFS regions.*

Absorption spectra of solid state materials, contrary to monoatomic gases demonstrate a fine structure which is due to the scattering of the photoelectrons at the neighbouring atoms of the absorbing atom (cf. Fig. 2.8). The fine structure above the absorption edge is denoted as X-ray Absorption Fine Structure (XAFS) and is subdevided into two regions: X-ray Absorption Near Edge Structure (XANES), which extends to about 30 eV above the edge, and Extended X-ray Absorption Fine Structure (EXAFS), the region about 1 keV above the edge. By EXAFS data analysis conclusions about the atomic vicinity of an absorbing atom are obtained. XANES, however, delivers information about the electronic structure of the absorbing atom. Since only EXAFS analysis is in the focus of this work, only this will be explained in the following subsection and theoretical backgrounds regarding XANES [91, 92] will be omitted.

2.2.2 Extendend X-ray Absorption Fine Structure

A core electron excited by absorption of an X-ray photon with sufficient energy propagates as spherical wave (primary wave) in the mater and scatters at neighbouring atoms, the so-called backscatterers (secondary waves). Both primary and secondary waves then interfere, depending on the phase, destructively or constructively. The transition of an electron can be described by Fermi's golden rule as

$$\mu(E) \sim |\langle f|\mathcal{H}|i\rangle|^2, \tag{2.45}$$

where E is the photon energy, $|i\rangle$ the initial state, $|f\rangle$ the final state and $\mathcal{H}$ the Hamiltonian operator. The final state, unlike the initial state, is influenced by the neighbouring atoms of the absorbing atom. The absorption probability increases or decreases by constructive or destructive interference, respectively. Furthermore, the wavelength of the primary as well as secondary waves depends on the energy of the absorbed X-ray photons. Thus, the photon energy also changes the absorption probability.

The fine structure $\chi(E)$ above the absorption edge is mathematically described by

$$\chi(E) = \frac{\mu(E) - \mu_0(E)}{\Delta\mu_0(E_0)}, \tag{2.46}$$

where $\mu(E)$ is the measured absorption coefficient, $\mu_0(E)$ the absorption coefficient of an isolated atom and $\Delta\mu_0(E_0)$ the measured height of the edge stroke (cf. Fig 2.9).

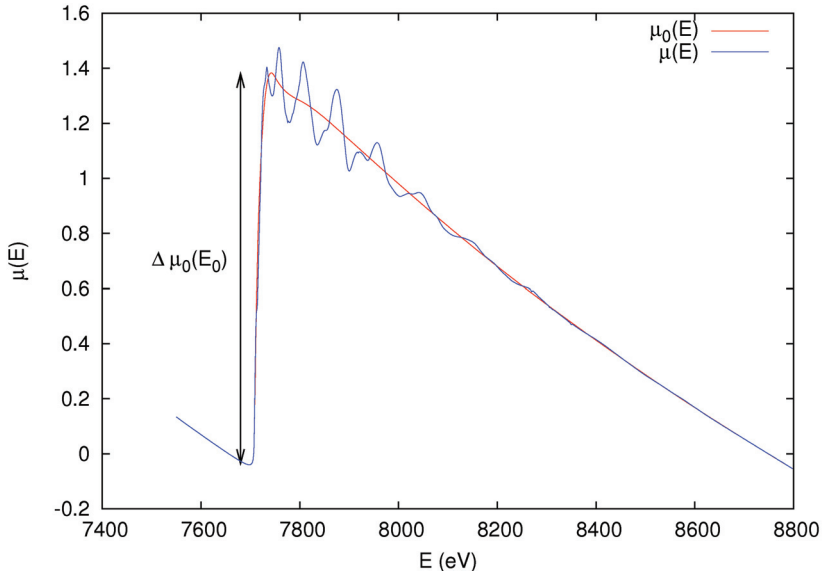

Figure 2.9: *Measured absorption coefficient of Co, $\mu(E)$ (blue), and absorption coefficient of an isolated Co atom $\mu_0(E)$ (red) vs. photon energy. The edge stroke $\Delta\mu_0(E_0)$ is indicated [93].*

The fine structure is due to the wave character of the photoelectrons. Hence, it would be useful to convert the photon energy E to k, i.e. the modulus of the wave vector $\mathbf{k}$:

$$k = \sqrt{\frac{2m(E - E_0)}{\hbar^2}}, \tag{2.47}$$

with m the electron mass and E_0 the energy of the absorption edge. Fig. 2.10 left shows the fine structure $\chi(k)$ obtained by this conversion. In this case the oscillations fall off rapidly by increasing k. Hence, for the data analysis the fine structure gets commonly weighted by k, k^2 or k^3. Fig. 2.10 right shows the fine structue $\chi(k)$ weighted by k^2.

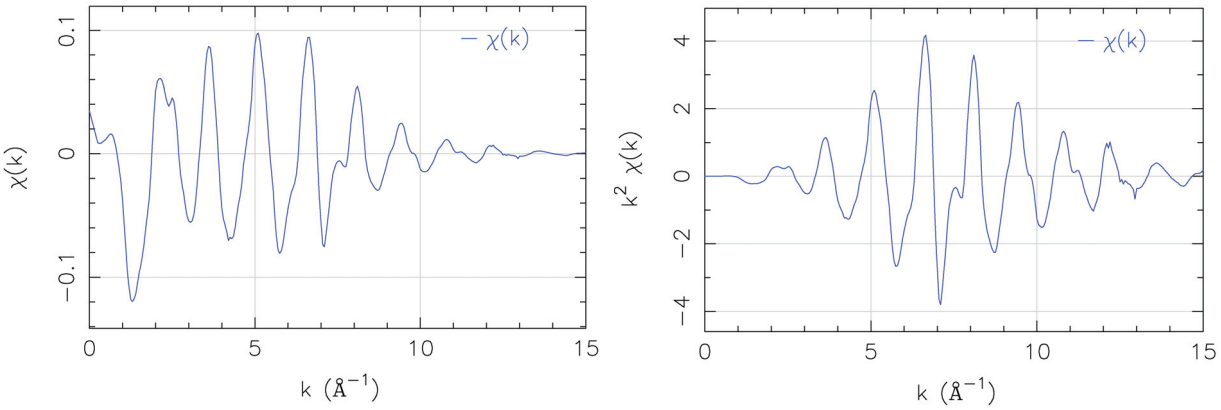

Figure 2.10: *EXAFS fine structure of Co,* ***left****: not weighted and* ***right****: weighted with* k^2.

The fine structure can be described by the EXAFS equation [94] as

$$\chi(k) = \sum_j N_j S_0^2 \cdot F_j(k) \frac{\sin(2kR_j + \delta_j(k))}{kR_j^2} \cdot e^{-2\sigma_j^2 k^2} \cdot e^{\frac{-2R_j}{\lambda_j(k)}}. \tag{2.48}$$

This is the sum of all backscattering contributions of N_j backscatterers of each coordination shell j with distance R_j to the absorbing atom. $F_j(k)$ is the amplitude function of the backscatterers, which depends on the atoms. Thermal oscillation and statistical disorder of the atoms extenuate the fine structure. These are described by $\exp(-2\sigma_j^2 k^2)$, with σ_j^2 the Debye-Waller factor. In order to be able to influence the final state, the photoelectron has to be backscattered to the absorber atom before the hole is filled by another electron. Both of these effects can be described by a damping term $\exp(-2R_j/\lambda_j(k))$ regarding the mean free path $\lambda_j(k)$. This describes the mean path of an electron before getting inelastically scattered or before the hole is refilled. This makes EXAFS a local characterisation method. Since long-range order is not necessary even non-crystalline samples can be probed. $\delta_j(k)$ is the total phase shift by phase jumps at the absorber atom and backscatterers. The amplitude reducing factor S_0^2 is the passive electron reduction factor and due to the relaxation of the electrons remaining in the absorber atom [95].

A Fourier transform transfers the fine structure into a pseudoradial distribution function (cf. Fig. 2.11). Each peak can be assigned to a coordination shell. Note that the peaks are shifted about $0.2 - 0.5$Å towards origin due to the phase shift. Knowing the phase and backscattering amplitude function of each backscatterer together with the mean free path, the fine structure delivers information about the kind, number and distance of the neighbouring atoms.

2.3 Grazing-Incidence Small-Angle X-ray Scattering

Small-angle X-ray scattering (SAXS) denotes the elastic scattering of monochromatic X-ray beam under small scattering angles (Thomson scattering). When the X-ray beam

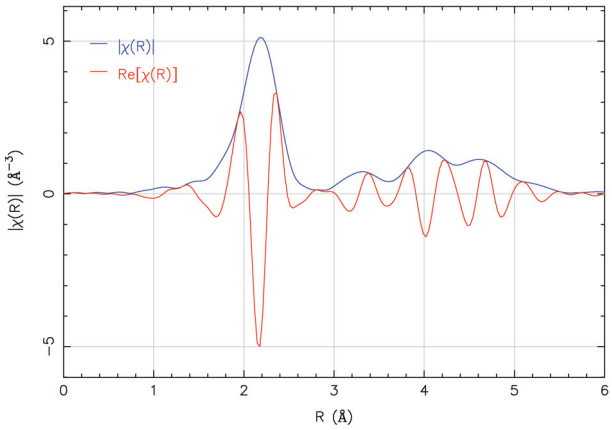

Figure 2.11: *Real part and modulus of the pseudoradial distribution function.*

penetrates the matter the electrons are forced into oscillation and send out secondary radiation. If the sample compound contains colloidal structures larger than the wave length of the X-ray beam, then interference of these waves appear at small angle. The X-ray beam is scattered by the electrons, so the small angle scattering appears if and only if the regions of the colloidal dimensions differ in their electron density values.

An incoming plane wave of wavelength λ and wave vector $\mathbf{k}$ scatters elastically ($|\mathbf{k}| = |\mathbf{k}'|$) at the electrons of the sample atoms. The scattered spherical wave can then be detected by e.g. a two-dimensional position-resolving detector under the scattering angle 2θ (cf. Fig. 4.6). The scattering vector $\mathbf{q}$ depends on the wavelength and the scattering angle, as $|\mathbf{q}| = q = 2k \sin\theta = 4\pi/\lambda \sin\theta$. The modulus of the scattering vector, q, specifies a characteristic length, $L \approx 2\pi/q$. Let q_{min} be the minimum reachable q-value in a SAXS experiment, then the maximum structural inhomogeneity which can be analyzed has got a size of $L_{max} \approx 2\pi/q_{min}$ [96].

The conventional SAXS geometry is not suitable for investigation of mesoscopic objects on a substrate due to the fact that depending on the incidence angle a part of the incoming beam transmits into the substrate (cf. 2.1.1). Therefore, a reflection geometry with grazing incidence (GISAXS) is chosen here, combining SAXS with surface sensitivity. This idea was first applied by Levine et al. [97, 98].

Performing GISAXS measurements by averaging over the whole illuminated surface area, precise information about the average particle-particle distance is delivered and this allows to quantify the degree of ordering of the nanoparticles in the film. For a general and quantitative GISAXS analysis of free-standing islands, a theoretical treatment within the framework of the distorted-wave Born approximation (DWBA) is demanded [99, 100, 101]. However, with respect to the value of the lateral component of the scattering vector $q_{||}$ there is no difference of the DWBA to a simplified description according to the simple Born approximation, hence application of the latter is justified.

By fitting Lorentzian shape functions, which was found to yield satisfactory results in our case, the mean particle-particle distance $\langle d \rangle$ can be calculated from the in-plane distance between the two first-order satellite peak positions $\Delta q_{||}$ (cf. Fig. 2.12) by virtue

of the relation [102]

$$\langle d \rangle = \frac{2}{\sqrt{3}} \frac{4\pi}{\Delta q_{||}}. \tag{2.49}$$

Furthermore, the peak width δq (cf. Fig. 2.12) provides a measure for the degree of ordering in the film. Accordingly, the correlation length Γ of the particle arrangement may be defined as $\Gamma = 2\pi/\delta q$. However, this definition is by no means unique and generally depends on the model of correlation assumed for the analysis [103].

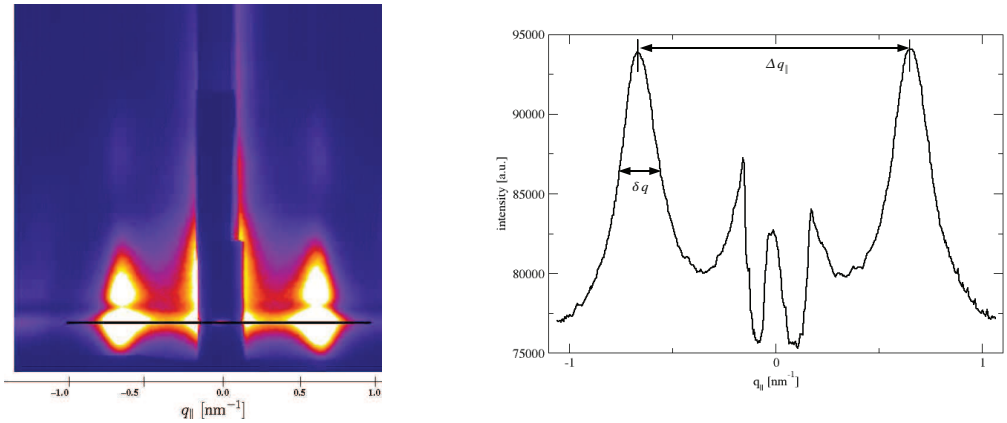

Figure 2.12: ***left****: GISAXS CCD image of a sample of deposited $CoPt_3$ NPs. The horizontal black line indicates the position of the extracted line profile.* ***right****: The line profile obtained from the GISAXS CCD image. $q_{||}$. $\Delta q_{||}$ as well as δq are indicated here.*

Chapter 3

Experimental Details I (Sample Preparation)

This chapter deals with sample preparation and contains information about the substrate choice, support functionalization and optimization of nanoparticle coating processes. The question of sample preparation can be tackled from different points of view, here explained in a step-by-step approach.

3.1 Substrate

In order to be able to to perform TER-XSW and GISAXS measurements, the nanoparticles have to be supported on a substrate (cf. 2.1 and 2.3). The first runs of the TER-XSW measurements were performed on nanoparticles deposited on Si(100), because of prevalence of this common substrate and previous GISAXS investigations on the same system in our group [103]. Corresponding TER-XSW experiments, however, remained without any distinct success. The reflectivity signal delivered information about the layer thicknesseses etc. but the fluorescence signal did not show any oscillations and, therefore, could not be used for a reliable structural characterization. Looking back into Table 2.1, one comprehends that due to the relatively low density of Si, its crtitical period D_c is at about 20 nm and thus, relatively large. This is, thereupon, not appropriate to investigate particles with diameters up to 8 nm. Hence, a material with a higher density has been used as the TER-XSW mirror in the following.

It is possible to coat Si substrates with polycrystalline Au layers in different desired thicknesses via physical vapour deposition [104]. Due to the polycrystalline nature of these Au films, the surface of the Au layer is rough. It is known that in case of thin films this roughness depends on the thickness of the Au layer [105], meaning that the thicker the Au layer is the rougher the surface becomes. On the other hand, as already described by Equations 2.20 and 2.21, depending on the photon energy a penetration depth of photons can be calculated. In order to be able to use Au as a bulk-like mirror a minimum thickness is necessary. A thickness of about 35 nm has been considered as appropriate for different possible photon energies. For such a layer thickness, a nominal roughness of ± 1 nm has been stated by the manufacturer [50].

cobalt concentration	platinum concentration
0.5 mgl^{-1}	1 mgl^{-1}
1 mgl^{-1}	2 mgl^{-1}
2.5 mgl^{-1}	3 mgl^{-1}
5 mgl^{-1}	5 mgl^{-1}
10 mgl^{-1}	10 mgl^{-1}

Table 3.1: Different solutions of known concentration used for AAS calibration

The critical period of standing waves in total reflection for Au is about 8 nm (cf. 2.1.4). Investigation of particles with almost the same size as in the case of this work and having Fig. 2.6 in mind, which shows the oscillation going through this distance from the mirror lead to the point, looking for methods which can elevate the nanoparticles to higher vertical positions. The more antinodes go through the particles, i.e., the more oscillations are the case at a specific position, the preciser the evaluation of the TER-XSW data. This fact, together with the idea of potential functionalization of the substrate for diverse applications has developed the idea of using self-assembled molecules. For this sake, it was important to use relatively long molecules with stable bounding potential to substrate from one end and the nanoparticles from the other end. Hexadecanethiol (HDT) has turned out to be appropriate for this purpose (cf. 1.3.1). In order to coat the Au/Si substarte with HDT SAMs, the wafer was cut into $\sim 10 \times 10$ mm^2 pieces and laid into 50 ml of a 10 mM alcanethiol solution of HDT and ethanol for 24 hours. They were subsequently rinsed and dried by high purity ethanol and nitrogen gas, respectively [106]. Processing the Au/Si samples with SAMs is very accessible, and thus has been always the case.

3.2 Atomic Absorption Spectrometry

After the $CoPt_3$ solution has been prepared as described in 1.2.1 the concentration of the solution has to be determined. This is performed by atomic absorption spectroscopy (AAS) method. For that 100 μl of the solution is vaporized into a beaker solved by 1 ml aqua regia (HNO_3/HCl=3/1).
AAS is mainly based on Lambert-Beer law (cf. 2.2.1). A light source emits light with different wave lengths of a defined intensity. An atomization unit, placed in the light path, atomizes the sample, whose concentration has to be determined. Atomization of the elements takes place using a gas flame, into which the sample solution is sprayed. The intensity of the light after the atomization unit is reduced due to the absorption in the atom cloud. The two intensities before and after the flame are compared. It can consequently be determined which amount of the intensity of a definite wave length has been absorbed . The higher the concentration, the higher the absorption of the emitted light.
A calibration step is required before starting with the actual measurement. This was done by different concentrated solutions of Co and Pt, listed in Table 3.1.

3.3 Coating Processes

As already described in 1.3, two main processes for coating the substrates with nanoparticles have been set in. In order to optimize the spin coating parameters, methods of statistical experimental design [107] have been used. In case of dip coating these parameters were mainly adopted from [38]. In the following a short introduction into statistical experimental design will be given and the results gained applying this method will be presented.

3.3.1 Statistical Experimental Design

Statistical Experimental Design or design of experiments (DoE) is the design of any information-gathering exercises where variation is present. Here, the experimenter is interested in the effect of some process or intervention on the yield. Small number of experiments and simultaneous variation of all factors with an effect on yield are some of the advantages of this systematic method. The stages in the DoE process can be itemized as follows

1. problem formulation
2. finding out the dominating factors and desicion about
   (a) Full Factorial Design
   (b) Fractional Factorial Design
3. Finding optimal regions of operability
4. Response surface modeling and optimization
5. Testing the Robustness

Full Factorial Design

In this variation of DoE two acceptable values, denoted with -1 and 1, are chosen for all the important variables. Each possible combination of the values corresponds to an experiment. Let x be the number of variables, from this it follows that 2^x experiments have to be performed. Fig. 3.1 shows an example for two variables. Furthermore, the scheme show that although only four experiments have been performed, a large range of possible combinations are covered. It is possible determine the effects of each variable on the yield. The effect of a variable M_x is defined as the midification of the yield by modifying the variable from -1 to 1. Contemplating the first two experiments one comes to the conclusion that the difference between the two yields y_1 and y_2 could have only been originated by variable x_1 as x_2 has remained constant. The same is the case for the difference between y_3 and y_4. Respectively, the differences between y_1 and y_3 as well as y_2 and y_4 are originated by x_2.

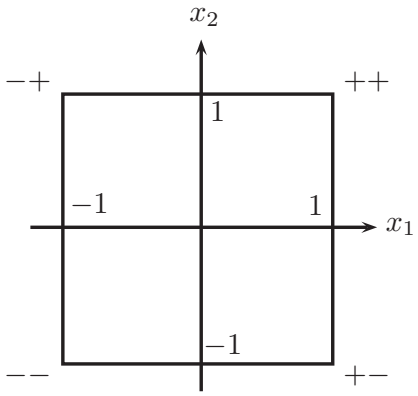

n	x_1	x_2	yield
1	1	1	y_1
2	−1	1	y_2
3	1	−1	y_3
4	−1	−1	y_4

Figure 3.1: *Example of a full factorial design for two variables*

The effect of a varible can be calculated as the mean value of the yield differences so that they can be determined independently:

$$M_1 = [(y_1 - y_2) + (y_3 - y_4)]/2 \tag{3.1}$$
$$M_2 = [(y_1 - y_3) + (y_2 - y_4)]/2. \tag{3.2}$$

In general, the effects of the variables in case of N experiments can be calculated as follows

$$M_i = \left[\sum_{n=1}^{N}(x_{i,n}.y_n)\right]/(N/2). \tag{3.3}$$

Furthermore, this method allows to calculate the interaction effects of two variables. As an example, the both differences $(y_2 - y_1)$ and $(y_4 - y_3)$ must not have the same value even though both are originated by modification of the same variable. This distinction can be led back to the interaction between the variables and can be calculated as

$$M_{i,j} = \left[\sum_{n=1}^{N}(x_{i,n}.x_{j,n}.y_n)\right]/(N/2). \tag{3.4}$$

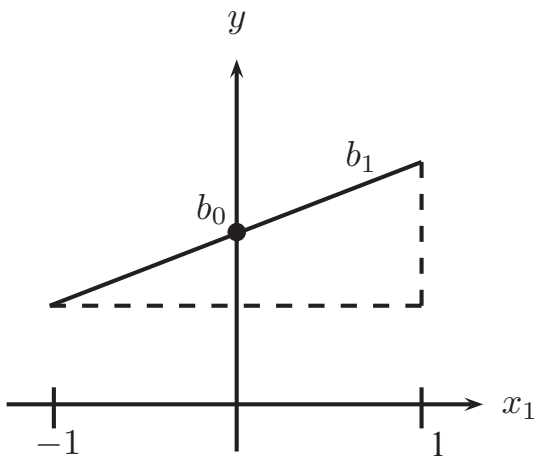

Figure 3.2: *Yield changes vs. modification of variable* x_1

In order to develop a linear model for calculation of different effects on the yield, one starts with determination of the slope of the straight line, b_x, originated by applying yield y vs. viariable x (cf. Fig. 3.2).

As already mentioned, the yield difference, Δy, complies with the effect M so that the slope coefficients can be expressed as $b_i = M_i/\Delta x = M_i/2$.

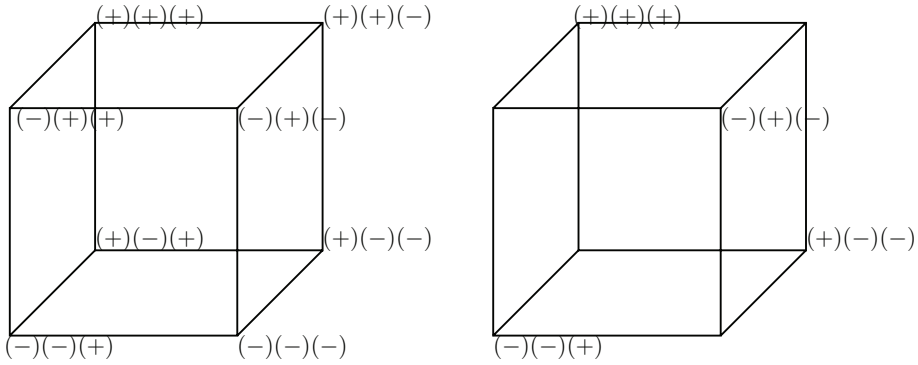

Figure 3.3: *Graphical representation of design of experiments with three variables in full factorial design (left) and fractional factorial design (right). By reducing the number of variables from three to two (going to fractional version) the number of experimnets are strongly reduced.*

Equation 3.5 shows the linear equation in case of two variables:

$$y = b_1.x_1 + b_2.x_2 + b_{12}.x_{12} + b_0, \tag{3.5}$$

with $x_{12} = x_1.x_2$. The first term takes the effect of variable x_1 into account, the second, the effect of x_2 and the third the interaction between the variables, with $b_{ij} = M_{ij}/2$. b_0 is the mean yield of all experiments calculated as

$$b_0 = \left[\sum_{n=1}^{N}(y_n)\right]/N \tag{3.6}$$

Fractional Factorial Design

The disadvantage of full factorial design is that in case of n variables 2^n have to be performed, which can easily get expensive. In order to reduce the number of experiments the fractional factorial design can be applied. The idea is based on an assumption equating experiments, by which the simultaneous modification of the variables are similar regardless the initial values. As an example, an experiment with the combination $x_1x_2x_3 = (+1)(+1)(-1)$ contains the same information as $x_1x_2x_3 = (-1)(-1)(+1)$, as in both case x_1 and x_2 have been simultaneously modified. Fig. 3.3 intimates that the possessed space of all combinations after reduction is still large without having lost much of information, even after the number of experiments have been halved.
The experiments for n variables can be set up the same as in case of full factorial design for $n-1$ variables succeeded by letting $x_n = x_1x_2...x_{n-1}$. The calculation of the effects and coefficients of the variables is then fulfilled as by full factorial design [107].

Coverage of the functionalized Au/Si substrate by nanoparticles was defined as yield by optimizing the coating processes and was determined using ImageJ software [108] after SEM[i] investigations on the samples. The uncertainty of coverage determination of the

[i] scanning electron microscopic

samples was rather large so that the full factorial design has been chosen for designing the experiments as well as a qualitative evaluation. Precise coverage calculations, due to the lack of precision, could not have been performed.

3.3.2 Spin Coated Samples

The principle of spin coating is already treated in 1.3.2. Here are some details of the spin coating steps we have taken described going over to optimization parameters choice, ending up with the qualitative influence of each parameter on the coverage of the surface.

The functionalized substrate is placed in the middle of a rotaing plate with a small vent hole through which a vacuum is drawn so that the sample does not fly away during rotation. By means of an Eppendorf pipette a defined amount of nanoparticle solution is dropped on the substrate. It is possible to let the substrate rotate at an initial speed when dropping, or start rotating after having dropped the solution, or even drop the solution while accelerating to the final speed. Thereupon, the sample rotates at its final speed for a certain time. The parameters which can be set by the spin coater are the initial speed, final speed and respective durations as well as the acceleration time in between for reaching the final speed. Furthermore, other parameters like the amount of solution dropped, as well as solvent and the concentration of the nanoparticle solution have to be studied.

Final Speed

The final speed has turned out to have a small effect on the coverage. This could be due to the fact that prior to reaching the final speed, the nanoparticle structure has reached an almost final form and then 'only' the rest of the solvent vaporizes. Fig. 3.4 makes the influence of this parameter at otherwise identical conditions clear. The $CoPt_3$ NPs can be seen as dark islands on the bright grainy surface of Au. The SAM layer can not be resolved by SEM. For small coverages one tends to the statement that in case of larger final speeds the nanoparticle islands are further apart or the nanoparticle network is thinner. In case of large coverages no differences are visible (not shown here).

Amount

If too much nanoparticle solution is droped on the substrate the excessive amount would fly away due to the acceleration. Therefore the amount merely needs to be enough to cover the whole sample. The practical values we've obtained are about 20 μl for smaller samples of $\approx 5 \times 5$ mm^2 and $30 - 40\,\mu$l for larger samples of $\approx 10 \times 10$ mm^2.

Rotating Duration

This factor has also turned out to have a small impact on the coverage. Fig. 3.5 shows different durations at otherwise identical conditions where no remarkable differences are visible. The only point of importance at this is to rotate the sample so long as the whole solvent is vaporized, as after this no changes take place on the surface of the substrate.

2000 rpm

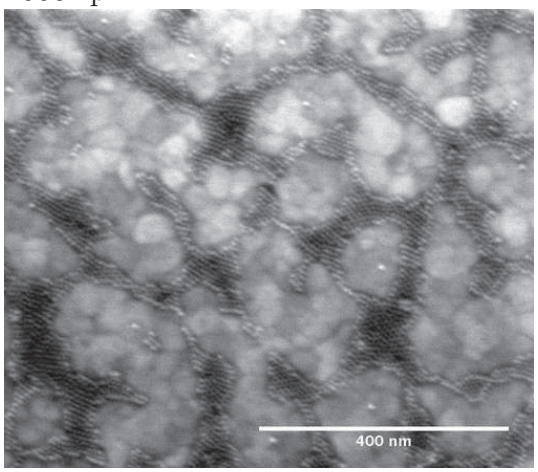

(5 s at 500 rpm, 0.9 m%, 60 s, 20 μl)

5000 rpm

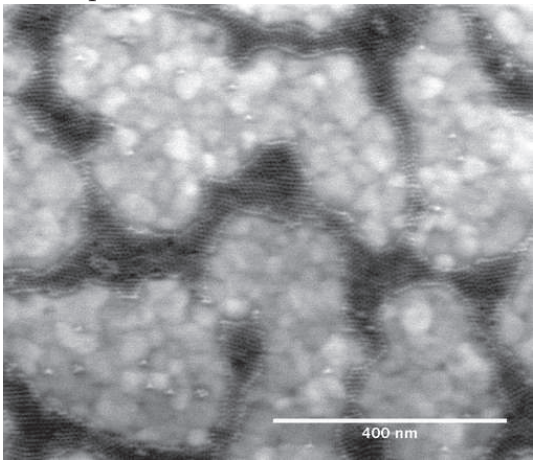

(5 s at 500 rpm, 0.9 m%, 60 s, 20 μl)

3000 rpm

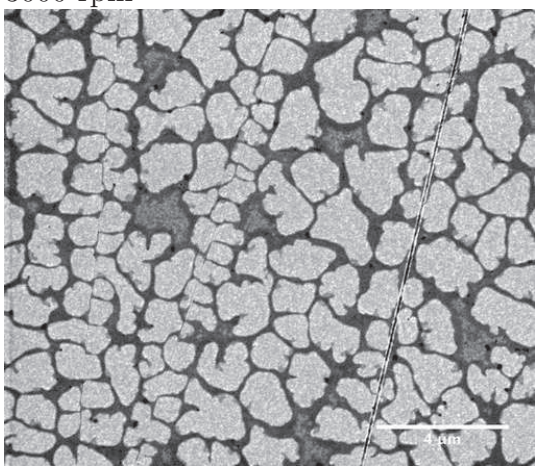

(0.45 m%, 40 s, 20 μl)‡

8000 rpm

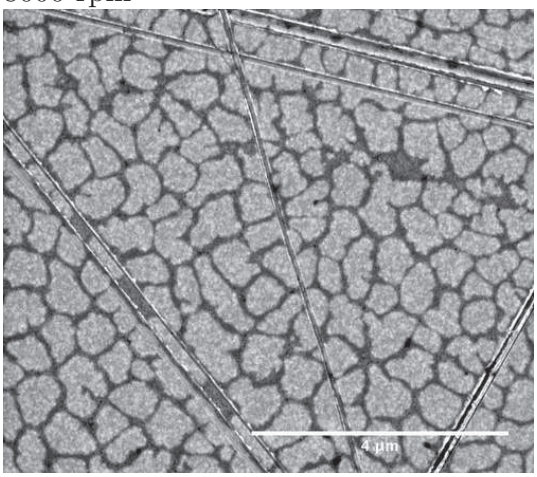

(0.45 m%, 40 s, 20 μl)‡

Figure 3.4: *Scanning electron micrographs of $CoPt_3$ nanoparticles (dark) deposited on Au (bright and grainy). Except for final speed all other parameters (initial speed, concentration, rotating duration and amount) are similar for each row of pictures.* ‡ *indincates the case as solution drop have taken place during the acceleration to the final speed and not at a constant inital speed.*

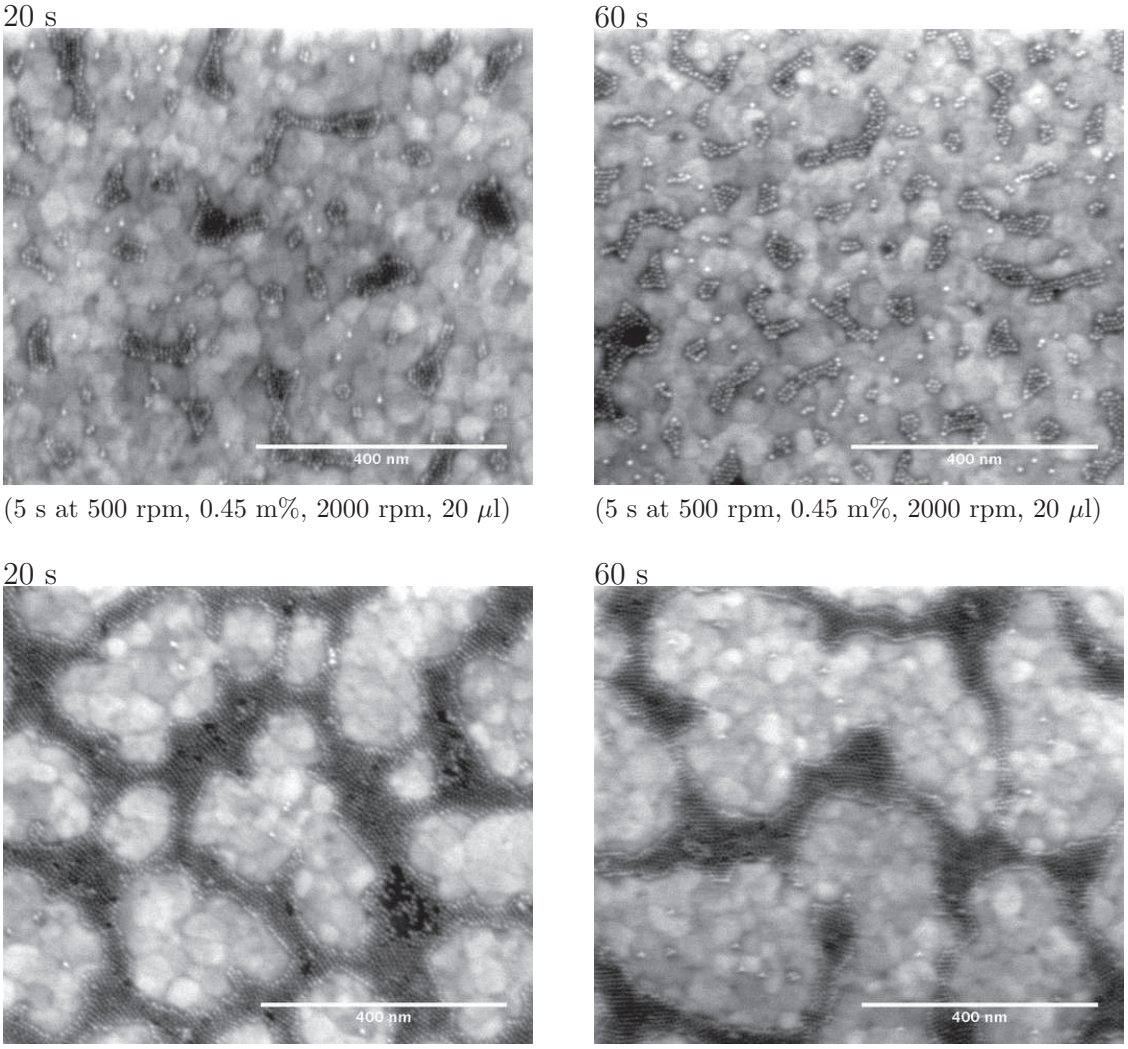

(5 s at 500 rpm, 0.45 m%, 2000 rpm, 20 μl) (5 s at 500 rpm, 0.45 m%, 2000 rpm, 20 μl)

(5 s at 500 rpm, 0.9 m%, 5000 rpm, 20 μl) (5 s at 500 rpm, 0.9 m%, 5000 rpm, 20 μl)

Figure 3.5: *Scanning electron micrographs of $CoPt_3$ nanoparticles (dark) deposited on Au (bright and grainy). Except for the rotating duration all other parameters (initial speed, concentration, final speed and amount) are similar for each row of pictures.*

Concentration

Concentration has apparently got the largest impact on the system. This does not behave linear though, i.e. by doubling the concentration the coverage is not doubled. Fig. 3.7 shows samples only different in the concentration of the solution droped. The sample prepared by 0.15 m% concentration shows a coverage[ii] of $5-10$ %. Both samples with concentrations 0.45 m% and 0.9 m% a coverage of $25-35$ %, thus to some extent the same coverage despite double concentration. The 1.35 m% sample shows a coverage of 45 %.

In case of a small nanoparticle concentration like 0.15 m%, very small domains consisting of a few nanoparticles appear. Furthermore, many separate particles are dispersed between the islands. In a nanoparticle concentration range between 0.3 m% and 0.9 m% the domains are larger and connected to each other. On the other hand if the concentration is too high (nearly 2 m%) multilayers instead of the sought monolayer are formed (cf. Fig. 3.6). Note that in non of the cases a coverage of 100 % was obtained. Even in cases where multilayers were formed, the very first layer wasn't completely closed.

The optimal concentration range is between 0.45 m% and 0.9 m%.

1.8 m%

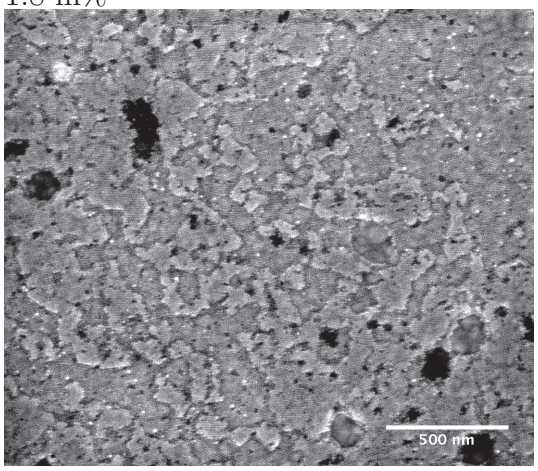

(5 s at 1000 rpm, 40 s, 4500 rpm, 20 μl)

Figure 3.6: *Multilayers of $CoPt_3$ nanoparticles due to the high concentration of the solution.*

Solvent

The properties of the solvents strongly influence the morphology of the NP domains. Hexane ($CH_3(CH_2)_4CH_3$) has got a higher vapor pressure (160 hPa @ 20°C [109]) and a lower viscosity (0.326 mPa.s [109]) than toluene ($C_6H_5CH_3$) with 29 hpa @ 20°C and 0.6 mPa.s [110], respectively. Having the nanoparticles solved in hexane the islands or networks of particles are distributed uniformly on the substrate. However, using toluene leads to branch-like multilayer forms on the susbtrate as can be seen in Fig. 3.8.
All of the nanoparticles deposited and investigted in this thesis were solved in hexane.

Initial Speed

It has turned out to be important by which conditions the nanoparticle solution is droped on the substrate as here the solution is distributed on the surface and can potentially be formed into a uniform monolayer. Three different variants were tested: droping on a substrate at rest, droping on a substrate which rotates at a constant speed of 500 rpm or 1000 rpm, and droping during the 5 seconds time as the substrate is accelerated to its final speed.
In case of a resting substrate, the solution is not distributed until the sample is accelerated

[ii]Reminder: All coverages are determined using ImageJ software, cf. Fig. 5.4.

0.15 m%

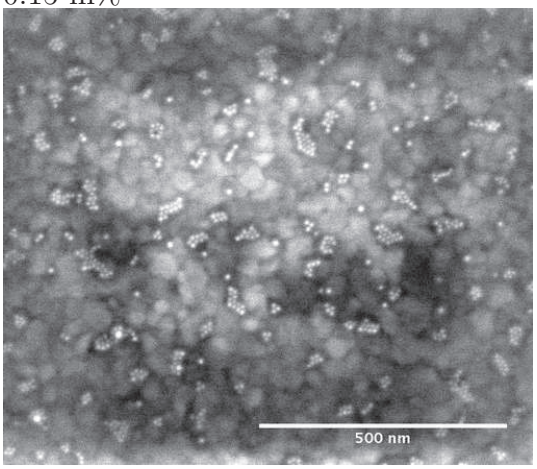

(5 s at 500 rpm, 40 s, 3000 rpm, 20 μl)

0.45 m%

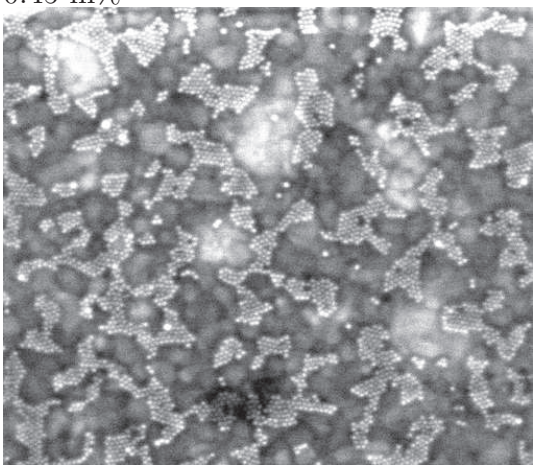

(5 s at 500 rpm, 40 s, 3000 rpm, 20 μl)

0.9 m%

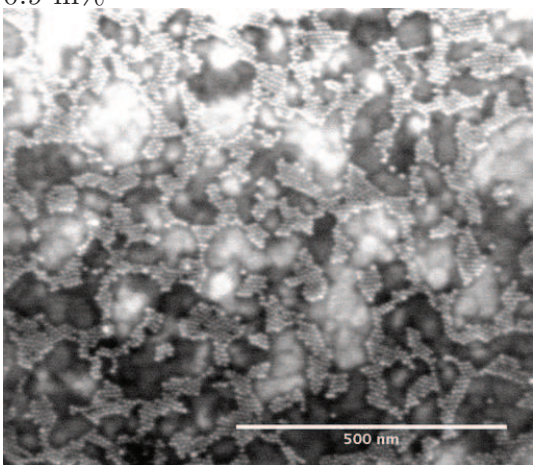

(5 s at 500 rpm, 40 s, 3000 rpm, 20 μl)

1.35 m%

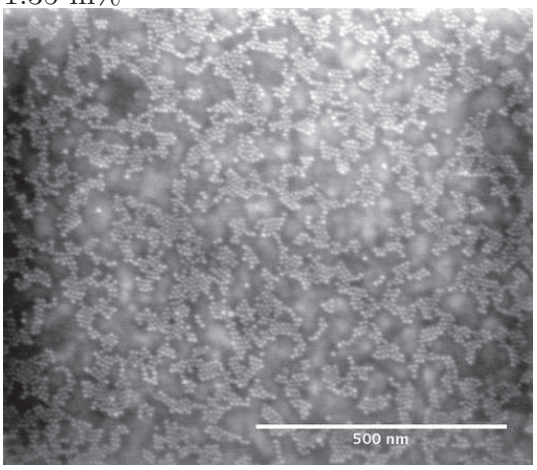

(5 s at 500 rpm, 40 s, 3000 rpm, 20 μl)

Figure 3.7: *Scanning electron micrograph of $CoPt_3$ nanoparticles (bright) deposited on Au (dark and grainy). Except for the concentration all other parameters (initial speed, rotating duration, final speed and amount) are similar for all pictures.*

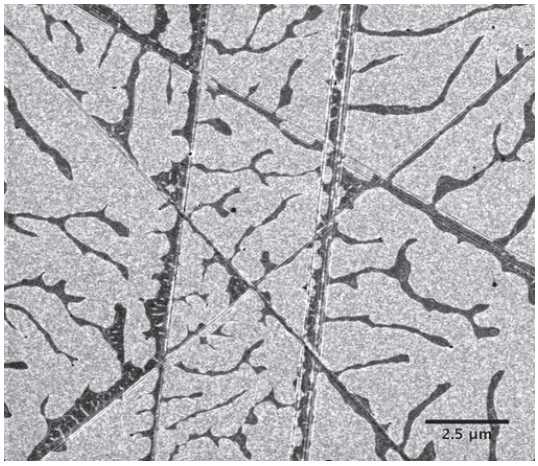

(5 s at 1000 rpm, 40 s, 3000 rpm, 20 μl)

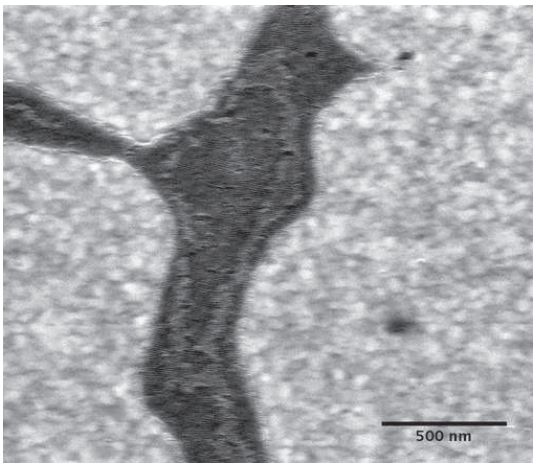

(5 s at 1000 rpm, 40 s, 3000 rpm, 20 μl)

Figure 3.8: *Scanning electron micrograph of $CoPt_3$ nanoparticles (dark) solved in toluene deposited on Au (bright and grainy)*

which leads to a very patchy coverage as well as multilayers on the surface, as can be seen in Fig. 3.9. In case of dropping on a substrate rotating at a constant speed the solution (if

not rotated by droping

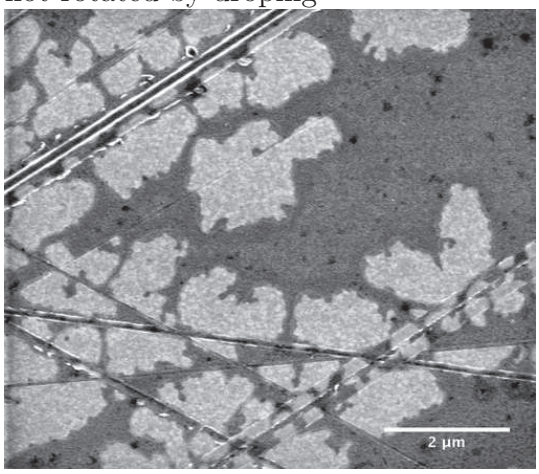

(40 s, 4000 rpm, 20 μl)

not rotated by droping

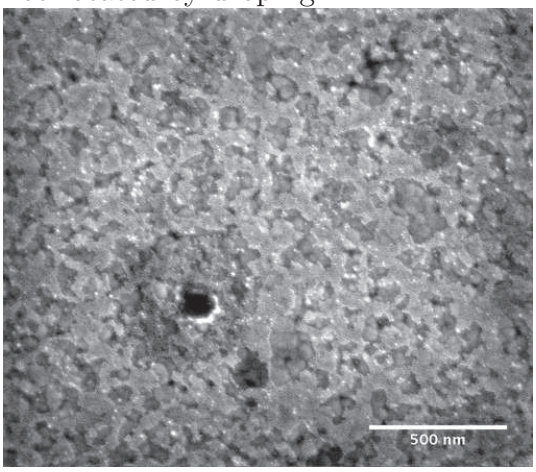

(40 s, 4000 rpm, 20 μl)

Figure 3.9: *Scanning electron micrograph of $CoPt_3$ nanoparticles (dark) solved in toluene deposited on Au (bright and grainy). A patchy multilayer is visible.*

in the optimal concentration range) is distributed homogeneously on the surface making no multilayers as has been seen in Figs. 3.4, 3.5, and 3.7 presented before.
Fig. 3.10 shows samples prepared by the same conditions except for the initial speed. As can be seen the surface coverage of the samples prepared by droping during accelerating to the final speed is network-like. This could be due to the fact that the solution is distributed very fast and some voids are originated in the film before the solvent is vaporized. Here,

some multilayer domains are also visible. In case of constant initial speed and concentrations between 0.3 and 0.6 m% monolayers are formed that have only few voids and look uniform with a locally hexagonal symmetry.

5 s acceleration

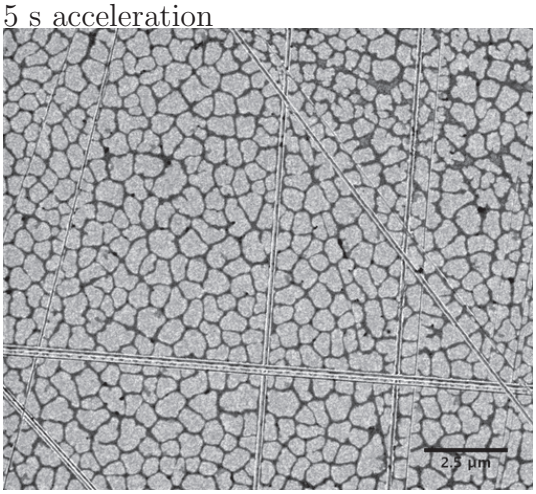

(0.45 m%, 40 s, 8000 rpm, 20 μl)

1000 rpm

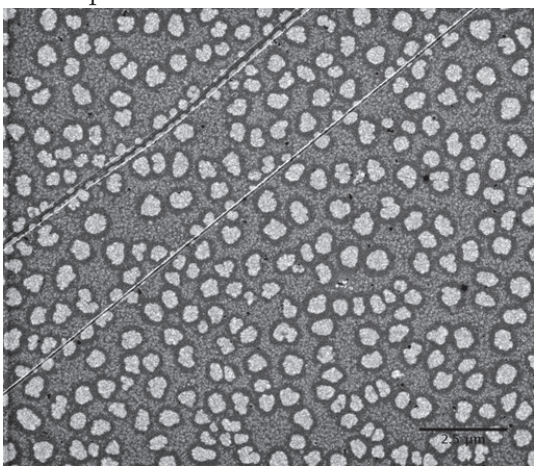

(0.45 m%, 40 s, 8000 rpm, 20 μl)

5 s acceleration

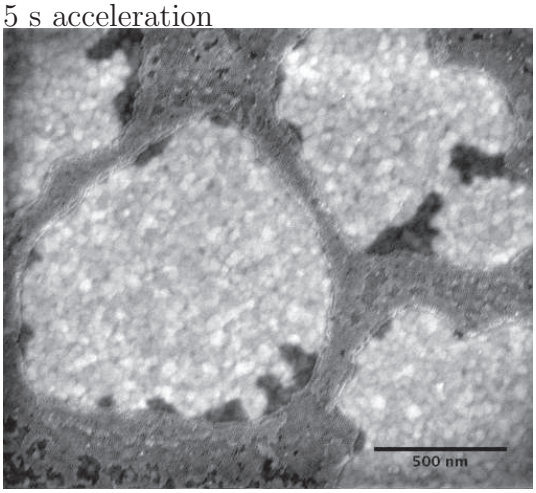

(0.45 m%, 40 s, 3000 rpm, 20 μl)

1000 rpm

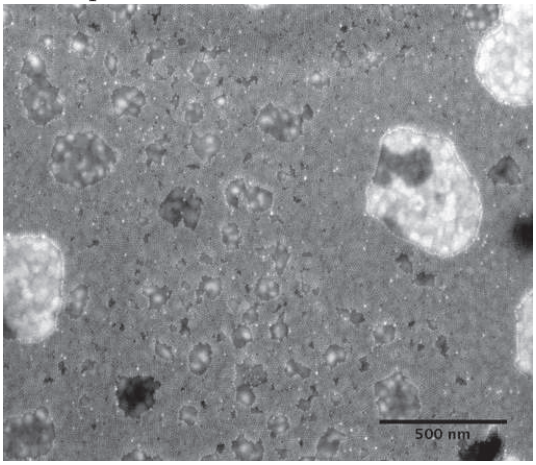

(0.45 m%, 40 s, 3000 rpm, 20 μl)

Figure 3.10: *Scanning electron micrograph of $CoPt_3$ nanoparticles (dark) deposited on Au (bright and grainy). Except for the initial dropping condition all other parameters (concentration, rotating duration, final speed and amount) are similar for all pictures.*

Synopsis

Spin coating is a fast and efficient method for depositing ordered structures of nanoparticles on a surface. Fig. 3.11 shows two of the best $CoPt_3$ nanoparticles on HDT-SAM functionalized Au-coated Si samples. As visible a very well ordered semi-closed monolayer of particles is formed which is a good requisit for performing TER-XSW as well as GISAXS investigations. In no case it was possible to reach a 100 % coverage as always some voids

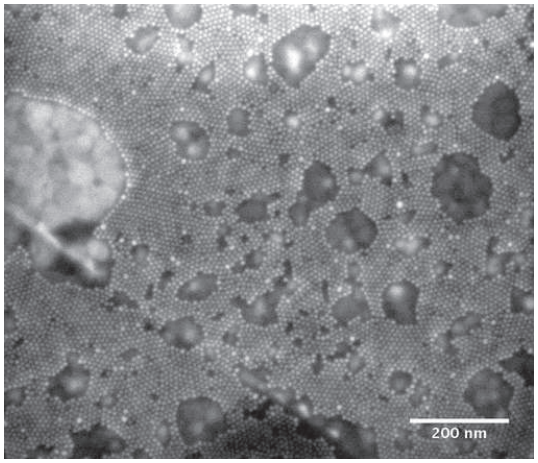

(5 s at 1000 rpm, 0.45 m%, hexane, 40 s, 3000 rpm, 20 μl)

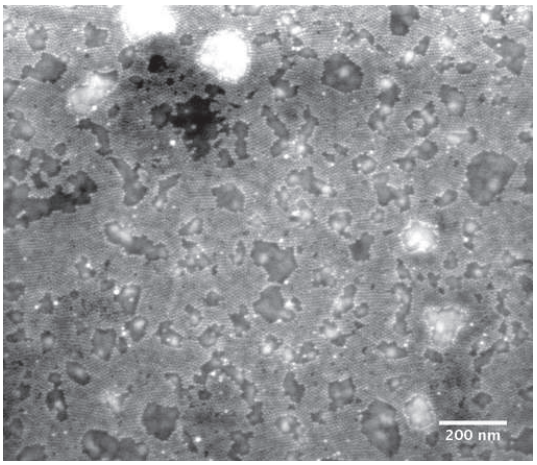

(5 s at 1000 rpm, 0.45 m%, hexane, 40 s, 8000 rpm, 20 μl)

Figure 3.11: *Two of the best $CoPt_3$ NP samples prepared by spin coating at the given conditions.*

in the layer came about. Increasing the concentration, to give an example for a possibility to increase the coverage, leads to generation of multilayers even before the first layer is completely closed. It is a general observation that even in case of samples with high density of multilayer domains, voids have been found in the first layer.

As already mentioned, the optimal nanoparticle solution concentration range is between 0.45 m% and 0.9 m% in a hexane solvent. The final speed of spin coating can be somewhere between 3000 and 8000 rpm, whereas the higher speeds tend to produce more uniform layers. As final spinning duration 40 seconds has been set in in order to make sure that the solvent is completely vaporized, even though the ordering of the nanoparticles on the substrate is not changed after 20 seconds. For the dropping condition the best results were gained when the sample was rotating at a constant speed at the moment of dropping. This initial speed must not fall below 500 rpm. The best results were achieved by an initial speed of 1000 rpm.

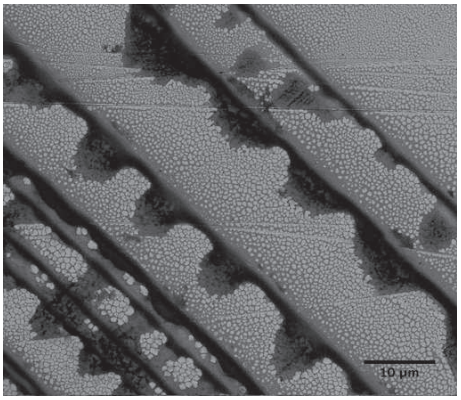

Figure 3.12: *Heaps of $CoPt_3$ NPs at an edge of a sample.*

Disadvantages of Spin Coating

A problem which emerges using spin coating is that not the whole surface of the sample gets uniformly covered, i.e., nanoparticles are heaped up at the edges of the sample (cf. Fig. 3.12). This is due to the fact that the form the solution is distributed on the square sample is because of centripetal force, circle like. On the border of this so-made circle the amount of partciles is not the same as elsewhere, which leads to formation of the mentoned nanoparticle heaps.

Furthermore, there are always problems by dropping the the solution from an Eppendorf pipette as not always the whole amount is released, and not always in the middle of the rotating sample due to the shaking hand. All these reasons lead to a partial non-reproducibility of this method, which, however, in principle could be avoided by a more reliable, automated spin coating setup.

3.3.3 Dip Coated Samples

The principle of dip coating is already described in section 1.3.3. In the present section we focus on some technical details used for depositing $CoPt_3$ nanoparticles. The dip coater has been designed and developed in our own group[iii]. The substrate can be fixed on a sample holder with a clip fixing it from the side so that the whole surface of the sample is free and can unobstructedly come into contact with the solution into which the sample is dived. A motor with adjustable speed depending on the applied voltage pulls the sample out of the solution. As we dive the samples into the solution all at once, the only parameters remaining tunable for dip coating are concentration of the nanoparticle solution as well as the speed by which the samples are pulled out (dipping speed)[iv].

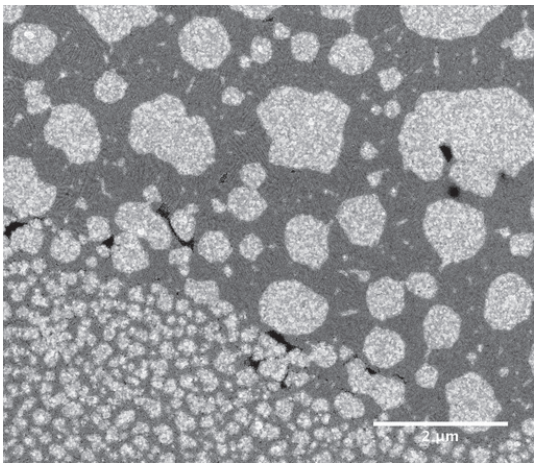

Figure 3.13: *Dipping speed of 14 mm/min by a concentration of 11.1 mmol/l leading to a high inhomogeneity of the surface coverage.*

As already mentioned, for the dip coating processes we have begun with the parameters reported in [38]. Four samples were prepared with dipping speeds of 2 mm/min and 10 mm/min each at nanoparticle solution concentrations of 2.4 mmol/l and 4 mmol/l[v] Uniform monolayers were obtained in all cases. We have also observed that the coverages of the samples prepared from solution of a concentartion do not differ from each other; and very much differ from the sample prepared with other solutions with other concentrations, so that the higher the concentration, the higher the coverage of the sample The speed of dipping has apparently an impact on the length scale of the island network of the nanoparticles and less on the coverage, as visible in Fig. 3.14. In the samples presented in the first row of Fig. 3.14 (solution concentration of 2.4 mmol/l), the one with a lower dipping speed shows a coverage of 36 % and the higher dipping speed 30 %, i.e. virtually the same coverage, if inaccuracies due to the local observation on the surface of the sample are taken into account. In the second row a coverage of 44 % for the slower and 41 % for the faster dipped samples were determined.
This increase of coverage with increasing concentration has also got upper limits. By going

[iii] For details see Appendix A.

[iv] Because of the knowledge obtained from section 3.3.2 we did not try using other solvents than hexane for the dip-coated samples.

[v] All concentrations in this section are given in mmol/l to be reconciled with [38].

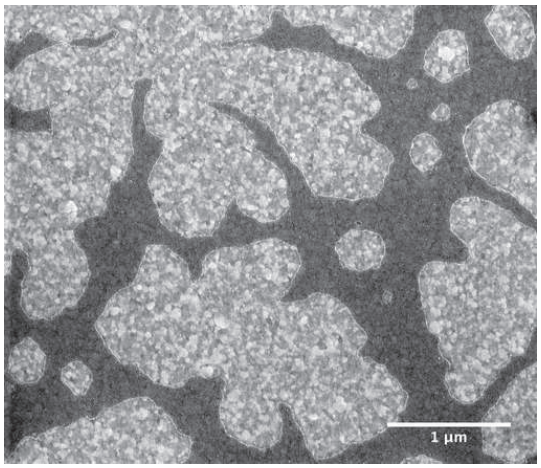

(2.4 mmol/l, 2 mm/min)

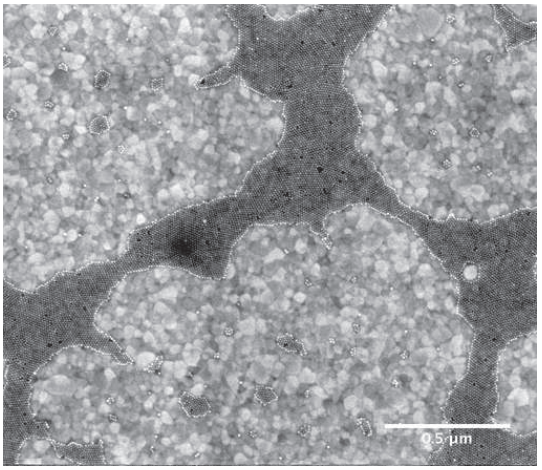

(2.4 mmol/l, 10 mm/min)

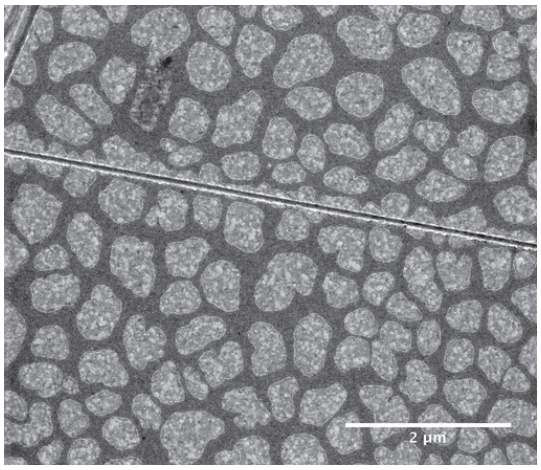

(4 mmol/l, 2 mm/min)

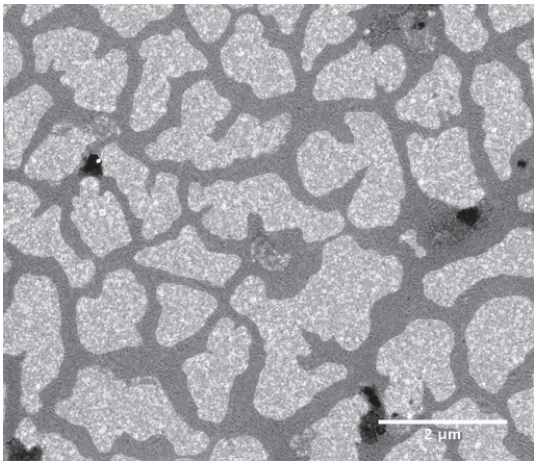

(4 mmol/l, 10 mm/min)

Figure 3.14: *Scanning electron micrograph of $CoPt_3$ nanoparticles deposited on Au by means of dip coating. In each row result for the same concentration and in each column results for the same dipping speed are shown. The coverages in each row are more or less the same even in case of relatively high dipping speeds. The speed seems to have an impact on the length scale of the domain pattern and less on the coverage.*

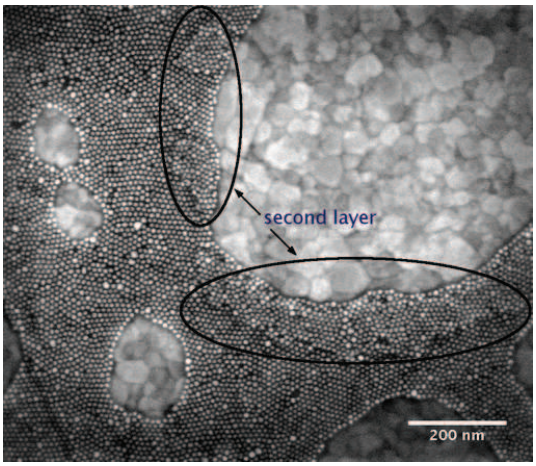

(8 mmol/l, 1 mm/min)

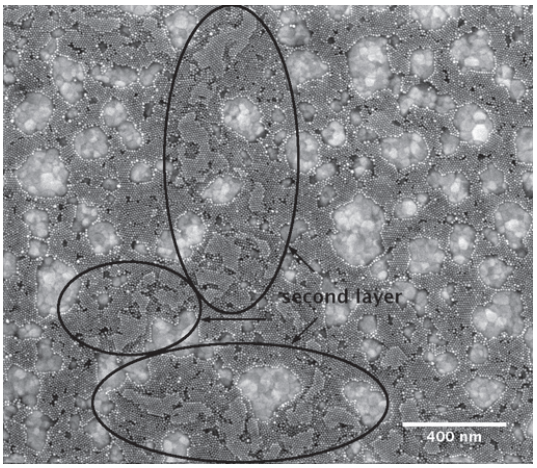

(11.1 mmol/l, 0.5 mm/min)

Figure 3.15: *Multilayers are generated in case of high nanoparticle solution concentration and low dipping speeds.*

to relatively high concentrations combined with low dipping speed, traces of forming a second layer were observed as can be seen in Fig 3.15 for two different high concentrations and low dipping speeds. In both cases a coverage of about 50 % has been reached which also can be reached by more moderate conditions (more dilute concentration and higher speeds) with the difference that multilayer formation is completely suppressed in the latter regime.
A first idea of optimizing the dip coating process was that the dipping speed could possibly compensate for the concentration. If this worked, one could prepare a relatively small amount of nanoparticle solution, dilute it so that a larger amount was resulted and go down with the speed and still gain the same coverage. This was proved not to be the case as the impact of concentration is to no extent comparable with the impact of dipping speed.

Synopsiss

Dip coating is an easy and fast method for preparing nanoparticle films on substrate. Especially in our case, for $CoPt_3$ on functionalized substrates we obtained much better results using dip coating in comparison with spin coating. The number of parameters which can influence the coverage and quality of the films are much fewer. Furthermore, there are no problems of uncertainties like the position of dropping and exact amount nor of round edges with particle heaps as it was the case by spin coating samples.
The best results obtained here were for solution concentrations between 2 and 8 mmol/l with dipping speeds of 2 to 10 mm/min, leading to uniform monolayers with different coverages. Fig. 3.16 one of the best results achieved by means of dip coating in two scales. Going too much further than the given speed leads to problems, as Fig. 3.13 demonstrates. Here, we chose a high concentration of 11.1 mmol/l and a fast dipping speed of 14 mm/min. The result is less satisfying than believed as the surface shows extremly high inhomogeneities.

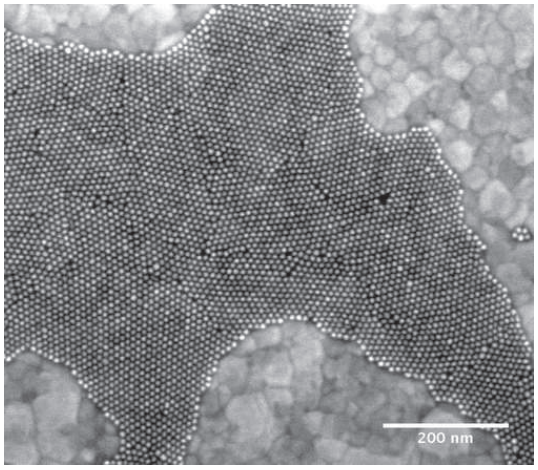

(8 mmol/l, 1 mm/min)

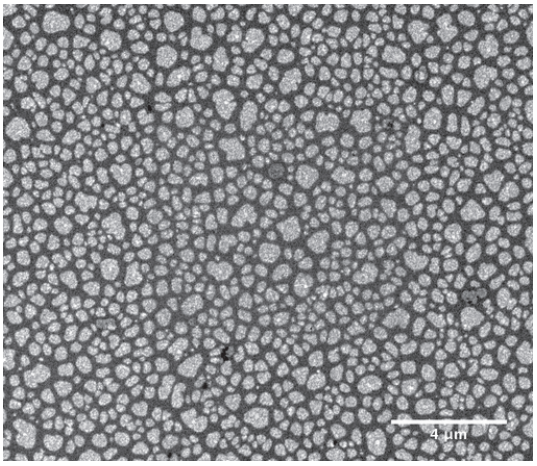

(11.1 mmol/l, 0.5 mm/min)

Figure 3.16: *Dipping speed of 6 mm/min by a concentration of 8 mmol/min*

Chapter 4

Experimental Details II (Measurement Setup and Evaluation)

In this chapter we explain some details about the synchrotron beamlines where the measurements in this work have been performed , together with information about their instrumentations. Detailed descriptions about synchrotron radion (SR) can be found in some excellent monographs like [111, 112], to name a few. The scanning electron microscope used for pre-characterization is also described here. In a last section the steps for evaluation of the measured data are introduced and explained.

4.1 Synchrotron Radiation Experiments

Most of the experiments done within the framework of this work have been based on synchrotron radiation (SR) , perfomed mainly at three beamlines, E2 (RÖMO I) and C (CEMO) at the Hamburger Synchrotronstrahlungslabor HASYLAB at the Deutsches Elektronen-Synchrotron DESY, Hamburg, Germany, and the Small Angle X-ray Scattering (SAXS) at Elettra, Trieste, Italy[i]. TER-XSW and XRR measurements and a part of the EXAFS measurements were performed at E2. CEMO is a dedicated XAFS beamline, were complementary EXAFS measurements were performed. SAXS, as can be extracted from the name of the beamline, is dedicated to small-angle scattering measurements, where we performed our GISAXS measurements. In the following some technical information to each of these beamlines are given.

4.1.1 E2 (RÖMO)

The RÖMO experimental hutch is supplied with an unfocused incident radiation originating from a bending magnet located at a distance of approximately 35 m from the station. The X-ray monochromator is a double crystal system mounted on a one-circle goniometer that can be operated in N_2 or He atmosphere. For the purpose of the measurements performed within this work, two Si (111) crystals were mounted in the monochromator.

[i]Furthermore, some investigations were performed at beamline BW1, HASYLAB, Hamburg, Germany and beamline B16 at Diamond Light Source, Oxfordshire, UK.

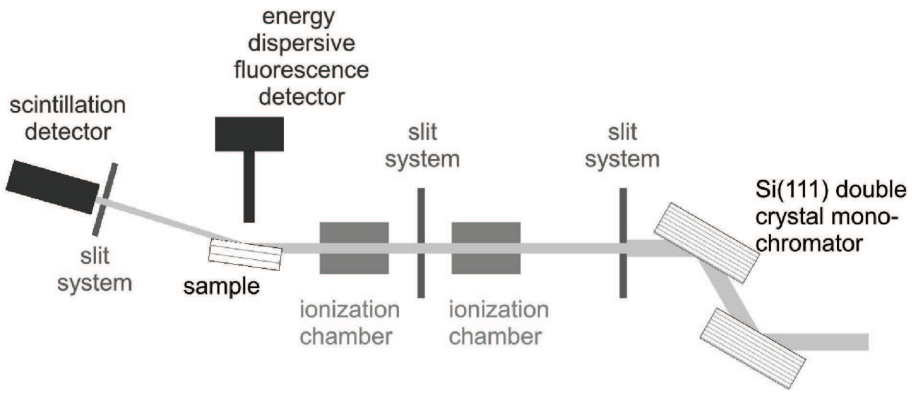

Figure 4.1: *TER-XSW measurement setup at E2 at HASYLAB, Hamburg, Germany.*

The monochromized beam has got a maximum size[ii] of about 7.6 mm (vertically) and $\approx$ 20 mm (horizontally) [113]. Two slit systems (in front of and behind the first ionization chamber) are used for cutting the beam into desired size, vertically as well as horizontally. Two ionization chambers for measuring the beam intensity are also installed in the hutch succeeded by a Huber diffractometer facilitating measurements in $\omega - 2\theta$ geometry. The sample is fixed on the Huber table performing the ω rotation. A reflectivity detector is fixed on the 2θ arm of the diffractometer equipped with an entrance slit to avoid the direct beam from hitting the detector at small angles. Fig. 4.1 shows a typical TER-XSW measurement setup at E2. As obvious, the sample surface has been brought half way into the beam such that it always, even during the ω scans up to maximum 1° floats in the beam. A photon energy of 11.7 keV was chosen for these experiments. The reason for this choice is that a minimum energy of about 11.6 keV is needed to be able to excite Pt L-edge fluorescence in $CoPt_3$ nanoparticles. On the other hand the nanoparticles are supported on Au, as already described, which has its L_3 edge at about 11.9 keV. Chosing an energy above this edge would lead to Au fluorescence, and thus would cause difficulties to seperate the two fluorescence signals[iii]. Thus, an energy in between was chosen.

Generally two detector types were used for TER-XSW:

- NaI (sodium iodide) scintillation[iv] counter detector system (Cyberstar): This detector was fixed on the 2θ arm and was used as refelectivity detector.
- Vortex silicon drift detector (SDD)[v] with multi-channel analyser: This detector was

[ii] At a photon energy of about 10 keV

[iii] Furthermore, as some measurements were performed at beamlines with Au mirrors after the monochromator (e.g. BW1, Hasylab) for suppressing higher harmonics or focussing purposes, one should remain below this limit to prevent absorption of the mirrors.

[iv] The emission of light in visible spectral range due to relaxation of excited states by radiative transitions is the property of scintillators. In a second step this light is converted into charge carriers which can then be electronically processed [114].

[v] SDD is a subclass of energy dispersive semiconductor detectors. When an electron-hole pair in depletion zone is generated by a photon, the free charge carriers are suked out in the electric field applied and generate a charge pulse in the preamplifier. In a second amplifier, these pulses are formed and further amplified succeeded by pulse hight determination, as the pulse height is proportional to the energy of the absorbed photon [114]. Further reading in [115].

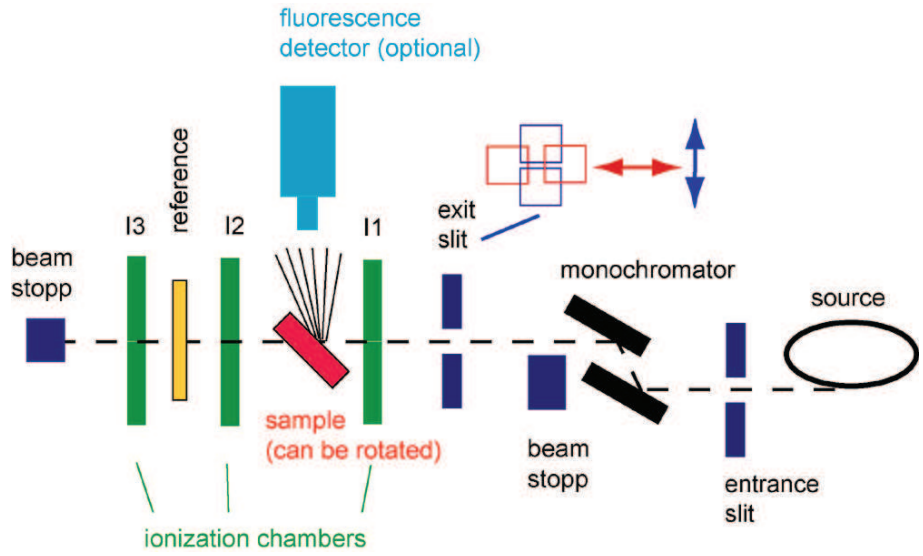

Figure 4.2: *EXAFS measurement setup at C at HASYLAB, Hamburg, Germany [116].*

mounted perpendicularly to the surface of the sample, with a collimator fixed in front of it to avoid diffuse scattering and fluorescence from the sample edges reaching the detector. The collimator basically consists of a 15 mm thick aluminum plate with a hole of 2 mm in diameter.

The EXAFS measurements at E2 were more or less carried out in the same setup, as they were performed on deposited nanoparticles on substrate, and thus, only the fluorescence signal and no transmission signal could be detected. The difference in the setup was that the NaI detector was merely used for the alignment and no grazing incidence angle condition prevailed.

4.1.2 C (CEMO)

CEMO is a bending magnet beamline dedicated to X-ray absorption spectroscopy experiments at energies between 5 and 43 keV. It is equipped with a fixed-exit double-crystal monochromator suitable for step by step energy scans. The typical beamsize at the sample is 10 mm horizontally and 1 mm vertically with a source-to-sample distance of about 30 m.

Fig. 4.3 sketches the beamline. The standard EXAFS set-up at beamline C consists of three ionization chambers which are mounted on the experimental table, where the first of them is proceeded by a double slit system for adjusting the beam size. A scroll pump and a turbo pump are installed at the beamline in order to evacuate the sample and reference sample chambers. A fluorescence detector[vi] can access the sample from the side, in case of non-transparent samples as well as in the case where an extra XAFS signal beside transmission intensity is desired. A reference foil can be mounted between the second and third ionization chamber. Each ionization chamber has got a length of 10 cm which can

[vi] We used a 7 pixel HPGe detector.

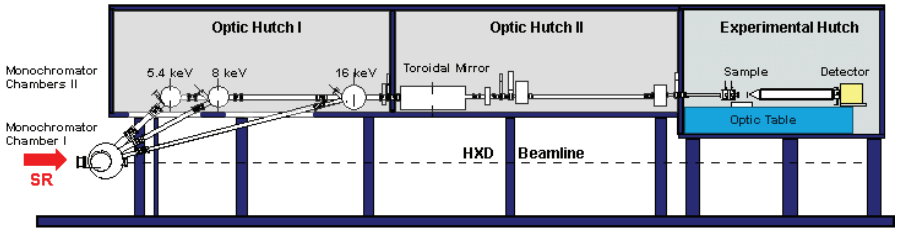

Figure 4.3: *SAXS beamline setup at Elettra, Trieste, Italy [117].*

be operated with gas filllings of N_2, Ar, and Kr between 100 and 1000 mbar, depending on the beam energy [116].

The EXAFS measurements performed at CEMO were all on nanoparticle solutions (and not nanoparticles deposited on substrates) so that the transmission signal could also be collected in addition to fluorescence.

4.1.3 SAXS

The high-flux SAXS beamline at ELETTRA is mainly intended for studies on partly ordered systems with a SAXS-resolution of 1 to 140 nm in real-space. The photon source is a 57-pole wiggler whose beam is shared and simultaneously used with a Macromolecular Crystallography beamline. From the very intense wiggler radiation, the SAXS-Beamline accepts 3 discrete energies, namely 5.4, 8 and 16 keV (0.077, 0.154, 0.23 nm). The beamline optics consists of a flat, asymmetric-cut double crystal monochromator and a double focusing toroidal mirror. The sample station is mounted movable onto an optical table for optimizing the sample detector distance with respect to SAXS resolution and sample size. The beam size at the sample is 5.4 mm horizontally and 1.8 mm vertically [117].

A two dimensional X-ray charge-coupled device (CCD) camera (Photonic Science) with an active area diameter of 115 mm with 1024×1024 pixels of 79 microns each has been used as detector. The sample-to-camera distance was 90 cm. The $\vec{q}$ space calibration was achieved using rat tendon tail (RTT) [118]. In order to optimally match the measured intensity with the given dynamic range of the CCD camera (12 bits), an aluminum absorber foil was introduced in front of the detector, suppressing the strong scattering intensity at $\vec{q}_{||} = 0$ due to the speculary reflected beam and the Yoneda peak [119] in favor of the GISAXS signal at finite values for $\vec{q}_{||}$. The photon energy used for the entire measurements was 8 keV, irradiated on the sample at grazing angles below 1° relative to the sample surface.

4.2 Scanning Electron Microscope

The scanning electron microscope (SEM) used for characterization purposes in this work is a commercial Nova 200 Nanolab, a two-beam system from FEI Company offering SEM together with a focused ion beam (FIB) to be deployed for direct structuring of microstructures. The latter property of the machine is not used within the scope of this work and therefore will not be dealt with any further at this point.

The electron column of the system is equipped with a Schottky thermal field emitter as electron gun which together with a through-the-lens secondary electron detector (TLD-SE) enables imaging of the sample down to ≈ 1.5 nm resolution. There is also an Everhardt Thornley secondary detector[vii](ET-SE) as well as a through-the-lens backscattered electron detector (TLD-BSE) used for low magnification 'search' conditions. An oil-free turbo molecular pump (TMP) together with a primary vacuum pump (PVP) pump down the system to less than 2.6e-06 mbar in less than 5 minutes [120].

All scanning electron micrographs taken during this work were in high-resolution mode by detection of secondary electrons with an acceleration voltage of 10 kV and an electron current of 0.54 nA.

4.3 XRR and TER-XSW Data Evaluation

The XRR and TER-XSW data were evaluated with a software package containing two programs *refnc* and *terxsw* developed in Fortran 77 within the context of this work (see Appendix B) as subroutines of LSFIT, a fit procedure written in University of Kiel.
For the measured data of each sample *refnc* or *terxsw* read in a configuration file (con file) which has to be generated manually. The content of each con file can be devided into 'read only' and 'modifiable' information, as the measured curve can be fitted by single or simultaneous variation of the modifiable parameter. However, information like photon energy, number of layers on the substrate, sample length and slit size are fixed and remain untouched by the routines.

The con files of both *refnc* and *terxsw* are almost the same. The mentioned read-only information are unchanged in both con files. For each layer and the substrate four different parameters have to be specified, i.e., thickness, roughness, dispersion δ (cf. Equation 2.8) and absorption β (cf. Equation 2.9). For the bulk materials dispersion and absorption remain untouched and merely thickness and roughness parameters are varied. In case of nanoparticle layers this is model dependent.

4.3.1 XRR and *refnc*

refnc calculates the reflectivity of the multilayer structure based on the Parratt formalism [81] as described in detail in section 2.1.3. The program calculates the reflected electric field E_j^r in each layer, recursively from the layer specifications given in the con file and the data gained from the previous layer, beginning from the substrate moving on toward the surface (0th layer). Reaching the surface the total reflectivity can be calculated. The roughness in each layer is assumed to be Gaussian distributed and is modelled after Névot - Croce [79, 80]

For the reflectivity, we assumed the nanoparticle film as a closed diluted bulk $CoPt_3$ layer with a specific thickness and roughness. The main factor here was the dilution which was reflected on the dispersion and absorption coefficients, i.e., a multiplying parameter was introduced which weights the dispersion and absorption values of bulk $CoPt_3$ equally.

[vii]This detector consists of a scintillator in a Farady cage and a photomultiplier, whereas the latter is outside the chamber.

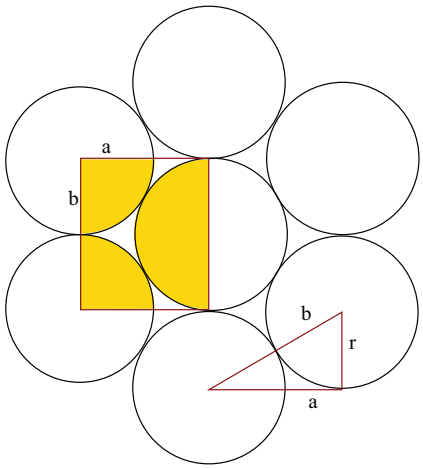

Figure 4.4: *Illustration of a monolayer of close-packed spheres in top view.* $a = \sqrt{3}r$ *and* $b = 2r$.

The weighting parameter was then determined by fitting the data and interpreted as the coverage of the surface.
Fig. 4.4 shows a cut-out of a monolayer of close-packed spheres. The rectangle shows the considered cuboid volume in plan view. The cuboid has got the edge lengths $a = \sqrt{3}r$, $b = 2r$ and $c = 2r$, whereas c is the edge perpendicular to drawing layer. As obvious one complete sphere is located in the cuboid. The ratio of sphere volume V_{sphere} to cuboid volume V_{cuboid} is the packing factor of the layer

$$\frac{V_{sphere}}{V_{cuboid}} = \frac{4\pi r^3/3}{2r \times 2r \times \sqrt{3}r} \approx 0.605. \tag{4.1}$$

A complete monolayer of the nanoparticles on the surface of the sample corresponds to a coverage of about 61%, assuming close-packed spheres. This value is obviously not the same as in case of three dimensional close-packing of spheres, where a packing factor of $\pi/3\sqrt{2} \approx 0.74$ is calculated.

4.3.2 TER-XSW and *terxsw*

terxsw calculates the fluorescence yield of each desired layer[viii] (in our case in the nanoparticle layer) based on the the Parratt formalism and the given atomic density distribution (cf. section 2.1.4). For this, both reflected and transmitted electric field, E_j^r and E_j^t in each layer have to be calculated. Similar to *refnc* this routine begins from the substrate calculating and saving the reflected electric field of each layer and moving toward the surface (0th layer) based on the information given by the con file[ix]. Then a second recursion starts calculating and saving the transmitted electic field of each layer begining from the

[viii] An extra parameter in the con file assigns the layer based on which the fluorescence yield calculation has to be performed.

[ix] The final results of *refnc* for each sample are applied into a con file and are used as input data for *terxsw*.

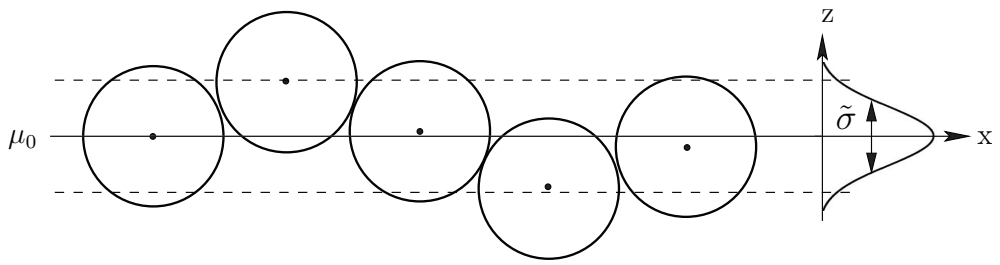

Figure 4.5: *Schematic diagram of the nanoparticle film surface model*

surface. By knowing these two the total field intensity as a function of incidence angle in each layer can be calculated (cf. Equation 2.39). The fluorescence yield is then calculated as the convolution of this intensity function with the atomic density distribution function determined in the program.

The model introduced here for the nanoparticle film is a more complicated one in comparison to the XRR case. Monodisperse spherical nanoparticles deposited on a support making a (sub)monolayer are assumed. One and each of these particles can be described by

$$x^2 + y^2 + z^2 = R^2, \tag{4.2}$$

with R the radius of the nanoparticles. A circular slice of the sphere cut out parallel to xy plane at $z = z_0$ perpendicular to z axis can be written as $x^2 + y^2 = R^2 - z_0^2 = r^2$, with r the radius of this slice. Now, if the spheres are modelled so that the position of their middle points is Gaussian distributed (cf. Fig. 4.5), this can be mathematically interpreted as a convolution of both circular and Guassian distributions. The normalized density distribution function of such nanoparticles can hence be calculated as

$$\rho(z) = \frac{\rho_0}{\pi R^2} \int_{-\infty}^{+\infty} \left[R^2 - (z-\mu)^2\right] \frac{1}{\sqrt{2\pi}\tilde{\sigma}} \exp\left(\frac{-(\mu-\mu_0)^2}{2\tilde{\sigma}^2}\right) d\mu, \tag{4.3}$$

with ρ_0 being the bulk density of the material the nanoparticles are made of, $\tilde{\sigma}$ the standard deviation of the Gaussian distribution and μ_0 its mean value. The smaller the standard deviation, the better ordered are the nanoparticles in vertical direction, so that in the optimal ordering case, $\tilde{\sigma} \to 0$, the Gaussian distribution turns to a Dirac delta distribution, and the centers of all particles are at constant height of μ_0 above the substrate. This standard deviation factor is implemented in the con file.

4.4 EXAFS Data Evaluation

For the evaluation of the EXAFS spectra the software package ATHENA-ARTEMIS was used [121] which is a front-end for IFEFFIT [122]. IFEFFIT is a collection of algorithms for XAFS evaluation reaching from raw data processing steps (ATHENA) to spectra fitting steps with help of the theoretical amplitudes and phases calculated using FEFF6 code [123] (ARTEMIS).

In order to subtract the background from each spectrum, the measured range up to 50 eV below the absorption edge was fitted with a linear function and extrapolated to the whole region. Subsequently, this was subtracted from the spectrum. In the next step a spline[x], representing the absorption spectrum of an isolated atom of the same species, was fitted into the region above the edge and consequently substracted from the spectrum. The EXAFS oscillations $\chi(k)$ were then weighted with k^2, analyzed in the k-range $4-11$ Å^{-1} for Pt L_3 and $2-10.5$ Å^{-1} for Co K-edge using a Kaiser-Bessel window. The passive electron reduction factor (S_0^2) fixed at 0.80 and 0.76 was obtained from EXAFS measurements of Co and Pt foils, respectively.

The model used to fit the experimental data was limited to the first coordination shell. Assuming the $CoPt_3$ nanoparticles to be in an ordered homogeneous fcc structure with a lattice constant of 3.854 Å [47], the Co atoms are positioned on the corners of the cube and the Pt atoms on the faces. Thus, 12 Pt atoms are positioned in the first coordination shell of Co atoms with a distance of 2.725 Å. In the same distance there are 4 Co and 8 Pt atoms in the first coordination shell of Pt.

4.5 GISAXS Data Evaluation

The GISAXS measurements were performed using a CCD camera (cf. section 4.1.3). Evaluations were performed using ImageJ software [108]. It is possible to obtain line profiles of the 2D image which is e.g. used to locate the peak positions, extracting their width and calculating distances of the maxima.

The first step of GISAXS data evaluation is to perform an angular calibration. For this we mounted a dry rat collagen as sample, as the positions of the peaks of these collagens are well-known and elaborated in the literature. Fig. 4.7 shows the scattering pattern of the collagen together with the intensity profile along the green line. The first visible accented peak is of third order. Knowing the primary spacing, $d = 660$ Å, the theoretical positions of the higher scattering [118] and the camera length, one can calibrate q-axis as follows. Keeping the Bragg's law, $n\lambda = 2d\sin\theta$, and the length of X-ray scattering vector

$$q = 2k\sin\theta = 4\pi\sin\theta/\lambda \tag{4.4}$$

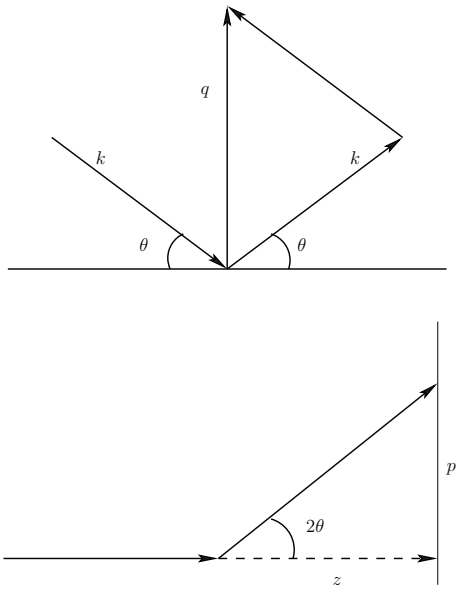

Figure 4.6: ***(Top):*** *Geometric illustration of* $q = 2k\sin\theta$. ***(Bottom):*** *The beam is diffracted through an angle of* 2θ.

as shown in Fig. 4.6, the following relation can be written

$$qd = 2\pi n. \tag{4.5}$$

An X-ray diffracted through 2θ will strike the detector at a distance p from the center, as shown in Fig. 4.6,

$$\tan 2\theta = \frac{p}{z} \tag{4.6}$$

[x]A spline of degree n is a function defined piecewise by polynomials of maximum degree n.

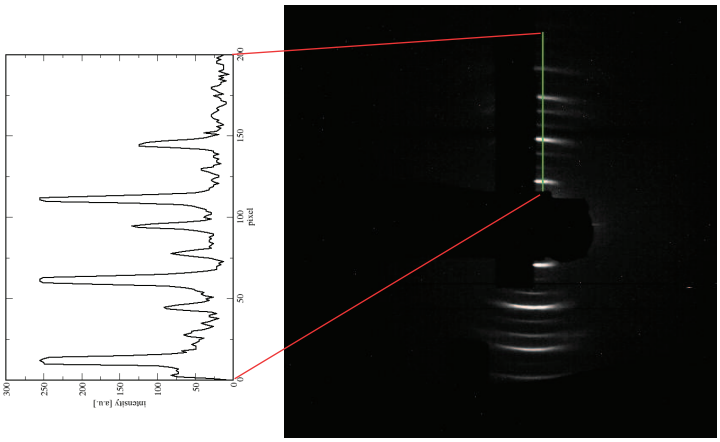

Figure 4.7: *Rat tail collagen scattering pattern together with an intensity profile along the line depicted.*

where z is the sample-to-detector distance. Approximating $\theta \approx \sin\theta \approx \tan\theta$ and equating θ in 4.4 and 4.6

$$q = \frac{2\pi p}{\lambda z}. \tag{4.7}$$

Furthermore, combining Equations 4.7 and 4.5, one can also write

$$p = \frac{n\lambda z}{d}. \tag{4.8}$$

As already mentioned, the first avisible accented peak is of third order, thus $n = 3$. Knowing $\lambda \approx 1.55$ Å and $d = 660$ Å, q is calculated to 0.28 nm^{-1} from Equations 4.7 and 4.8. Thus, each pixel on the detector screen corresponds to $5.88.10^{-3}$ nm^{-1}. In our case the CCD pictures of size 512 px × 512 px comply with 2.94 nm^{-1}× 2.94 nm^{-1}.

Chapter 5

Evaluation and Result Discussion

In this chapter we present the measured data and the evaluation results together with the corresponding discussions. Beginning with XRR, we discuss the coverage, nanoparticle size and roughnesses obtained by the evaluation. In the next step, going through TER-XSW, the mean distance of the nanoparticles to the substrate is determined. This portrays a main strength of the standing waves, being able to resolve structures in vertical direction, in comparison with e.g. microscopy. Furthermore, the ordering quality of the nanoparticle films in vertical direction is also discussed. The differences in obtained nanoparticle sizes with the sizes gained by XRR are addressed. We also show that even the internal structure of the supported nanoparticles can be investigated by TER-XSW. These results were approved by the EXAFS measurements. EXAFS data evaluation steps and results, thus, form the next section. The last section deals with GISAXS results, i.e. particle-to-particle distance and, effective ligand length determination, and lateral ordering of the nanoparticle film.

5.1 TER-XSW and XRR Data Evaluation

In the following we present the results obtained by evaluation of XRR and TER-XSW in two seperate sections followed by a consistency discussion about apparent discrepancy of the results that came out from *refnc* and *terxsw*, due to the different models implemented in these two programs.

5.1.1 XRR

Fig. 5.1 shows the reflectivity of two $CoPt_3$ nanoparticle film samples with different coverages of 53% and 33% as, to begin with, known from SEM pre-characterization, together with the reflectivity obtained from an uncovered Au/Si substrate at a photon energy of 11.7 keV (cf. section 4.1.1). Visible are the measured data and numerical fit in each case as well as three vertical lines, indicating three different critical angles as will be described in the following, including the critical angle of Au $\alpha^c_{Au} = 0.367°$.

After overcoming the total reflection regime of the Au layer an oscillation due to the Au layer thickness is visible. The small differences in the peak position of the layer thickness

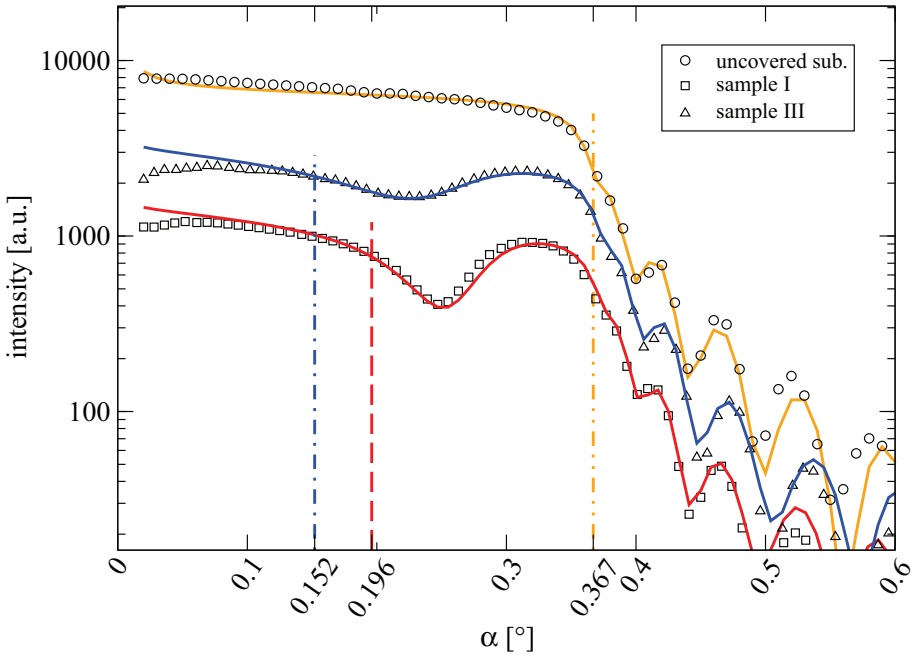

Figure 5.1: *X-ray reflectivity intensity of two samples with different coverages which lead to different crtitical angles specified on the graph together with the crtitical angle of Au* $\alpha^c_{Au} = 0.367°$.

oscilliation can be described by the fact that an Au layer thickness variation exists. By evaluation of this peak shift in the oscillating part we concluded an Au layer thickness difference of about 1.5 nm between the three samples figured[i]. Au layer thickness of sample I, $d^{sampleI}_{Au} = 360$ Å. Moreover, $d^{sampleIII}_{Au} = 345$ Å and the bare Au substrate $d^{uncovered}_{Au} = 350$ Å. It can be observed in Fig. 5.1 that the thinner the Au layer the more the oscillating peaks shift to the right.

Coverage

As already described in section 4.3.1, the model used for fitting the reflectivity data integrated in *refnc* assumes the $CoPt_3$ nanoparticle film as a compact layer with a specific thickness, interpreted as particle diameter and an effective density less than the density of $CoPt_3$[ii] hence diluted. It is known that $\varrho \propto \delta$ and $\varrho \propto \beta$, where ϱ is the partial mass density of the material, δ its dispersion and β absorption factor (cf. Equations 2.8 and 2.9). Thus, if $\varrho_{diluted}/\varrho_{CoPt_3} = r^{dil}$ with r^{dil} the dilution factor, the same factor has an effect on δ_{CoPt_3} (and also β_{CoPt_3}) and thus after Equation 2.11 on the critical angle. This means the less the coverage of the surface, the smaller the critical angle as visible in Fig. 5.1. Hence, sample I with the larger coverage shows a critical angle $\alpha^c_{sampleI} = 0.196°$ and

[i]The sample were all cut out of the same wafer. This discrepancy can be interpreted by the fact that the substrate is not covered homogeneously.

[ii]Dispersion and absorption coefficients of bulk $CoPt_3$ have been calculated to δ =1.68e-05 and β =2.87e-06, respectively [124].

sample III a critical angle $\alpha^c_{sampleIII} = 0.152°$.

The other way round, one could argument from the end of the mentioned statement to the beginning, justifiably claiming that by knowing the specific dispersion coefficient of each sample it is possible to conclude the coverage, keeping in mind that the packing factor of a single monolayer of spheres in hexagonal closest-packed structure assumed to cover a surface is 0.605.
In case of the two samples introduced in Fig. 5.1, the two dilution factors according to the numerical fit are as follows: $r^{dil}_{sampleI} = 0.35$ and $r^{dil}_{sampleIII} = 0.21$ which lead to

$$\begin{aligned} \text{coverage}_{sampleI} &= 0.35/0.605 \approx 0.58 \equiv 58\% \\ \text{coverage}_{sampleIII} &= 0.21/0.605 \approx 0.35 \equiv 35\%. \end{aligned}$$

Coverage results of the samples I and III obtained from SEM and XRR are not quite the same. Table 5.1 shows the the different coverage values obtained from these two different methods for seven samples[iii]. In all cases differences to some extent are visible.

Sample	Coverage by SEM	Coverage by XRR
I	0.53	0.58
II	0.45	0.40
III	0.33	0.35
IV	0.18	0.21
V	0.42	0.43
VI	0.42	0.27
VII	0.51	0.48

Table 5.1: *Surface coverage of investigated samples obtained from SEM micrographs as well as XRR measurements. Here, 1.0 means a complete surface coverage. As measurement errors 10% for SEM and 2% for XRR are assumed.*

The scanning electron micrographs used for determining the coverage are mainly from the middle parts of the respective samples, as there a more uniform coverage was available. However, sometimes on the edges of the samples, large deviations from the middle point are visible (cf. Fig. 5.2), such that completely uncovered as well as completely covered regions are observable, the latter often showing strong indications of multilayers. This could lead to inaccuracies in the coverage results of this method. Nevertheless, SEM coverage determination method has turned out to be a liable preliminary coverage determination method as Fig. 5.3 shows. The content of Table 5.1, i.e. coverages obtained by SEM versus coverages obtained by XRR, is depicted here together with a linear fit through the data points. The slope of the mentioned linear fit is equal to unity which indicates the good agreement of the results obtained by either of the methods within the measurements accuracy.

In order to determine the coverage from the scanning electron micrographs, the con-

[iii] The results of investigations on these very samples will be consequently presented in this section.

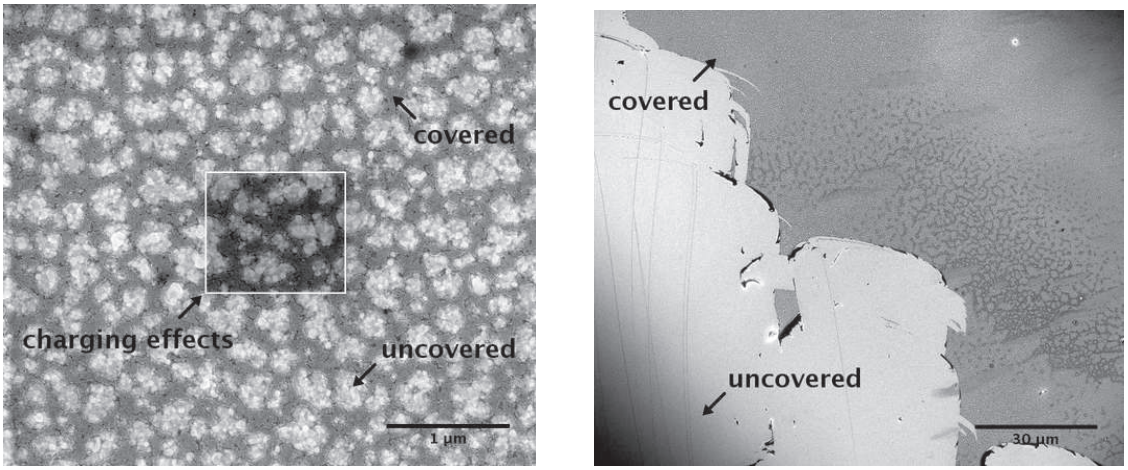

Figure 5.2: *Scanning electron micrograph from* ***Left:*** *the middle of a sample where a uniform coverage can be observed;* ***Right:*** *the edges of the sample show partially a high coverage and partially no coverage at all. The marked square indicates the charging effects of the SEM as we have zoomed in this region. This is due to the insulation of the SAM layer.*

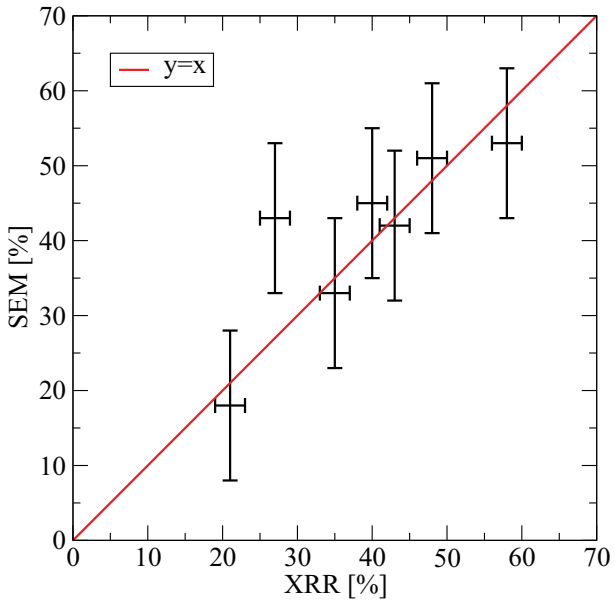

Figure 5.3: *Coverages determined by SEM vs. XRR with measurement errors of 10% and 2%, respectively.*

trasts of the pictures were modified such that the nanoparticles appeared white and the background dark. From the ratio of the black to the white pixels, which can be counted automatically by ImageJ, the surface coverage can be determined. An example of the procedure is depicted in Fig. 5.4.

Mean Particle Size

As in case of coverage we have determined the $CoPt_3$ nanoparticle size by means of SEM in pre-characterization steps using ImageJ. Following this intention we have made up an average of at least 10 individual measurements to come to an averaged nanoparticle size. Fig. 5.5 shows the determination of nanoparticle size from a scanning electron micrograph. The nanoparticle sizes of each sample obtained from SEM can be seen in Table 5.2. The measurment error of the diameter of the particles is due to observation inaccuracies and has been assumed to be 5 Å.

For all the samples discussed here, the mean nanoparticle diameters are in a narrow range

Sample	Average Diameter [Å]
I	85 ± 5
II	88 ± 5
III	83 ± 5
IV	83 ± 5
V	85 ± 5
VI	86 ± 5
VII	85 ± 5

Table 5.2: *List of the mean diameter size of $CoPt_3$ nanoparticles measured by means of SEM.*

from (83 ± 5) Å to (85 ± 5) Å.

The nanoparticle size determination by means of XRR was also performed using the model introduced in section 4.3.1. Here, we have taken a four-layer system as a basis consisting of the $CoPt_3$ layer, the SAM layer, the gold layer and the titanium adhesive layer. Thus, it is possible to determine the thickness of each of the mentioned layers by evaluating the reflectivity data. Table 5.3 shows the the $CoPt_3$ nanoparticle film thicknesses, the roughness of this layer together with the SAM layer thickness and Gold layer roughness. Despersion and absorption values of the SAM layer were assumed to be zero (vacuum values)[iv], so that this layer can be understood merely as a spacer with a specific thickness which is due to the conveyed Au layer roughness, not same high everywhere.

The thicknesses obtained by XRR are obviously smaller than the thicknesses mea-

[iv] This is a good proximity for the photon energy applied here, as the HDT has got a very low density and is effectively invisible for the beam.

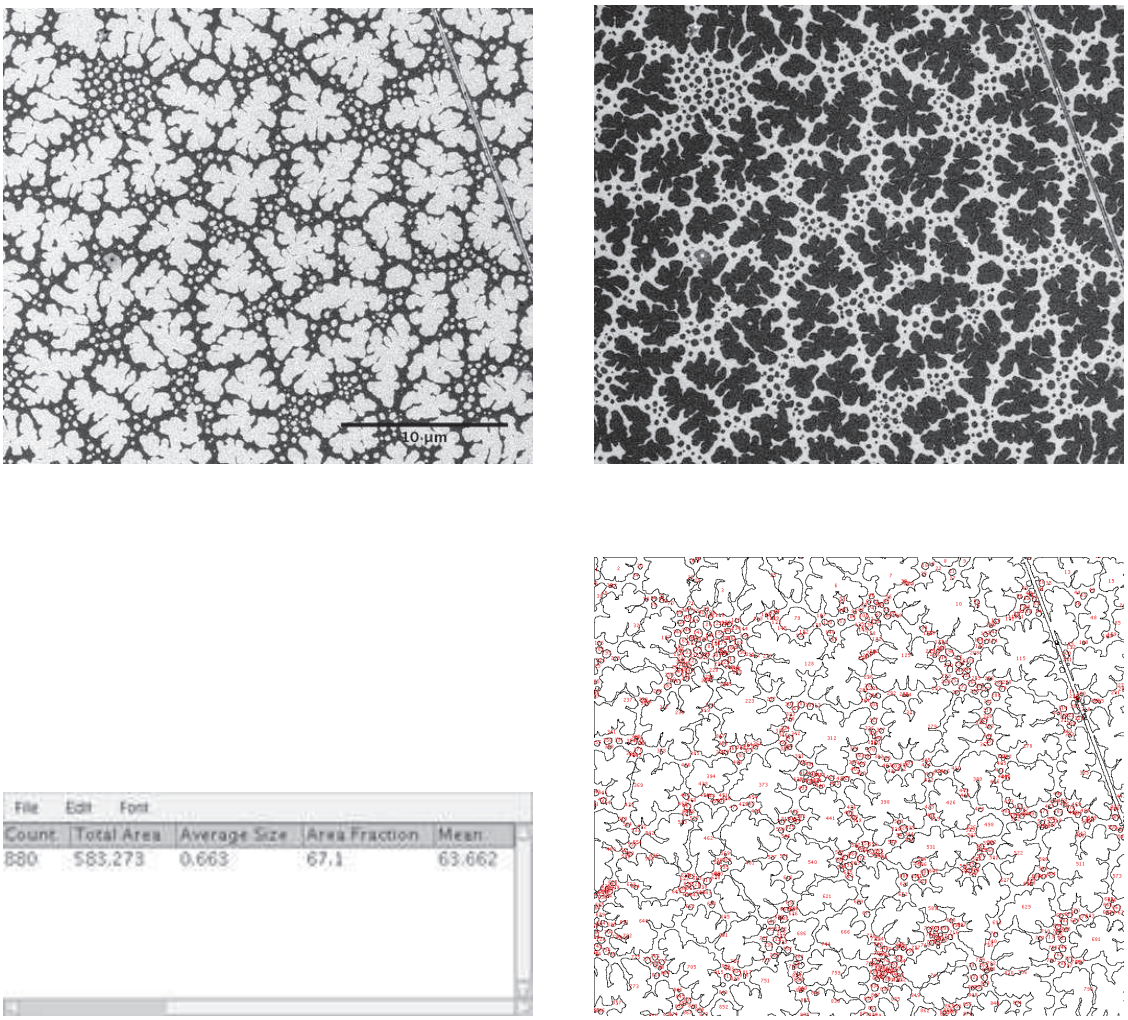

Figure 5.4: *Steps of surface coverage determination out of scanning electron micrographs using ImageJ on the example of sample III. The top left picture shows the micrograph as taken. In the top right picture the contrast is changed such that the nanoparticles are completely distinguished from the background (in this case Au). ImageJ then forms the boarders of the nanoparticle islands as can be seen in the botoom right picture and calculates, among others, the area fraction of the covered surface with respect to the total surface. This is in this specific case* $\approx 67\%$ *as seen in the bottom left frame, a snap shot of the active ImageJ window.*

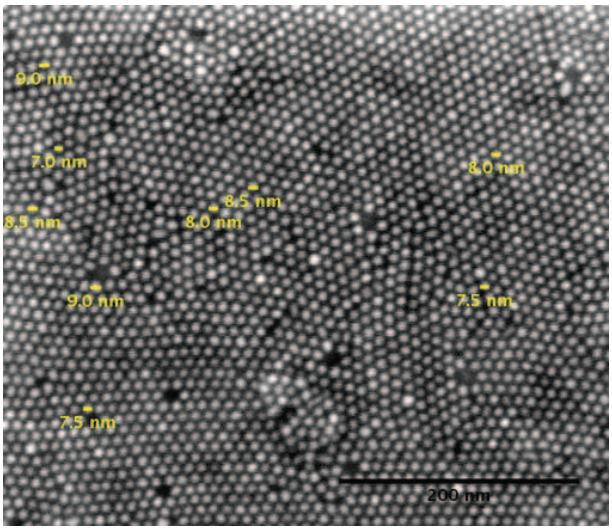

Figure 5.5: *Example of nanoparticle size determination out of a scanning electron micrograph of sample IV.*

Sample	$d^{XRR}_{CoPt_3}$ [Å] ±2 Å	$\sigma^{XRR}_{CoPt_3}$ [Å] ±2 Å	d^{XRR}_{SAM} [Å] ±2 Å	σ^{XRR}_{Au}[Å] ±2 Å
I	75	10	21	12
II	92	10	19	8
III	68	5	30	11
IV	75	12	29	11
V	75	5	23	12
VI	80	5	20	8
VII	65	15	21	11

Table 5.3: *$CoPt_3$ film layer thickness d_{CoPt_3} and SAM thickness d_{SAM} together with nanoparticle film and gold layer roughnesses σ_{CoPt_3} and σ_{Au}, respectively, as determined from XRR.*

sured from scanning electron micrographs due to the underlying model. In case of evaluation of reflectivity data the nanoparticles are assumed as closed box-shaped layers with a Gaussian-distributed roughness with standard deviation $\sigma^{XRR}_{CoPt_3}$ after Névot-Croce. The real layer consists of sphere-shaped particles, though. It is conceivable that the simplification assumed in the model constitutes a box-shaped cut out of the sphere-shaped layer and the cut-out spherical shape is interpreted as roughness. Thus, the effective layer thickness after this model is assembled by adding the thickness and the surface roughness, $d^{XRR}_{CoPt_3} \pm \sigma^{XRR}_{CoPt_3}$.

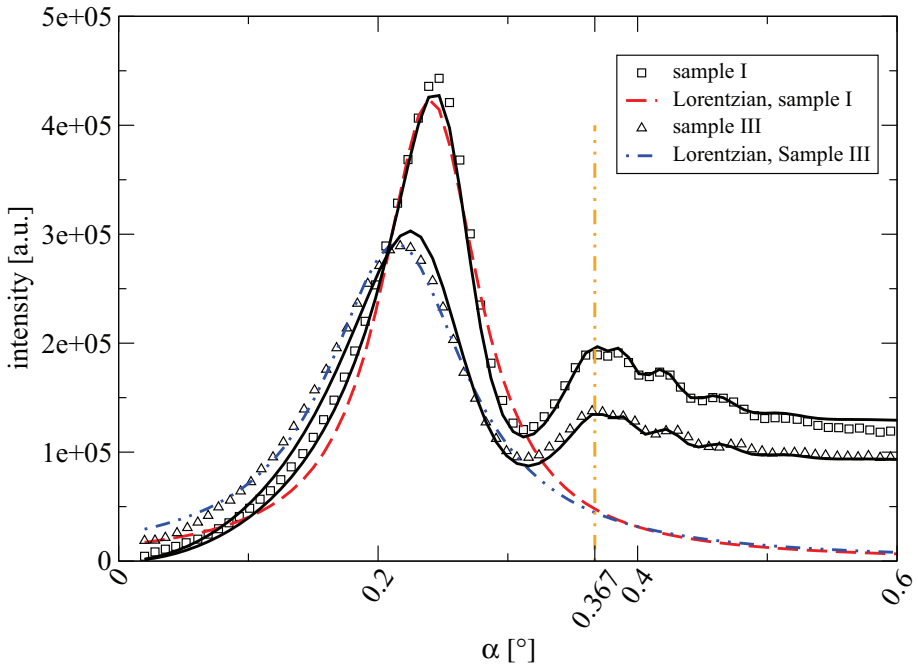

Figure 5.6: *Pt fluorescence by TER-XSW measurements on two samples with different coverages. Curves are fitted with Lorentzian functions in order to extract HWHM. Sample with low coverage (sample III) shows with* $HWHM_{sampleIII} = 0.065°$ *a broader curve than sample I,* $HWHM_{sampleI} = 0.047°$*. The critical angle of Au,* $\alpha^c_{Au} = 0.367°$ *is also indicated.*

5.1.2 TER-XSW

Fig. 5.6 shows a typical fluorescence curve obtained by TER-XSW measurements, in this case Pt fluorescence. The curve rises fast in the beginning as the sample is rocked over into the beam and the first intensity maximum of the standig wave field gets through the nanoparticles. After the first intensity maximum has passed through the middle of the $CoPt_3$ nanoparticle layer, the fluorescence yield drops and rises again shortly before reaching the critical angle of Gold. The second intensity maximum enters the nanoparticle layer here which cannot show any characteristic like the first peak because the standing wave field practically disappears after leaving the total external regime by exceeding the critical angle. The oscillations visible above the critical angle are due to the layer thickness oscillations in the reflectivity, as the fluorescence yield is mathematically a convolution integral of the intensity of the standing waves field and the material density. As the intensity depends on by the sample reflectivity (cf. section 2.1.4), these XRR oscillations are conveyed to the fluorescence yield.

In the $\alpha > \alpha^c_{Au}$ region where the sample turns increasingly into the beam and thus more intensity of the primary beam for fluorescence excitataion is available, one expects that the fluorescence yield rises. This is apparently not the case which is presumably due to the utilization of the collimator infront of the fluorescence detector (cf. 4.1.1) strongly restricting the acceptance angle of the detector. This restriction is possibly so strong that the photons with maximum energy leaving the surface prependicularly do not reach the

detector any more. Instead, only the photons with increasingly larger angle to the surface can reach the detector through the collimator. The combination of this increasing shielding effect and simultaneously increasing photon intensity could possibly explain the constant intensity of the curve.

Ordering and Coverage

As also indicated in the inset of Fig. 5.6 two Lorentzian functions[v], for illustration, have been fitted into the Pt fluorescence curves of each sample with scale parameters γ_I and γ_{III}, respectively. The ratio of the γ values of the two samples is $\gamma_I/\gamma_{III} = 0.72$ meaning that the fluorescence curve of the first sample is narrower. As obvious from the curve, the first antinode of the standing waves stimulated Pt fluorescence sooner by sample III than sample I. This is an indication for having the nanoparticle film in a better vertical ordering. This argumentation is based on the model introduced in 4.3.2. As already mentioned there, σ is standard deviation of the Gaussian distribution which the ordering of the film obeys. Table 5.4 shows that the grade of ordering is directly proportional to coverage of the samples. With increasing the grade of surface coverage the island structures on the surface get larger and more networked. This is possibly the reason for accruement of better defined nanoparticle distribution on the surface, i.e., the nanoparticles stabilize themselves more and more the more covered the surface is. This is possibly due to the ligand-ligand as well as ligand-SAM interaction. This means that in case of higher coverages the vertical position of single nanoparticles and thus their distance to the substrate is closer to the expected value of the Gaussian distribution, as the variance of the distribution gets smaller.

Sample II constitutes the only exception which could be due to the fact that in this case multilayers are built which cannot be implied into the proposed model and would be interpreted as a strong deviation of nanoparticles' midpoint around the average distance to the gold surface. Another indication for existance of multilayers in case of sample II is the large particle sizes obtained by XRR (cf. Table 5.3) and by TER-XSW (cf. Table 5.5), although the average particle size of this sample should be exactly the same as in other cases. SEM is seldom an appropriate method for determining the existance of such monolayers, as its operation range is very local.

Vertical Resolution

As the first step here we introduce the nanoparticle sizes obtained as well as the mean SAM layer size which simultaneously indicates the mean $CoPt_3$ nanoparticle distance to the surface in Table 5.5.

The nanoparticle sizes obtained by this method are, within the error bar comparable with the values obtained from SEM and therefore show discrepancies to corresponding values extracted from XRR data, as already discussed in section 5.1.1.

[v] Lorentzian function is a singly peaked function given by
$f(x) = \frac{1}{\pi}\left[\frac{\gamma}{(x-x_0)^2+\gamma^2}\right]$,
with x_0 is the location parameter and γ the scale parameter specifying the half-width at half-maximum (HWHM).

sample	coverage [%]	σ_{Pt} [Å]	σ_{Co} [Å]
I	55.5	1.4	1.7
VII	49.5	1.9	2.1
V	42.5	2.0	2.0
II	42.5	4.5	2.9
VI	35	2.0	2.2
III	34	2.9	2.6
IV	19.5	3.0	2.7

Table 5.4: *Standard deviation of the NP height distribution (see model in section 4.3.2) derived from both Pt and Co fluorescence data. The specified coverages are mean values extracted from XRR and SEM coverages. The higher the coverage is, the smaller is the standard deviation of the NP height. The only exception is sample II.*

Sample	$d_{CoPt_3}^{Pt-fluo.}$	$d_{CoPt_3}^{Co-fluo.}$	$d_{CoPt_3}^{TER-XSW}$	$d_{SAM}^{Pt-fluo.}$	$d_{SAM}^{Co-fluo.}$	$d_{SAM}^{Co-fluo.\&XRR}$
I	83	92	87.5	32	25	23
II	90	97	93.5	26	25	22
III	82	90	86	29	25	27.5
IV	83	93	88	26	22	25
V	84	90	87	30	25	24
VI	79	89	84	30	26	23
VII	80	92	86	26	20	20.5

Table 5.5: *$CoPt_3$ mean nanoparticle size and SAM thicknesses obtained from TER-XSW measurements. $d_{CoPt_3}^{TER-XSW}$s are the average values of thicknesses gained by Pt fluorescence signals for $CoPt_3$. $d_{CoPt_3}^{TER-XSW}$s are the SAM thicknesses gained by averaging over $d_{SAM}^{Co-fluo.}$ and d_{SAM}^{XRR}. All values are in Å with an error of 2 Å in each case.*

Furthermore, comparing the two fluorescence intensity curves of Co and Pt, it becomes obvious that the Co fluorescence yield in TER regime is always wider in comparison to the Pt fluorescence yield as can be seen in Fig. 5.7. This fact together with the smaller peak-to-valley ratio of Co fluorescence can be due to core-shell-like structure of nanoparticles instead of presumed homogeneous $CoPt_3$ fcc structure. Table 5.5 shows that the thicknesses attained by evaluating the Co fluorescence are on average about (9 ± 2) Å thicker than in case of Pt fluorescence. Hence, it can be claimed that a spherical shaped region with a thickness of about (4 ± 2) Å around the circumference of the nanoparticles containes mainly Co atoms. This result has been approved by the EXAFS measurements (cf. section 5.2).

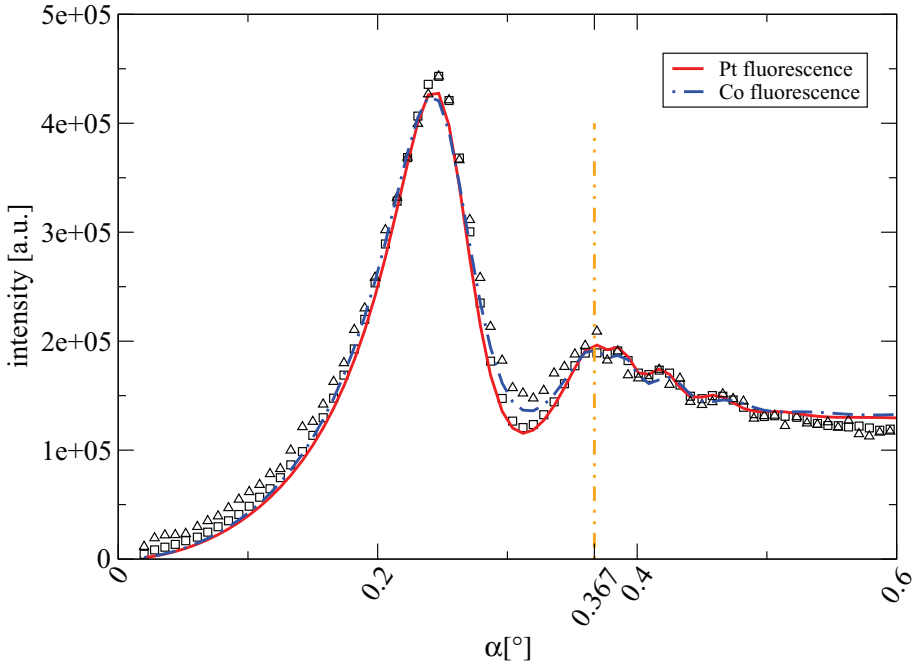

Figure 5.7: *Co and Pt fluorescence of one and the same sample. The Co intensity curve is normalized such that both peaks correspond. It is obvious that the Co curve has got a larger FWHM and a smaller peak to valley ratio than the Pt curve. The critical angle of Au,* $\alpha^c_{Au} = 0.367°$ *is indicated.*

Consequently, when the first XSW antinode approaches the surface, it first confronts Co atoms in the shell of the structure and later on the mixed Co-Pt. Knowing this, one can extract the average SAM layer thickness from the known thicknesses out of XRR and Co-fluorescence evaluation as also listed in table 5.5. According to that, the mean thickness of all SAM layers is 24 ± 3Å. It is known from 1.3.1 that the effective thickness of this layer is about 21 Å. Thus, it can be concluded that HDT molecules of the SAM layer and the ligand layer of the nanoparticles interlock and this makes the nanoparticles stand in average higher than the effective thickness of the SAM layer itself.

5.2 EXAFS Data Evaluation

The EXAFS measurements were performed on $CoPt_3$ nanoparticle solutions as well as deposited $CoPt_3$ nanoparticles on functionalized Au coated Si substrates as alreday described in section 4.1 in detail. The EXAFS oscillations $\chi(k)$ were obtained by subtracting the pre-edge background, normalizing to the experimental edge step and subtracting a smooth atomic background from normalized absorption data using the ATHENA program [122].

Based on the model introduced in section 4.4, and assuming the $CoPt_3$ nanoparticles to be in an ordered homogeneous fcc structure, the first evaluation steps were taken without leading to satisfactory results. The best fit of the Fourier transform at the Co K-edge for $CoPt_3$ nanoparticles, using 12 Pt-atoms in the first coordiantion shell with a distance of

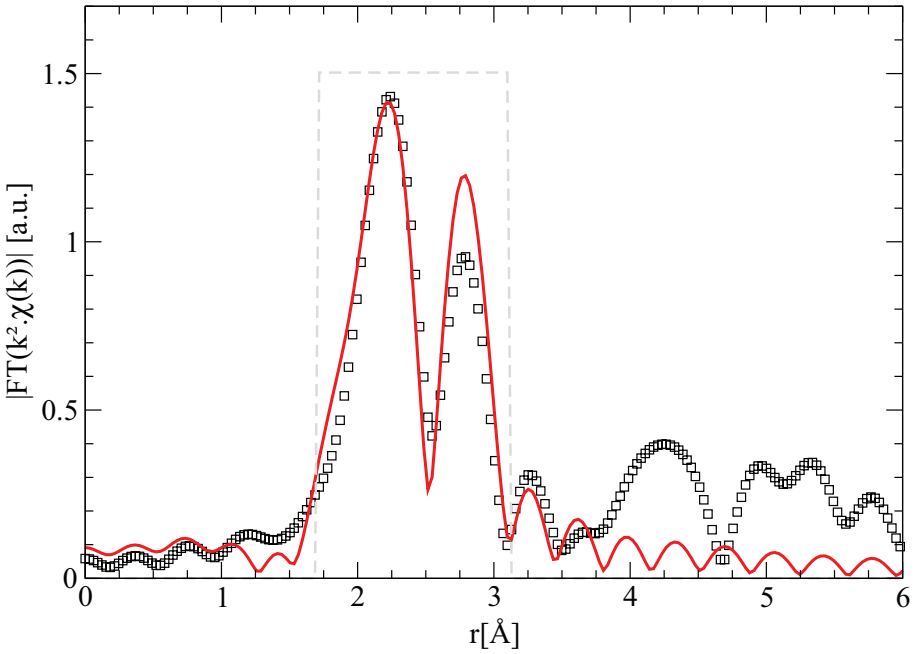

Figure 5.8: *Radial distribution (RDF) of the first coordination shell fit of Co atoms for an ordered $CoPt_3$ fcc structure. The window models the range of the first coordination shell.*

2.725 Å can be seen in Fig. 5.8.

Therefore, we modified the structural model for the EXAFS evaluation, keeping the total number of atoms in the first coordination shell of Co at 12 and allowing an arbitrary mixture of Pt and Co neighbors in this shell. Fig. 5.9 shows the result obtained with this model, and as obvious, a much better data fit is achieved in this case having Co as well as Pt in the direct neighbourhood of Co atoms. Here, we came to the best result having ≈ 7 Pt and ≈ 5 Co atoms in the first coordination shell of Co atoms.

On the other hand, Pt L_3 edge is evaluated, at the first step also based on the preliminary $CoPt_3$ fcc structure with Pt having 4 Co and 8 Pt atoms in the first coordination shell with a distance of 2.725 Å. For the fitting procedure we kept the total number of atoms in the first coordiantion shell constant (12 atoms) and tried to find the best combination. Fig. 5.10 shows the result of this procedure, having 10.4 Pt and 1.6 Co atoms in the first coordination shell.

The parameters obtained for Co K- and Pt L_3-edge are collected in Table 5.6 together with the quality of the fit (R-factor).

Within the error bars the Co-Pt and Pt-Co distances, 2.69 Å and 2.70 Å, respectively, match each other and are slightly smaller than in the ordered $CoPt_3$ bulk system, 2.725 Å. The Pt-Pt distance was found at the 2.73 Å that correspond to distance in bulk $CoPt_3$. The Co-Co distance is significantly different from that in $CoPt_3$. However, in case of fcc $CoPt_3$ the Pt-Pt and Co-Co distances should be the same.

The relatively large value of the Debye-Waller factor, σ^2 and unexpected concentration, x can be explained by non-homogeneous distribution of Co atoms in the $CoPt_3$ nanopar-

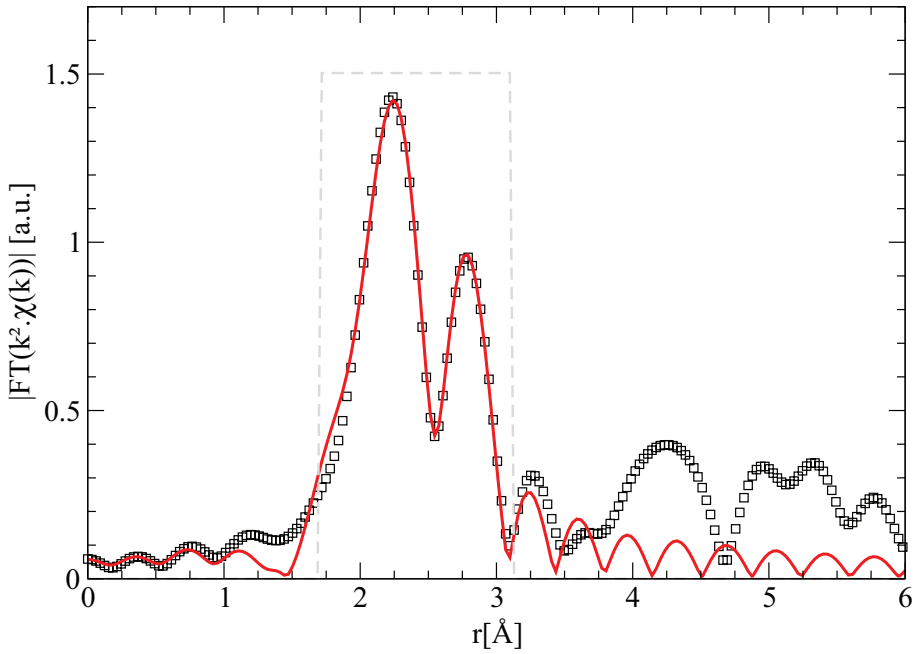

Figure 5.9: *Radial distribution (RDF) and the best fit of the first coordination shell for $CoPt_3$ nanoparticles at Co K-edge. The window models the range of the first coordination shell.*

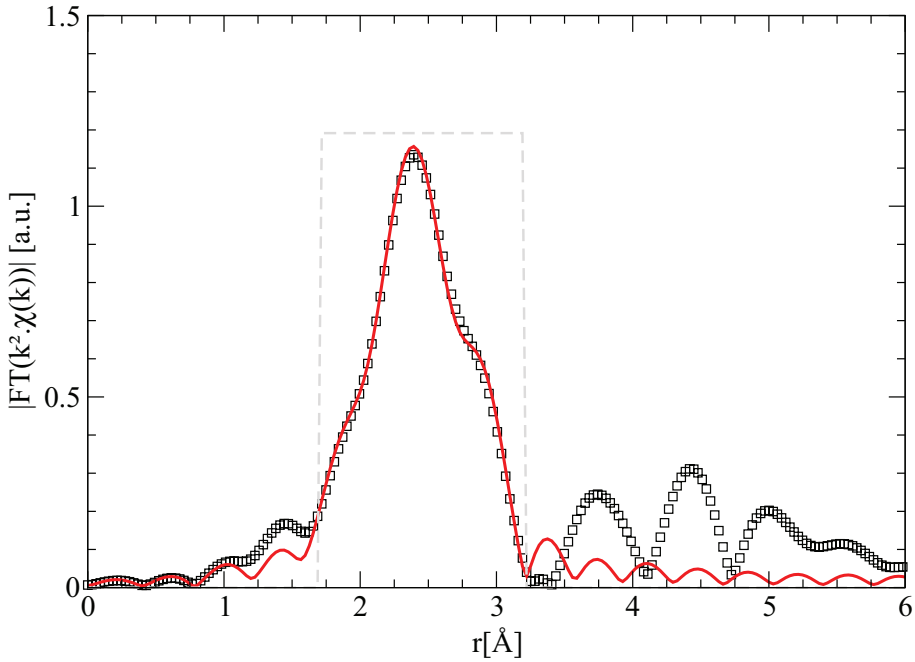

Figure 5.10: *Radial distribution (RDF) and one shell fitting for $CoPt_3$ at Pt L_3 edge. The window models the range of the first coordination shell.*

path	N	R [Å]	σ^2 [Å^2]	R-factor
Pt-Pt	10.4 ± 0.3	2.73 ± 0.01	0.006 ± 0.0003	0.002
Pt-Co	1.6 ± 0.3	2.70 ± 0.01	0.007 ± 0.0015	
Co-Pt	7.0 ± 0.4	2.69 ± 0.01	0.005 ± 0.0003	0.005
Co-Co	5.0 ± 0.4	2.67 ± 0.02	0.026 ± 0.003	

Table 5.6: *Modelling assimilation parameters of the first coordination shell at the Pt L_3 and Co K-edge of $CoPt_3$ nanoparticles.*

ticles. Moreover, the value of the σ^2, for the Co-Co path is high in comparison with other paths and the concentration of Co in the first coordiantion shell of Co K-edge differs from the Co concentration in the first coordination shell of Pt L_3-edge, 44 % and 23 %, respectively.

The need of the Co-Co scattering path and values of coordination numbers of both coordination shells show that the internal crystal structure of the $CoPt_3$ nanoparticles is not pure ordered fcc. Co atoms have Co neighbors in their first coordination shell which is an indication for Co-rich locations in the nanoparticles. The proposed structure model of a core of $CoPt_3$ fcc and a shell of Co assimilate pretty well with recognition out of TER-XSW studies. Assuming a thickness of about 4 Å as discussed in section 5.1.2, the volume fraction of the Co shell with respect to the whole nanoparticle valume can be calculated. Fig. 5.11 shows a core-shell nanoparticle structure with R_1 the radius of the whole particle and R_2 the radius of the core. Imagining the nanoparticle size to be about 80 Å (cf. 5.1.2 and 5.1.2) one can calculate the volume ratio to

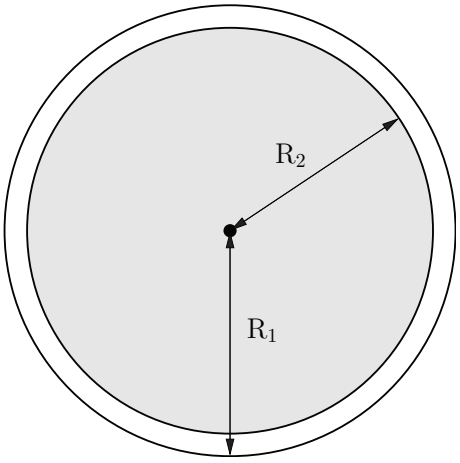

Figure 5.11: *Schematic view of a core-shell nanoparticle with R_1 radius of the whole particle and R_2 radius of the core.*

$$\frac{V_{shell}}{V_{total}} = 1 - \frac{V_{core}}{V_{total}} = 1 - \frac{R_2^3}{R_1^3} = 1 - \frac{(40-4)^3}{40^3} \approx 0.27.$$

One comes to the conclusion that about 27% of the volume of nanoparticles is in the shell part.

5.3 GISAXS Data Evaluation

Fig. 5.12 shows an island of $CoPt_3$ nanoparticles where two hexagonal close-packed domains are accented. The two domains are rotated 30 degrees relative to each other and are taken as sample bitmaps. For each sample bitmap, or kernel, the linear correlation coefficients for sub-bitmaps of the original image, which has the same dimensions are calculated. This yields a two-dimensional map of the correlation coefficient. Since sub-regions of the original bitmaps are compared, this map can be termed autocorrelation function (ACF). The ACFs reveal the repetitive features similar to the chosen kernels, respectively. Here indicate white spots high correlation and dark areas show little correlation. Fast Fourier transform (FFT) of the ACFs clearly show 6-fold symmetries, whereas the FFT of the original micrograph shows a ring. This is due to the different hcp domains rotated relative to each other. Summing up the FFT monographs of ACFs, the same result (a ring) is obtained. This legitimizes the assumption of hcp ordering.

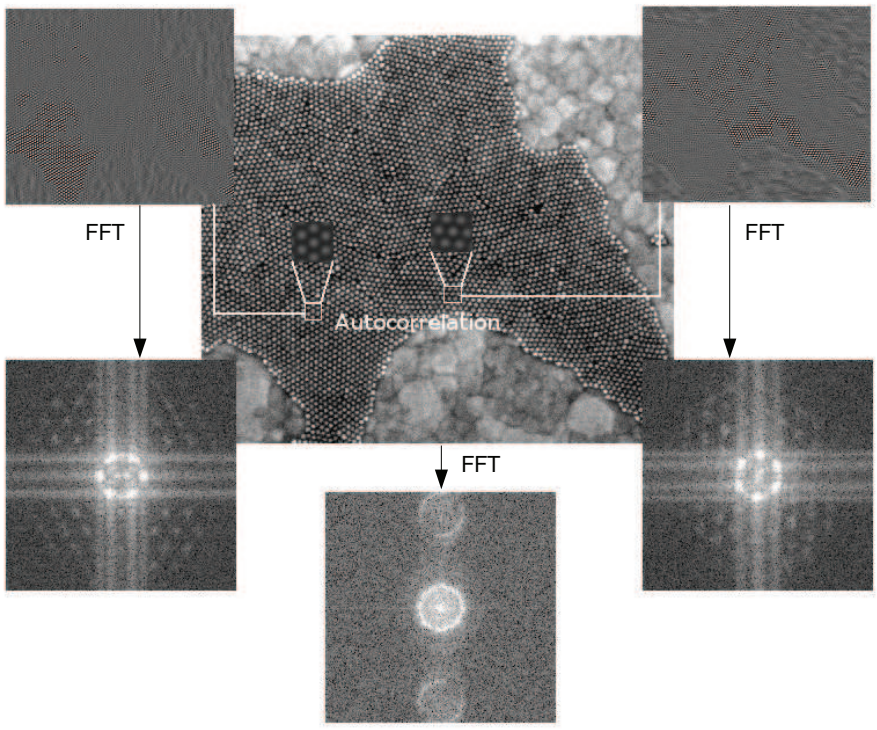

Figure 5.12: *SE monograph of a $CoPt_3$ nanoparticle island. Two hcp domains are chosen and the similar repetitive features are accented. FFTs of each of the ACFs as well as FFT of the original micrograph are also shown.*

In Fig. 5.13 a GISAXS pattern of the nanoparticle sample III is displayed as an example. Since the scattering contrast scales with the element number, it is evident that the heavy $CoPt_3$ nanoparticles dominate the small-angle scattering while the contribution of the SAM film is negligable. It is obvious from the image that the due to the relative long camera distance of ≈ 90 cm not all the information could have been collected. Therefore, the detector was shifted horizontally, such that $q_{\parallel} = 0$ is not positioned centrally and at least one second-order peak (in this case the one on the left hand side) is visible.

A line along $q_{\perp} = 0.6$ nm^{-1} is also visible on the picture, which indicates the position,

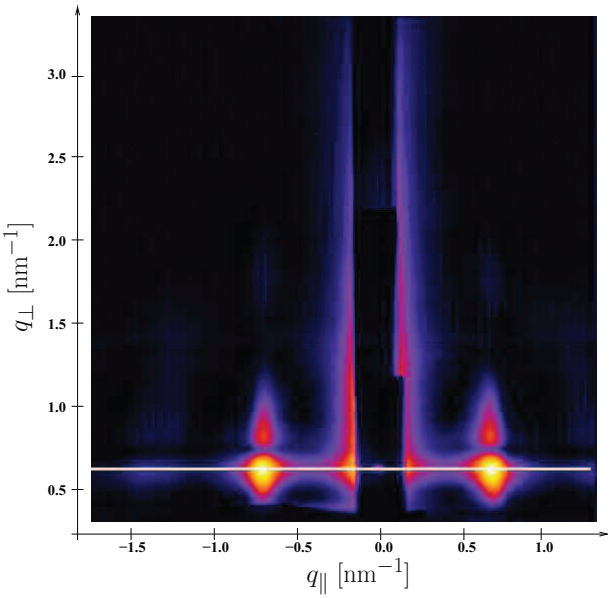

Figure 5.13: *GISAXS CCD image of sample III. The vertical black stripe indicates the position of the semi-transparent Al absorber. The white line along $q_{\perp} = 0.6$ nm^{-1} indicates the line profile extracting position.*

where the exit angle is equal to the critical angle of the reflecting layer, α_c (Yoneda peak [119]). This line profile at this specific position has been taken by all the samples investigated here.

Fig. 5.14 shows the the line profiles of all the investigated samples at the mentioned position. In order to determine the position and width of the first-order peaks left and right to $q_{\parallel} = 0$ we fitted Lorentzian functions to the peaks (cf. section 2.3) with the following general formula

$$y = \frac{a_0}{\pi a_1 \left[1 + \left(\frac{x - a_2}{a_1}\right)^2\right]},$$

with a_0 the heighth scaling parameter, a_1 the scaling parameter specifying the half-width at half-maximun (HWHM) of the Lorentzian function, and a_2 the location parameter, specifying the position of the peak. In case of hexagonal close packing of the nanoparticles one expects a peak at $q_{\parallel} = \frac{4\pi}{a}$ nm^{-1} beside the peak at $q_{\parallel} = \frac{4\pi}{\sqrt{3}a}$ nm^{-1}, with a lattice constant of the nanoparticles. The statistics for the second peak visible on the left hand

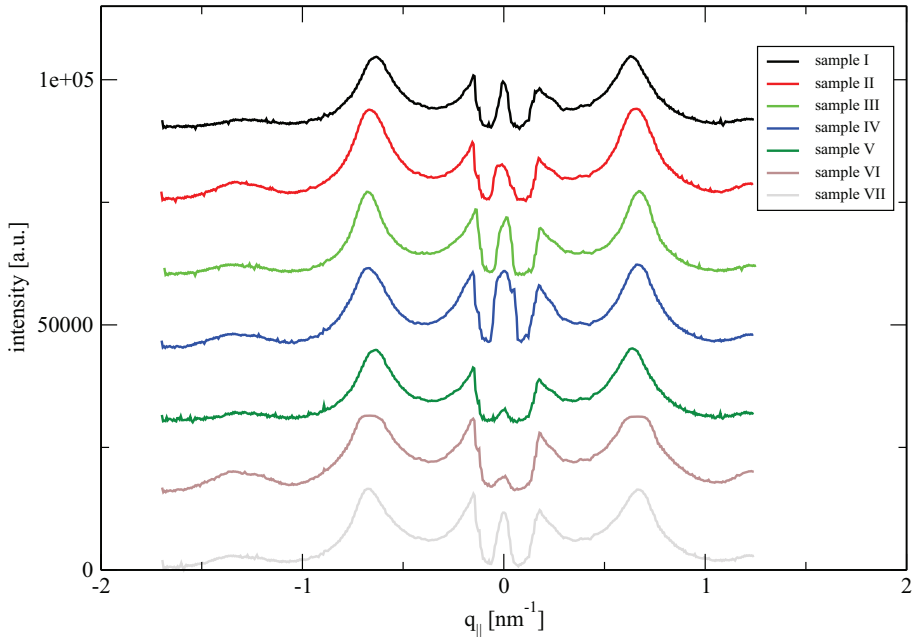

Figure 5.14: *Line profiles obtained from the GISAXS CCD images along* $q_\perp = 0.6\ nm^{-1}$

side is not good enough so that the both mentioned peaks can not be clearly resolved. Therefore, only the first-order scattering peaks are discussed in the following. The fit process had been performed individually for each of the two first-order peaks. Table 5.7 indicates the values obtained from the fitting processes together with the extracted $CoPt_3$ particle-particle distance, $\langle d \rangle$, and correlation length, Γ, values.

In section 2.3 we have defined the correlation length of the nanoparticle arrangement $\Gamma = 2\pi/\delta q$. We assume an error of 5 pixel in reading off the data from the CCD. This corresponds to an error of $\Delta q = \pm 5\text{px} \times 2.92\text{nm}^{-1}/497\text{px} \approx \pm 0.3\text{nm}^{-1}$. After a standard procedure of error propagation, calculated error of the particle-particle distance is given

Sample	$q_\parallel > 0$			$q_\parallel < 0$			$\langle d \rangle = \frac{2}{\sqrt{3}} \frac{4\pi}{a_2 - a_2'}$	$\Gamma = \frac{2\pi}{a_1 + a_1'}$
	a_0	a_1	a_2	a_0'	a_1'	a_2'		
I	5948	0.13	0.63	5781	0.13	-0.63	11.53 ± 0.55	24.06
II	7769	0.13	0.65	7679	0.13	-0.65	11.09 ± 0.53	23.98
III	5866	0.11	0.67	5744	0.11	-0.67	10.90 ± 0.52	28.19
IV	6929	0.13	0.66	6943	0.14	-0.66	10.96 ± 0.53	23.53
V	6144	0.13	0.63	5803	0.13	-0.63	11.46 ± 0.53	24.16
VI	9309	0.18	0.65	9234	0.18	-0.65	11.22 ± 0.53	17.61
VII	7485	0.15	0.65	7382	0.15	-0.65	11.16 ± 0.51	20.74

Table 5.7: *Values obtained from the fitting processes together with the extracted* $CoPt_3$ *particle-particle distance ,* $\langle d \rangle$*, and correlation length,* Γ*, values.*

by

$$\Delta\langle d\rangle = \pm \left\| -\frac{2}{\sqrt{3}} \frac{4\pi}{\Delta q_{\parallel}^2} \cdot \Delta q \right\| .$$

The $\langle d\rangle$ error values mentioned in the table are calculated as described and all $\pm \approx 0.5$ nm. It is evident from the values that the calculated distances, regarding the calculation errors, in the same range. This shows that the coverage grade of the nanoparticles virtually does not have any influence on the lateral particle-particle distance, as intuitively expected. This lateral distance is thus dominated by the ligand-ligand as well as possibly ligand-SAM interactions.

Regarding the calculated correlation lengths one can see that again the values are in the same range except for two samples III and VI. Sample VI has been prepared by dip coating with a speed higher than the optimum range given in 3.3.3. Observing the line profile, one can see that the first-order scattering peaks are wider than other cases, so that possibly two Lorentzian functions have to be fitted into it. A glimpse at Fig. 3.13, which belongs to sample VI, shows beside well-ordered islands of nanoparticles also domains with small numbers of nanoparticles coming together. By the latter, no hcp ordering is the case and the pure particle-particle distances ($\langle d\rangle = \frac{4\pi}{\Delta q_{\parallel}}$) are obtained. Hence, two different Lorentzian functions with two different peak positions.

The preparation condition of sample III is different from the rest as the sample was dipped into the solution with an angle of $\approx 30°$. Apparently this has led to better lateral ordering than in the case of perpendicular dipping.

We come to the conclusion that by keeping the preparation conditions in the given ranges noticed as optimal, the ordering quality of the nanoparticles in lateral direction remains more or less the same.

Chapter 6

Summary and Outlook

Controlling the distance of the particles and their ordering are important for electrical, magnetical or catalytic properties of the particle assemblies. In case of depositing the ligand terminated $CoPt_3$ nanoparticles on SAM functionalized Au bulk, the ordering and distance of these nanoparticles can be controlled, as these are mainly goverend by mutual interaction of ligands and SAM molecules. The coating processes, spin and dip coating, were optimized such that a good coverage control was achieved. Here, we could show the possibility of fabricating homogeneous monolayers of nanoparticles. Dip coating has turned out to be a more appropriate method for this purpose than spin coating.

The coverage of the nanoparticles has been obtained using XRR. These results were then compared with corresponding SEM analyses. It was obvious that within the specified error bars the determined coverages were the same. This is an indication for homogeneously covered layers. The same investigations and comparisons also show the monodispersity of the investigated nanoparticles. SEM is unable to resolve the vertical distances of the structures. This could theoretically be performed by tunneling electron microscopes. The disadvantage of this method is that it is destructive and also less appropriate for our case. Furthermore, it is known that the deposited nanoparticles investigated in this thesis are only weekly immobilized by van der Waals forces and are thus not particularly stable. Hence, the preparative steps needed for TEM investigations can easily lead to deformation of the structure to be investigated.

TER-XSW has turned to be a reliable method to resolve distances in vertical direction. We observed, for instance, that the nanoparticles are arranged in a specific distance to the substrate, and not directly on the surface, due to the interaction of the SAM layer and the ligand shells. Furthermore, we observed the fact that the quality of ordering in vertical direction is a function of coverage, meaning that the higher the coverage is the better is the ordering in vertical direction. The vertical ordering of the nanoparticles is modelled by a Gaussian distribution of the nanoparticle positions. In case of higher coverages, the standard deviation of the distribution turned out to be smaller and thus the distance value of single particles to the substrate is closer to the mean particle to substrate distance.

Mean particle to particle distances in lateral direction have been obtained using GISAXS. We came to the conclusion that contrary to vertical ordering the lateral ordering is not a function of coverage. Samples with different coverages and same in other aspects show the same lateral distances within a specified error bar. The distance in lateral direction is so

affected by ligand-ligand and possibly ligand-SAM interactions.

Beside the film morphology, the internal structures of the nanoparticles has also been investigated. While a homogeneous $CoPt_3$ fcc structure was expected, we observed that the nanoparticles exhibit a core-shell-like structure. TER-XSW investigations have shown that the shell is 4 Å thick and comprises mainly Co.

Complementary EXAFS investigations on $CoPt_3$ colloidal nanoparticle solutions have approved the core-shell structure proposed by TER-XSW. Furthermore, the core of the nanoparticles turned out to comply with the expected $CoPt_3$ fcc structure.

As often the case in the science, achievements fetch open questions. This constitutes the fascination of science. This thesis hasn't been an exception. There are still open questions and need of improvement in nanoparticle system fabrication as well as investigation methods, some of which are introduced in the following.

Beside spin and dip coating, the Langmuir-Blodgett method can be used to prepare nanoparticle films. Using this method, one might achieve better defined arrays of nanoparticles. Furthermore, by modifying the ligand shells of the nanoparticles as well as the SAM layer, it is possible to engineer the film in a way that ligand-SAM interactions are not merely goverend by non-polar van der Waals forces but also by polar or even covalent bounds. This might promote the stability of the nanoparticle film.

By designing a setup which enables both TER-XSW and GISAXS measurements, it would be possible to obtain both lateral and vertical information of an installed sample without moving it. This guarantees a thorough investigation and possibly a full 3D structural characterization.

For TER-XSW data evaluation we took a spherical model as basis. Yet for reflectivity data evaluation this was a layer model. The consistency of the latter rather easy model with the spherical one has been verified using iterative methods. Using distorted-wave Born approximation (DWBA) modelling of the nanoparticles leads to a unified model for both methods. Furthermore, DWBA is also advantageous for GISAXS experiments, as the structure factor of the nanoparticle film assembly and the form factor of the nanoparticles can be distinguished.

By TER-XSW measurements we always took fluorescence as the photo yield. Performing the experiments in UHV, it would also be possible to detect photoelectrons. This could then lead to more precise investigations as in this case information about chemical shifts and oxidation states can also be obtained. Furthermore, in-situ model catalysis under reaction conditions would be possible.

Appendix A

Dip Coater

The idea of making a dip coater was to have an alternative deposition technique. Having an alternative method beside spin coating for preparing nanoparticle films on substrate was the main reason for studying about the concept of dip coating. Soon we found out that the constructing concept of a dip coater is easy enough to be realized as a home-built system. The technical specification needed was that the machine is able to fulfill a precisely regular vertical motion with adjustable speeds ranging from $\approx 1 - 10$ mm/min (cf. section 3.3.3).

The motion generator is a four pole brushless DC-Servomotor from series BX4 SC of the Faulhaber group with a nominal voltage of 12 V, a recommended no-load maximum speed of 6000 rpm and an integrated PI regulator for speed control. The speed control takes place by the voltage applied to the system. This motor is delivered in combination with a planetary gearhead with nominal reduction ratio of 71:1. The torque of the motor is horizontally transfered to a steel wedge via a metric M6 screw. A metal slab, geometrically perpendicular to the horizontal edge of the wedge having one degree of freedom in vertical direction can be set into motion when the wedge moves back and forth (cf. Figs. A.1 and A.2). Hence, by fixing the sample at the ende of the metal slab, this can be moved vertically with a uniform adjustable speed. There is a pin available on the screw which releases the moving unit from the screw so that it can be manually positioned. This is for example useful at the immersion step of coating which has to be done all at once (cf. sections 1.3.3 and 3.3.3).

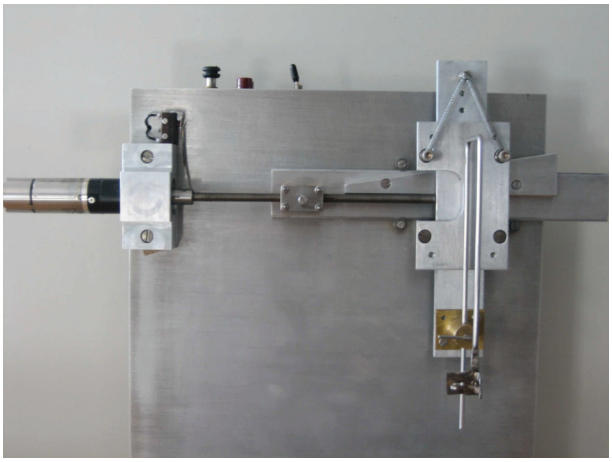

Figure A.1: *Photograph of the dip coater made in our group*

Each complete rotation of the M6 screw corresponds to a horizontal displacement of 1 mm. Having the reduction ration of 71:1 together with 6000 rpm in mind, the maximum horizontal displacement of the wedge per minute is about 80 mm. In order to find out the correspondence of vertical speed with the applied voltage, some calibration measurements

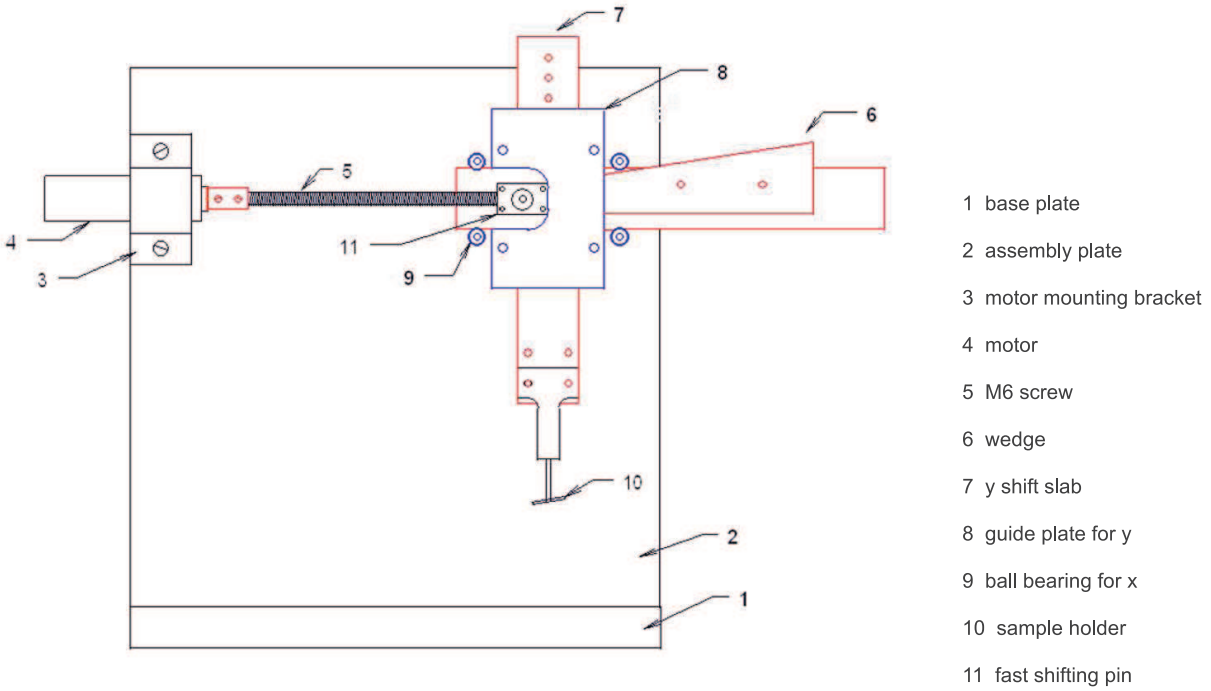

Figure A.2: *Schematic illustration of the dip coater*

were performed. Fig. A.3 provides the detailed calibration information which is used for setting the speed in dipping processes. For different voltages the vertical displacement in a minute was measured. It is obvious that the motor works linearly between $\approx 1 - 14$ mm/min. The frequency listed is a value read out of the motor control electronics.

voltage [V]	f [Hz]	start s [mm]	stop s [mm]	v [mm/min] Δs [mm]
0,5	23,5	27	27,3	0,3
0,6	34,5	27,3	28,3	1
0,7	45	28,3	29,3	1
0,8	56	29,3	30,55	1,25
0,9	66	30,55	32,15	1,6
1	79	32,15	34,05	1,9
1,1	89	34,05	36,05	2
1,2	101	36,05	38,5	2,45
1,3	111	38,5	41,05	2,55
1,4	123	41,05	44	2,95
1,5	134	27,25	30,3	3,05
1,6	144	30,3	33,6	3,3
1,7	156	33,6	37,25	3,65
1,8	167	37,25	41,15	3,9
1,9	179	41,15	45,25	4,1
2	189	28,05	32,35	4,3
2,2	210	32,35	37,2	4,85
2,4	234	37,2	42,6	5,4
2,6	255	42,6	45,4	5,6
2,8	277	26,35	32,7	6,35
3	300	32,7	39,55	6,85
3,2	322	26,75	34	7,25
3,4	344	34	41,8	7,8
3,6	366	26,5	35	8,5
3,8	388	35	43,9	8,9
4	409	26,4	35,85	9,45
4,2	433	35,85	45,7	9,85
4,4	455	27,35	37,7	10,35
4,6	477	28,85	39,7	10,85
4,8	499	30,45	42,05	11,6
5	521	28,5	40,6	12,1

voltage [V]	f [Hz]	start s [mm]	stop s [mm]	v [mm/min] Δs [mm]
5,2	542	28,5	40,9	12,4
5,4	563	29	41,85	12,85
5,6	587	30,4	43,8	13,4
5,8	608	28,75	42,7	13,95
6	630	28,15	42,6	14,45
6,2	652	27,6	42,6	15
6,4	651	27,55	42,6	15,05
6,6	653	28,15	43,1	14,95
6,8	654	28,7	43,65	14,95
7	654	28	42,85	14,85
7,2	654	28,65	43,65	15
7,4	654	27,3	42,25	14,95
7,6	654	27,85	43	15,15
7,8	654	27,55	42,65	15,1
8	654	27,5	42,55	15,05
8,5	654	27,4	42,4	15
9	654	28,45	43,4	14,95

Figure A.3: *voltage-speed correspondence of the dip coater*

Appendix B

refnc and *terxsw* Routines

In the following the implemented Fortran 77 codes for both routines together with comments are presented.

B.1 *refnc*

```
c********refnc routine for evaluation the reflectivity********

      SUBROUTINE FUNNY
      implicit none
      include   '/home/admin/for/refnc/lsinc1.f'



      real*8 thick(0:25),inter(0:25),beta(0:25),delta(0:25)
      real*8 k0,lambda,sigma,ymax,ymaxfalt
      real*8 reflex,r,theta,xoff,yoff,pi,back,rel
      real*8 walter,cross_section,probenlaenge
      integer num,i,jj,kk,pointc,pointp,rep,zz
      integer counter
      real*8 c, h,E0,slit_height,x_gain,y_gain
c************************
c     definitions
c************************
      pi=4.0*atan(1.0)

      pointc = param(1)                  ! Pointer Con-File
      pointp = param(2)                  ! Pointer Par-File

c*******pvalue(x) are all from the corresponding con

      c=2.998d+8                        !light velocity
      h=4.13567d-15                     !Planck constant
      E0=pvalue(1)                      !fixed photon energy
      lambda=c*h/E0*1.0d+10             !wave length
      k0     = 2.*pi/lambda             !wave vector
      y_gain=pvalue(2)
      x_gain=pvalue(3)
      xoff=pvalue(4)                    !x-axis correction
      yoff=pvalue(5)                    !y-axis correction
      num    = pvalue(6)                !number of layers on the substrate
      sigma=pvalue(7)*0.001             !resolution
      beta(0)=0.0                       !vacuum (air) absorption
      delta(0)=0.0                      !vacuum (air) dispersion
```

```
        inter(0)=0.0                    !vacuum (air) roughness

        do jj=1,num                     !reading in the layer information,
                                        !dispersion, absorption, roughness
                                        !and thickness respectively.
            kk          = 4*jj+13
            delta(jj)   = pvalue(kk)
            beta(jj)    = pvalue(kk+1)
            inter(jj)   = pvalue(kk+2)
            thick(jj)   = pvalue(kk+3)
        end do

        back            =pvalue(8)      !background
        rel             =pvalue(9)      !rel is multiplied by dispersion and
                                        !absorption of the NP layer, interpreted as coverage
        probenlaenge    =pvalue(10)     !sample length
        slit_height     =pvalue(11)     !vertical slit size
        rep             =pvalue(12)     !number of repetitions of
                                        !the layer structure given. (applied for e.g. DBRs)
        delta(num+1)    =pvalue(13)     !substrate dispersion
        beta(num+1)     =pvalue(14)     !substrate absorption
        inter(num+1)    =pvalue(15)     !substrate roughness
        thick(num+1)    =pvalue(16)     !substrate thickness (a very large number in
                                        !comparison, can be interpreted as infinity)

        if (back.le.0.0d0) back = 10.0d0
        back        = 10.0d0**(-back)           ! linear background

c*******listing the read in data

        jj=0
        counter=0
        zz=0
        write(*,*)'␣c␣,i␣,␣␣Delta␣␣␣␣␣,␣␣Beta␣␣␣␣␣␣,␣␣Dicke␣␣␣␣,␣␣sigma'
        write(*,11) counter,jj,delta(jj),beta(jj),thick(jj),inter(jj)
        do zz=0,rep
                do jj=1,num
                    counter=counter+1
                    write(*,11) counter,jj,delta(jj),beta(jj),thick(jj),inter(jj)
                end do
        end do
        counter=counter+1
        jj=num+1
        write(*,11) counter,jj,delta(jj),beta(jj),thick(jj),inter(jj)


11      format(I3,I3,2e12.5,2F12.4)

c**************************************
c       from hier intensity calculation
c**************************************
        ymax=0.0
        do jj=1,nyr,1
          theta=(xobs(jj)*x_gain-xoff)
          cross_section=sin(theta)*probenlaenge

            if (cross_section.lt.slit_height) then

                walter=cross_section/slit_height    !'walter' considers the fact
                                                    !that the sample turns into
                                                    !the beam and thus the
                                                    !intensity increases
            else
                walter=1.0
            end if

           r=Reflex(num,rep,thick,beta,delta,inter,theta,k0,rel)
           r=r*walter
```

```
            ycalc(jj)=y_gain*(r+back)-yoff

             if (ymax.lt.ycalc(jj)) then
                 ymax=ycalc(jj)
             end if

           write(*,*)jj,xobs(jj),theta,ycalc(jj)
     &     , ycalc(jj)-yobs(jj),weight(jj)
         end do

         ymaxfalt=1.0e-10
         if (sigma.ge.0.0002) then
             call falt(sigma)
         end if

         do i=1,nyr
             if (ymaxfalt.lt.ycalc(i)) then
               ymaxfalt=ycalc(i)
             end if
         end do

         do i=1,nyr
           ycalc(i)=ycalc(i)*ymax/ymaxfalt
         end do

         return
         end


c**********************************************************************
c
c        function kz !wavevector calculation function
c
c**********************************************************************
        complex*16 function kz(beta,delta,sinphi)
        real*8     sinphi,beta,delta
          kz=sqrt(sinphi*sinphi-2.0*delta-(0.0,2.0)*beta)
        return
        end

c**********************************************************************
c
c        function CSINH(Z) !auxiliary function
c
c**********************************************************************
        complex*16 function CSINH(Z)
        complex*16 z
          csinh=(exp(z)-exp(-z))*0.5
        return
        end

c**********************************************************************
c
c       REFLEXION (tanh) !roughness modelling after Beckmann-Spizzichino
c
c**********************************************************************

        complex*16 function reft(k1,k2,sigma)
        complex*16 k1,k2,csinh
        real*8 sigma,pi
          pi=atan(1.0)*4.0
          if (sigma.gt.0.1) then
            sig=sigma*sqrt(pi/8.)
          else
            sig=0.1
          end if
          reft=csinh(pi*sig*(k1-k2))/csinh(pi*sig*(k1+k2))
        return
```

```
      end

c**********************************************************************
c
c       REFLEXION  (Nevot-Croce) !roughness modelling after Nevot-Croce
c
c**********************************************************************

      complex*16 function refnc(k1,k2,sigma)
      complex*16 k1,k2
      real*8 sigma,pi
        pi=atan(1.0)*4.0
        refnc=(k1-k2)/(k1+k2)*exp(-2.0*k1*k2*(sigma**2))
      return
      end

c**********************************************************************

      function Reflex(num,rep,thick,beta,delta,inter,theta,k0,rel)
c******reflection calculation
c**********************************************************************

      real*8    thick(0:100),beta(0:100),delta(0:100),inter(0:100)
      integer   num,l,lm,rep
      complex*16   refnc,r,P,Rl,kz,f(0:100) !f(0:25)
      real*8       k0,theta,sinphi,reflex,rel
       complex*16 memory(100,2),Er(0:100),Et(0:100)
       lm=num*(rep+1)+1
      sinphi=sin(theta)
      beta(0)=0.0
      delta(0)=0.0

c*******(All following comments are based on  B.N.Dev et al. Phys.Rev. B 61. 8462. (2000))******

c*******Beginning from the substrate moving toward the 0th layer for X-value calculation

c*******substrate value calculations

       Rl=(0,0) !X substrate
       f(lm)=k0*kz(beta(lm),delta(lm),sinphi)   !kz substrate
       P     = exp(f(lm)*(0,-1)*thick(lm))       !a_j

       memory(lm+1,1)=Rl
       memory(lm+1,2)=P

c*******calculation of X_j and a_j for layers

       do l=lm-1,0,-1

            if (l.eq.1) then
               f(l) = k0*kz(beta(l)*rel,delta(l)*rel,sinphi) !for the case when no full coverage
                                                             !available on the surface (e.g. NPs)
            else
               f(l) = k0*kz(beta(l),delta(l),sinphi)         !k_j
            end if
               write(*,*) f(l+1),f(l)
         r = refnc(f(l),f(l+1),inter(l+1))
         write(*,*) 'refnc--->', l,r

         Rl      = (r+Rl*(P**2))/(1+r*Rl*(P**2))            !X_j
         P       = exp(f(l)*(0,-1)*thick(l))                !a_j

         memory(l+1,1)=Rl
         memory(l+1,2)=P

       end do

       Et(0)=1
```

```
      Er(0)=(memory(1,2)**2)*memory(1,1)

      reflex=(Er(0)/Et(0))*conjg(Er(0)/Et(0))

      return
      end

c*********************************************************************

      subroutine falt(sigma)

c*********************************************************************
      include '/home/admin/for/refnc/lsinc1.f'
      parameter(ianzahl=100)
      real*8 g(-ianzahl:ianzahl),dx,sigma,f(nym)
      integer i1,i2,i3
      dx=xobs(2)-xobs(1)
      call gauss(g,dx,sigma,ianzahl)
      do i1=1,nyr
        f(i1)=0.0
        i3=i1
        do i2=-ianzahl,ianzahl,1
           i3=i1+i2
          if ((i3.gt.0).and.(i3.le.nyr)) then
            f(i1)=f(i1)+ycalc(i3)*g(i2)
          else if (i3.gt.nyr) then
            f(i1)=f(i1)+ycalc(nyr)*g(i2)
          else
            f(i1)=f(i1)+ycalc(1)*g(i2)
          end if
        end do
      end do
      do i1=1,nyr
        ycalc(i1)=f(i1)
      end do

      return
      end


c*********************************************************************

      subroutine gauss(g,dx,sigma,anzahl)

c*********************************************************************

      integer i,anzahl
      real*8     dx,sigma,g(-anzahl:anzahl)
      pi=4.0*atan(1.0)
      do i=1,anzahl,1
        g(i)=exp(-0.5*(i*dx/sigma)**2)/sqrt(2*pi)/sigma
        g(-i)=g(i)
      end do
      g(0)=1.0/sqrt(2*pi)/sigma
      return
      end

c*********************************************************************

      subroutine window(g,dx,sigma,anzahl)

c*********************************************************************

      integer i,anzahl
      real*8     dx,sigma,g(-anzahl:anzahl)
      pi=4.0*atan(1.0)
      do i=1,anzahl,1
        if (i*dx.le.sigma) then
```

```
      g(i)=1.0
    else
      g(i)=0.0
    end if
    g(-i)=g(i)
  end do
  g(0)=1.0
  return
  end
```

B.2 terxsw

As the main issues of this routin concerning reading in the data and fitting procedures are the same as *refnc* we at this point merely introduce the yield function calculation procedure with its directly related subroutines.

```
c*****************************************************************

      function yield(number,repet,thick,beta,delta,inter,theta,k0,
     &                    ly,standdev)
c******yield calculation
c*****************************************************************

      real*8  thick(0:10),beta(0:10),delta(0:10),inter(0:10)
      integer number,l,lm,repet,ly
      complex*16  r,P,Rl,kz,refnc,f(0:100) !f(0:25)
      complex*16 t,refnct
      complex*16 memory(100,2),Er(0:100),Et(0:100)
      real*8      k0,theta,sinphi,zmax,zmin,mumin,mumax
      real*8  reflex,nu,standdev
      real*8  int_max, int_min,int_mu_min,int_mu_max
      integer n,n1, c,c1, cmax,c1max          !n: approvimation of nth grade
                                              !c, cmax: odd prefactor
      integer nmax,n1max                      !nmax: maximum grade of approximation
      real*8 m,m1, hn,hn1                     !m: mittelpunktsumme, !hn: step width
      real*8 v,w, tn,tm, tn1,tm1              !v: improvement between
                                              !the two trapezium tn and tn1
      real*8 vmin,wmin, midpoint, sig, pi,mures !gauss dist. sigma

      lm=number*(repet+1)+1
      sinphi=sin(theta)
      beta(0)=0.0
      delta(0)=0.0
      thick(0)=0.0

c*******(All following comments are based on B.N.Dev et al. Phys.Rev. B 61. 8462. (2000))******
      Rl=(0,0)
      f(lm)=k0*kz(beta(number+1),delta(number+1),sinphi)      !kz substrate
      P       = exp(f(lm)*(0,-1)*thick(number+1))             !a_j

      memory(lm+1,1)=Rl
      memory(lm+1,2)=P


      do l=lm-1,0,-1

            f(l) = k0*kz(beta(l),delta(l),sinphi)             !k_j
            r       = refnc(f(l),f(l+1),inter(l+1))
            Rl      = (r+Rl*(P**2))/(1+r*Rl*(P**2))           !X_j
            P       = exp(f(l)*(0,-1)*thick(l))               !a_j
            memory(l+1,1)=Rl
            memory(l+1,2)=P
      end do


      Et(0)=1
      Er(0)=(memory(1,2)**2)*memory(1,1)


      do l=1,lm

            r         = refnc(f(l-1),f(l),inter(l-1))
            t         = refnct(f(l-1),f(l),inter(l-1))
            Et(l)=(memory(l,2)*Et(l-1)*t)/(1+(memory(l+1,2)  !transmitted E-field
     &           **2)*memory(l+1,1)*r)
            Er(l)=(memory(l+1,2)**2)*memory(l+1,1)*Et(l)      !reflected E-field
```

```
        end do


        reflex=(Er(ly)/Et(ly))*conjg(Er(ly)/Et(ly))                !R
        nu=datan2(dimag(Er(ly)/Et(ly)),dble(Er(ly)/Et(ly)))        !nu

        write(*,*) 'reflex,nu---->',reflex,nu

c********integration routine

        tn1=0.0
        tm1=0.0
        pi=4.0*atan(1.0)
        sig=thick(ly)/standdev    !gauss dist sigma
        write(*,*) 'stand',sig
        midpoint=thick(ly)/2.0
        zmin=0.0-3.0*sig          !lower limit
        zmax=thick(ly)+3.0*sig    !upper limit
        vmin=0.0001
        wmin=0.0001
        n1max=3
        nmax=5
        n=0
        n1=0

        int_min=fcn(zmin,Et(ly),Er(ly),f(ly))
        int_max=fcn(zmax,Et(ly),Er(ly),f(ly))

        hn=(zmax-zmin)/(2.0**n)
        tn=hn*(int_min/2.0 + int_max/2.0)

        do n=0,nmax,1

                hn=(zmax-zmin)/(2.0**n)          !determining new step width
                cmax=(2**(n+1))-1
                m=0.0

                do c=1,cmax,2

c*******From here Gaussian distribution of middle point of particles***************
                        mumin=midpoint-3.0*sig
                        mumax=midpoint+3.0*sig
                        int_mu_min=halfcirc((zmin+c*hn/2.0)-mumin,thick(ly)/2.0)
     &                  *gaussdist(mumin,sig,midpoint)
                        int_mu_max=halfcirc((zmin+c*hn/2.0)-mumax,thick(ly)/2.0)
     &                  *gaussdist(mumax,sig,midpoint)
                        hn1=(mumax-mumin)/(2.0**n1)
                        tm=hn1*(int_mu_min/2.0 + int_mu_max/2.0)

                        do n1=0,n1max,1
                                m1=0.0
                                hn1=(mumax-mumin)/(2.0**n1)
                                c1max=(2**(n1+1))-1
                                        do c1=1,c1max,2

                                        m1=m1+hn1*halfcirc((zmin+c*hn/2.0)
     &                                  -(mumin+c1*hn1/2.0),thick(ly)/2.0)
     &                                  *gaussdist(mumin+c1*hn1/2.0
     &                                  ,sig,midpoint)

                                        enddo

                                tm1=(m1+tm)/2.0
                                w=abs(tm1-tm)
                                if(w.le.wmin) exit
                                tm=tm1
                        enddo
```

```
                        mures=tm1

c*******Gaussian distribution until here*****************************************

        m=m+hn*fcn(zmin+c*hn/2.0,Et(ly),Er(ly),f(ly))
     &                 *mures

                enddo

                  tn1= (m+tn)/2.0                !improved trapezoid calculation
                  v=abs(tn1-tn)                  !quality determination
                        if(v.le.vmin) exit       !if precise enough, exit and return value
                  tn=tn1
        enddo

        yield=tn1

        return
        end
c*********************************************************************
                function fcn(x,Et,Er,f)
c*******intensity function
c*********************************************************************
        real*8 fcn, x
        complex*16 Et, Er, f
        fcn=(Et*exp((0,-1)*f*x)+
     &           Er*exp((0,1)*f*x))
     &           *conjg(Et*exp((0,-1)*f
     &           *x)+Er*exp((0,1)*f
     &           *x))

        return
        end
c*********************************************************************
                function gaussdist(zet,sigma,mu)
c*******Gaussian distribution
c*********************************************************************
        real*8 zet,sigma,mu
        real*8 gaussdist
        real*8 pi
        pi=4.0*atan(1.0)
                gaussdist=(1.0/(sqrt(2*pi)*sigma))*
     &          exp(-0.5*(((zet-mu)/sigma)**2.0))

        return
        end
c*******************************t*************************************
                function halfcirc(muvar,radius)
c*******particle distribution defined in density distribution func.
c*********************************************************************
        real*8 halfcirc,muvar,radius
        real*8 pi
        pi=4.0*atan(1.0)
                halfcirc=(radius**2.0-muvar**2.0)/radius**2.0/4.0
        return
        end
c*********************************************************************
                function refnc(k1,k2,sigma)
c*******roughness modelling after Nevot-Croce
c*********************************************************************
       complex*16
       complex*16 k1,k2, refnc
       real*8 sigma,pi
         pi=atan(1.0)*4.0
         refnc=(k1-k2)/(k1+k2)*exp(-2.0*k1*k2*(sigma**2))
       return
       end
```

Bibliography

[1] G. Schmid, editor. *Nanoparticles: From Theory to Application* (Wiley-VCH, Weinheim, 2004).

[2] A. Fuhrer, S. Luscher, T. Ihn, T. Heinzel, K. Ensslin, W. Wegscheider, and M. Bichler. *Energy spectra of quantum rings.* Nature, **413**(6858), 822–825 (2001).

[3] M. Bayer, T. Gutbrod, J. P. Reithmaier, A. Forchel, T. L. Reinecke, P. A. Knipp, A. A. Dremin, and V. D. Kulakovskii. *Optical Modes in Photonic Molecules.* Physical Review Letters, **81**(12), 2582 (1998).

[4] M. C. Rogge, C. Fuhner, U. F. Keyser, R. J. Haug, M. Bichler, G. Abstreiter, and W. Wegscheider. *Combined atomic force microscope and electron-beam lithography used for the fabrication of variable-coupling quantum dots.* Applied Physics Letters, **83**(6), 1163–1165 (2003).

[5] S. Tarucha, D. G. Austing, T. Honda, R. J. van der Hage, and L. P. Kouwenhoven. *Shell Filling and Spin Effects in a Few Electron Quantum Dot.* Physical Review Letters, **77**(17), 3613 (1996).

[6] P. M. Petroff and S. P. DenBaars. *MBE and MOCVD growth and properties of self-assembling quantum dot arrays in III-V semiconductor structures.* Superlattices and Microstructures, **15**(1), 15 (1994).

[7] P. M. Petroff, A. Lorke, and A. Imamoglu. *Epitaxially Self-Assembled Quantum Dots.* Physics Today, **54**(5), 46 (2001).

[8] A. P. Alivisatos. *Semiconductor Clusters, Nanocrystals, and Quantum Dots.* Science, **271**(5251), 933–937 (1996).

[9] C. B. Murray, D. J. Norris, and M. G. Bawendi. *Synthesis and characterization of nearly monodisperse CdE (E = sulfur, selenium, tellurium) semiconductor nanocrystallites.* Journal of the American Chemical Society, **115**(19), 8706–8715 (1993).

[10] X. Peng, J. Wickham, and A. P. Alivisatos. *Kinetics of II-VI and III-V Colloidal Semiconductor Nanocrystal Growth: Focusing of Size Distributions.* Journal of the American Chemical Society, **120**(21), 5343–5344 (1998).

[11] B. Gehl, V. Aleksandrovic, M. Erbacher, B. Jürgens, M. Schürenberg, A. Kornowski, H. Weller, and M. Bäumer. *Ligand Exchange with Thiols: Effects on Composition*

and Morphology of Colloidal CoPt Nanoparticles. ChemPhysChem, **9**(6), 821–825 (2008).

[12] B. Gehl, A. Frömsdorf, V. Aleksandrovic, T. Schmidt, A. Pretorius, J. Flege, S. Bernstorff, A. Rosenauer, J. Falta, H. Weller, and M. Bäumer. *Structural and Chemical Effects of Plasma Treatment on Close-Packed Colloidal Nanoparticle Layers.* Advanced Functional Materials, **18**(16), 2398–2410 (2008).

[13] M. T. Franklin and K. J. Klabunde. *High-Energy Processes in Organometallic Chemistry*, chapter Living Colloidal Metal Particles from Solvated Metal Atoms: Clustering of Metal Atoms in Organic Media, 246–259 (American Chemical Society, Washington, D. C., 1987).

[14] M. Faraday. *The Bakerian Lecture: Experimental Relations of Gold (and Other Metals) to Light.* Philosophical Transactions: Royal Society of London, **147**, 145–153 (1857).

[15] J. M. Thomas. *Colloidal metals: past, present and future.* Pure and Applied Chemistry, **60**(10), 1517–1528 (1988).

[16] G. Schmid, editor. *Clusters and Colloids: From Theory to Applications* (VCH Verlag, Weinheim, 1994).

[17] W. Ostwald. *Systematik der Kolloide.* Kolloid-Zeitschrift, **1**, 291–331 (1907).

[18] R. A. Zsigmondy. *Colloids and the Ultramicroscope: A Manual of Colloid Chemistry and Ultramicroscopy (English Edition)* (Wiley, New York, 1909).

[19] R. A. Zsigmondy. *Properties of Colloids.* Nobel Lecture (1926).

[20] J. Turkevich, P. C. Stevenson, and J. Hillier. *A Study of the Nucleation and Growth Processes in the Synthesis of Colloidal Gold.* Discussions of the Farady Society, **11**, 55–75 (1951).

[21] R. M. Crooks, M. Zhao, L. Sun, V. Chechik, and L. K. Yeung. *Dendrimer-Encapsulated Metal Nanoparticles: Synthesis, Characterization, and Applications to Catalysis.* Accounts of Chemical Research, **34**(3), 181–190 (2001).

[22] M. Brust, M. Walker, D. Bethell, D. J. Schiffrin, and R. Whyman. *Synthesis of thiol-derivatised gold nanoparticles in a two-phase Liquid-Liquid system.* Journal of the Chemical Society, Chemical Communications, (7), 801–802 (1994).

[23] I. Lisiecki, F. Billoudet, and M. P. Pileni. *Syntheses of copper nanoparticles in gelified microemulsion and in reverse micelles.* Journal of Molecular Liquids, **72**(1-3), 251–261 (1997).

[24] N. Moumen, P. Veillet, and M. P. Pileni. *Controlled preparation of nanosize cobalt ferrite magnetic particles.* Journal of Magnetism and Magnetic Materials, **149**(1-2), 67–71 (1995).

[25] M. Aslam, L. Fu, M. Su, K. Vijayamohanan, and V. P. Dravid. *Novel one-step synthesis of amine-stabilized aqueous colloidal gold nanoparticles.* Journal of Materials Chemistry, **14**(12), 1795–1797 (2004).

[26] J. M. Slocik and R. Naik. *Biologically Programmed Synthesis of Bimetallic Nanostructures.* Advanced Materials, **18**(15), 1988–1992 (2006).

[27] D. Astruc, F. Lu, and J. R. Aranzaes. *Nanoparticles as Recyclable Catalysts: The Frontier between Homogeneous and Heterogeneous Catalysis.* Angewandte Chemie International Edition, **44**(48), 7852–7872 (2005).

[28] M. Haruta. *Catalysis of Gold Nanoparticles Deposited on Metal Oxides.* CATTECH, **6**(3), 102–115 (2002).

[29] H. Bönnemann, G. Braun, W. Brijoux, R. Brinkmann, A. S. Tilling, K. Seevogel, and K. Siepen. *Nanoscale colloidal metals and alloys stabilized by solvents and surfactants Preparation and use as catalyst precursors.* Journal of Organometallic Chemistry, **520**(1-2), 143–162 (1996).

[30] N. Toshima and T. Yonezawa. *Bimetallic nanoparticles-novel materials for chemical and physical applications.* New Journal of Chemistry, **22**(11), 1179–1201 (1998).

[31] B. D. Terris and T. Thomson. *Nanofabricated and self-assembled magnetic structures as data storage media.* Journal of Physics D: Applied Physics, **38**(12), R199–R222 (2005).

[32] A. N. Shipway, E. Katz, and I. Willner. *Nanoparticle Arrays on Surfaces for Electronic, Optical, and Sensor Applications.* ChemPhysChem, **1**(1), 18–52 (2000).

[33] A. F. Carlsson, M. Bäumer, T. Risse, and H. Freund. *Surface structure of Co–Pd bimetallic particles supported on Al_2O_3 thin films studied using infrared reflection absorption spectroscopy of CO.* The Journal of Chemical Physics, **119**(20), 10885–10894 (2003).

[34] H. Bönnemann and R. Richards. *Nanoscopic Metal Particles - Synthetic Methods and Potential Applications.* European Journal of Inorganic Chemistry, **2001**(10), 2455–2480 (2001).

[35] R. W. J. Scott, C. Sivadinarayana, O. M. Wilson, Z. Yan, D. W. Goodman, and R. M. Crooks. *Titania-Supported PdAu Bimetallic Catalysts Prepared from Dendrimer-Encapsulated Nanoparticle Precursors.* Journal of the American Chemical Society, **127**(5), 1380–1381 (2005).

[36] M. O. Nutt, J. B. Hughes, and M. S. Wong. *Designing Pd-on-Au Bimetallic Nanoparticle Catalysts for Trichloroethene Hydrodechlorination.* Environmental Science & Technology, **39**(5), 1346–1353 (2005).

[37] S. Maenosono, T. Okubo, and Y. Yamaguchi. *Overview of Nanoparticle Array Formation by Wet Coating.* Journal of Nanoparticle Research, **5**(1), 5–15 (2003).

[38] V. T. Aleksandrović. *$CoPt_3$ Nanoparticles: Ligand Exchange and Film Preparation.* Ph.D. thesis, University of Hamburg, Hamburg, Germany (2006).

[39] Y. Xia, B. Gates, Y. Yin, and Y. Lu. *Monodispersed Colloidal Spheres: Old Materials with New Applications.* Advanced Materials, **12**(10), 693–713 (2000).

[40] E. Slavcheva, V. Nikolova, T. Petkova, E. Lefterova, I. Dragieva, T. Vitanov, and E. Budevski. *Electrocatalytic activity of Pt and PtCo deposited on Ebonex by BH reduction.* Electrochimica Acta, **50**(27), 5444–5448 (2005).

[41] C. Kwak, T. Park, and D. J. Suh. *Effects of sodium addition on the performance of PtCo/Al2O3 catalysts for preferential oxidation of carbon monoxide from hydrogen-rich fuels.* Applied Catalysis A: General, **278**(2), 181–186 (2005).

[42] X. Zhang, K. Tsang, and K. Chan. *Electrocatalytic properties of supported platinum-cobalt nanoparticles with uniform and controlled composition.* Journal of Electroanalytical Chemistry, **573**(1), 1–9 (2004).

[43] A. Tomou, D. Gournis, I. Panagiotopoulos, Y. Huang, G. C. Hadjipanayis, and B. J. Kooi. *Weak ferromagnetism and exchange biasing in cobalt oxide nanoparticle systems.* Journal of Applied Physics, **99**(12), 123915–5 (2006).

[44] E. V. Shevchenko, D. V. Talapin, A. L. Rogach, A. Kornowski, M. Haase, and H. Weller. *Colloidal Synthesis and Self-Assembly of CoPt3 Nanocrystals.* Journal of the American Chemical Society, **124**(46), 11480–11485 (2002).

[45] E. V. Shevchenko, D. V. Talapin, H. Schnablegger, A. Kornowski, O. Festin, P. Svedlindh, M. Haase, and H. Weller. *Study of Nucleation and Growth in the Organometallic Synthesis of Magnetic Alloy Nanocrystals: The Role of Nucleation Rate in Size Control of CoPt3 Nanocrystals.* Journal of the American Chemical Society, **125**(30), 9090–9101 (2003).

[46] E. V. Shevchenko. *Monodisperse magnetic alloy nanocrystals and their superstructures.* Ph.D. thesis, University of Hamburg, Hamburg, Germany (2003).

[47] A. Kootte, C. Haas, and R. A. de Groot. *The electronic structure of ordered binary Co-Pt compounds.* Journal of Physics: Condensed Matter, **3**(9), 1133–1152 (1991).

[48] A. Ulman. *Formation and Structure of Self-Assembled Monolayers.* Chemical Reviews, **96**(4), 1533–1554 (1996).

[49] F. Schreiber. *Structure and growth of self-assembling monolayers.* Progress in Surface Science, **65**(5-8), 151–257 (2000).

[50] *Georg Albert Physikal Vapor Deposition.* http://georg-albert-pvd.de.

[51] C. D. Bain, E. B. Troughton, Y. T. Tao, J. Evall, G. M. Whitesides, and R. G. Nuzzo. *Formation of monolayer films by the spontaneous assembly of organic thiols from solution onto gold.* Journal of the American Chemical Society, **111**(1), 321–335 (1989).

[52] A. Cossaro, R. Mazzarello, R. Rousseau, L. Casalis, A. Verdini, A. Kohlmeyer, L. Floreano, S. Scandolo, A. Morgante, M. L. Klein, and G. Scoles. *X-ray Diffraction and Computation Yield the Structure of Alkanethiols on Gold(111).* Science, **321**(5891), 943–946 (2008).

[53] S. R. Holmes-Farley, C. D. Bain, and G. M. Whitesides. *Wetting of functionalized polyethylene film having ionizable organic acids and bases at the polymer-water interface: relations between functional group polarity, extent of ionization, and contact angle with water.* Langmuir, **4**(4), 921–937 (1988).

[54] L. H. Dubois and R. G. Nuzzo. *Synthesis, Structure, and Properties of Model Organic Surfaces.* Annual Review of Physical Chemistry, **43**, 437–463 (1992).

[55] L. Houssiau, M. Graupe, J. Colorado, H. I. Kim, T. R. Lee, S. S. Perry, and J. W. Rabalais. *Characterization of the surface structure of CH_3 and CF_3 terminated n-alkanethiol monolayers self assembled on Au111.* The Journal of Chemical Physics, **109**(20), 9134–9147 (1998).

[56] N. K. Devaraj, G. P. Miller, W. Ebina, B. Kakaradov, J. P. Collman, E. T. Kool, and C. E. D. Chidsey. *Chemoselective Covalent Coupling of Oligonucleotide Probes to Self-Assembled Monolayers.* Journal of the American Chemical Society, **127**(24), 8600–8601 (2005).

[57] J. P. Collman, A. Hosseini, T. A. Eberspacher, and C. E. D. Chidsey. *Selective Anodic Desorption for Assembly of Different Thiol Monolayers on the Individual Electrodes of an Array.* Langmuir, **25**(11), 6517–6521 (2009).

[58] N. Shukla, J. Ahner, and D. Weller. *Dip-coating of FePt nanoparticle films: surfactant effects.* Journal of Magnetism and Magnetic Materials, **272-276**(Supplement 1), E1349–E1351 (2004).

[59] M. J. Bedzyk. *Encyclopedia of Condensed Matter Physics*, volume 6, chapter Scattering: X-Ray Standing Wave Techniques, 330–341 (Elsevier,Oxford, 2005).

[60] J. Zegenhagen. *Surface structure determination with X-ray standing waves.* Surface Science Reports, **18**, 202–271 (1993).

[61] J. M. Bloch, M. Sansone, F. Rondelez, D. G. Peiffer, P. Pincus, M. W. Kim, and P. M. Eisenberger. *Concentration Profile of a Dissolved Polymer near the Air-Liquid Interface: X-Ray Fluorescence Study.* Physical Review Letters, **54**, 1039 (1985).

[62] M. J. Bedzyk, G. M. Bommarito, and J. S. Schildkraut. *X-ray standing waves at a reflecting mirror surface.* Physical Review Letters, **62**, 1376 (1989).

[63] D. K. G. de Boer. *Glancing-incidence x-ray fluorescence of layered materials.* Physical Review B, **44**, 498 (1991).

[64] U. Weisbrod, R. Gutschke, J. Knoth, and H. Schwenke. *X-ray induced fluorescence spectrometry at grazing incidence for quantitative surface and layer analysis.* Fresenius' Journal of Analytical Chemistry, **341**, 83–86 (1991).

[65] M. Caffrey and J. Wang. *Internal and interfacial structure of membranes studied using X-ray standing waves.* Faraday Discussions, **94**, 283–293 (1992).

[66] J. Kawai, M. Takami, M. Fujinami, Y. Hashiguchi, S. Hayakawa, and Y. Gohshi. *A numerical simulation of total reflection X-ray photoelectron spectroscopy (TRXPS).* Spectrochimica Acta Part B: Atomic Spectroscopy, **47**, 983–991 (1992).

[67] S. Kirchner, J. Wang, Z. Yin, and M. Caffrey. *X-ray standing waves as probes of surface structure: Incident beam energy effects.* Journal of Applied Physics, **78**, 2311–2322 (1995).

[68] M. J. Bedzyk, D. Bilderback, J. White, H. D. Abruna, and M. G. Bommarito. *Probing electrochemical interfaces with x-ray standing waves.* The Journal of Physical Chemistry, **90**, 4926–4928 (1986).

[69] M. Bedzyk, D. Bilderback, G. Bommarito, M. Caffrey, and J. Schildkraut. *X-ray standing waves: a molecular yardstick for biological membranes.* Science, **241**, 1788–1791 (1988).

[70] J. Wang, M. J. Bedzyk, T. L. Penner, and M. Caffrey. *Structural studies of membranes and surface layers up to 1,000 A thick using X-ray standing waves.* Nature, **354**, 377–380 (1991).

[71] J. Wang, M. Bedzyk, and M. Caffrey. *Resonance-enhanced x-rays in thin films: a structure probe for membranes and surface layers.* Science, **258**, 775–778 (1992).

[72] J. Wang, M. Caffrey, M. J. Bedzyk, and T. L. Penner. *Direct Profiling and Reversibility of Ion Distribution at a Charged Membrane/Aqueous Interface: An X-ray Standing Wave Study.* Langmuir, **17**, 3671–3681 (2001).

[73] B. N. Dev. *Synchrotron X-radiation in studies of layered and self-assembled structures.* Radiation Physics and Chemistry, **70**, 525–533 (2004).

[74] J. A. Libera, R. W. Gurney, S. T. Nguyen, J. T. Hupp, C. Liu, R. Conley, and M. J. Bedzyk. *X-ray Nanoscale Profiling of Layer-by-Layer Assembled Metal/Organophosphonate Films.* Langmuir, **20**, 8022–8029 (2004).

[75] H. Hönl. *Atomic factor for x-rays as a problem of the dispersion theory (K-Schale).* Annalen der Physik, **18**(6), 625–655 (1933).

[76] M. Born and E. Wolf. *Principles of Optics* (Cambridge University Press, 2003).

[77] B. L. Henke, E. M. Gullikson, and J. C. Davis. *X-ray Interactions: Photoabsorption, Scattering, Transmission, and Reflection: at E = 50-30,000 eV, Z = 1-92.* Atomic Data and Nuclear Data Tables, **54**, 181–342 (1993).

[78] M. Tolan. *X-ray Scattering from Soft-Matter Thin Films*, volume 148 of *Springer Tracts in Modern Physics* (Springer, Berlin Heidelberg, 1999).

[79] P. Croce and L. Névot. *Étude des couches minces et des surfaces par réflexion rasante, spéculaire ou diffuse, de rayons X.* Revue de Physique Appliquée, **11**, 13 (1976).

[80] L. Névot and P. Croce. *Caractérisation des surfaces par réflexion rasante de rayons X. Application à l'étude du polissage de quelques verres silicates.* Revue de Physique Appliquée, **15**, 19 (1980).

[81] L. G. Parratt. *Surface Studies of Solids by Total Reflection of X-Rays.* Physical Review, **95**, 359 (1954).

[82] R. Zhang, R. Itri, and M. Caffrey. *Membrane Structure Characterization Using Variable-Period X-Ray Standing Waves.* Biophys. J., **74**, 1924–1936 (1998).

[83] B. N. Dev, A. K. Das, S. Dev, D. W. Schubert, M. Stamm, and G. Materlik. *Resonance enhancement of x rays in layered materials: Application to surface enrichment in polymer blends.* Physical Review B, **61**, 8462 (2000).

[84] S. K. Ghose and B. N. Dev. *X-ray standing wave and reflectometric characterization of multilayer structures.* Physical Review B, **63**, 245409 (2001).

[85] S. K. Ghose, B. N. Dev, and A. Gupta. *Resonance enhancement of x-rays and fluorescence yield from marker layers in thin films.* Physical Review B, **64**, 233403 (2001).

[86] D. R. Lee, A. Hagman, X. Li, S. Narayanan, J. Wang, and K. R. Shull. *Perturbation to the resonance modes by gold nanoparticles in a thin-film-based x-ray waveguide.* Applied Physics Letters, **88**, 153101–3 (2006).

[87] W. Lin, T.-L. Lee, P. F. Lyman, J. Lee, M. J. Bedzyk, and T. J. Marks. *Atomic Resolution X-ray Standing Wave Microstructural Characterization of NLO-Active Self-Assembled Chromophoric Superlattices.* Journal of the American Chemical Society, **119**, 2205–2211 (1997).

[88] P. Fenter, F. Schreiber, L. Berman, G. Scoles, P. Eisenberger, and M. J. Bedzyk. *On the structure and evolution of the buried S/Au interface in self-assembled monolayers: X-ray standing wave results.* Surface Science, **412-413**, 213–235 (1998).

[89] H. Jin, C. R. Kinser, P. A. Bertin, D. E. Kramer, J. A. Libera, M. C. Hersam, S. T. Nguyen, and M. J. Bedzyk. *X-ray Studies of Self-Assembled Organic Monolayers Grown on Hydrogen-Terminated Si(111).* Langmuir, **20**, 6252–6258 (2004).

[90] *Photon Cross Section Database of National Institute of Standards and Technology, USA.* http://www.nist.gov/physlab/data/xcom/index.cfm.

[91] I. Arcon, B. Mirtic, and A. Kodre. *Determination of Valence States of Chromium in Calcium Chromates by Using X-ray Absorption Near-Edge Structure (XANES) Spectroscopy.* Journal of the American Ceramic Society, **81**, 222–224 (1998).

[92] J. Stöhr. *NEXAFS Spectroscopy* (Springer, Berlin, 2005).

[93] M. Newville. *Fundamentals of XAFS*. http://xafs.org/Tutorials (2004).

[94] E. A. Stern, D. E. Sayers, and F. W. Lytle. *Extended x-ray-absorption fine-structure technique. III. Determination of physical parameters*. Physical Review B, **11**, 4836 (1975).

[95] D. C. Koningsberger and R. Prins, editors. *X-Ray Absorption: Principles, Applications, Techniques of EXAFS, SEXAFS and XANES*, volume 92 of *Chemical Analysis* (Wiley & Sons Ltd, West Sussex, England, 2005).

[96] J. Falta and T. Möller, editors. *Forschung mit Synchrotronstrahlung*, chapter Röntgenbeugungsmethoden (Vieweg+Teubner, 2010).

[97] J. R. Levine, J. B. Cohen, Y. W. Chung, and P. Georgopoulos. *Grazing-incidence small-angle X-ray scattering: new tool for studying thin film growth*. Journal of Applied Crystallography, **22**(6), 528–532 (1989).

[98] J. R. Levine, J. Cohen, and Y. Chung. *Thin film island growth kinetics: a grazing incidence small angle X-ray scattering study of gold on glass*. Surface Science, **248**(1-2), 215–224 (1991).

[99] S. K. Sinha, E. B. Sirota, S. Garoff, and H. B. Stanley. *X-ray and neutron scattering from rough surfaces*. Physical Review B, **38**(4), 2297 (1988).

[100] M. Rauscher, R. Paniago, H. Metzger, Z. Kovats, J. Domke, J. Peisl, H. Pfannes, J. Schulze, and I. Eisele. *Grazing incidence small angle x-ray scattering from free-standing nanostructures*. Journal of Applied Physics, **86**(12), 6763–6769 (1999).

[101] M. Schmidbauer. *X-ray Diffuse Scattering from Self-Organized Mesoscopic Semiconductor Structures* (Springer, Berlin Heidelberg, 2004).

[102] R. Lazzari. *IsGISAXS: a program for grazing-incidence small-angle X-ray scattering analysis of supported islands*. Journal of Applied Crystallography, **35**, 406 (2002).

[103] J. Flege, T. Schmidt, V. Aleksandrovic, G. Alexe, T. Clausen, B. Gehl, A. Kornowski, S. Bernstorff, H. Weller, and J. Falta. *Grazing-incidence small-angle X-ray scattering investigation of spin-coated $CoPt_3$ nanoparticle films*. Nuclear Instruments and Methods in Physics Research Section B: Beam Interactions with Materials and Atoms, **246**(1), 25–29 (2006).

[104] G. Albert. *Herstellung und Characterisierung polykristalliner Goldschichten zur Verwendung in der Nanolithographie*. Master's thesis, Ruprecht-Karls-Universität in Heidelberg (2001).

[105] F. E. Christensen, F. Besenbacher, J. Garnaes, E. Laegsgaard, and I. Stensgaard. *Scanning tunneling microscopy studies of thin foil x-ray mirrors*. Optical Engineering, **29**(6), 666–671 (1990).

[106] D. M. Collard and M. A. Fox. *Use of electroactive thiols to study the formation and exchange of alkanethiol monolayers on gold.* Langmuir, **7**(6), 1192–1197 (1991).

[107] G. E. P. Box, W. G. Hunter, J. S. Hunter, and W. G. Hunter. *Statistics for Experimenters: An Introduction to Design, Data Analysis, and Model Building* (John Wiley & Sons, 1978).

[108] *Image Processing and Analysis in Java.* http://rsbweb.nih.gov/ij/.

[109] Die Merck-Gruppe. *Sicherheitsdatenblatt-Hexan* (2006).

[110] Die Merck-Gruppe. *Sicherheitsdatenblatt-Toluol* (2006).

[111] J. Als-Nielsen and D. McMorrow. *Elements of Modern X-Ray Physics* (John Wiley & Sons, 2001).

[112] J. Falta and T. Möller, editors. *Forschung mit Synchrotronstrahlung* (Vieweg+Teubner, 2010).

[113] HASYLAB, DESY, web presence, Hamburg, Germany. *Beamline: E2 (RÖMO I), Instrument Specification* (2010).

[114] J. Falta and T. Möller, editors. *Forschung mit Synchrotronstrahlung*, chapter Synchrotronstrahlung: Erzeugung, Eigenschaften und Instrumentierung (Vieweg+Teubner, 2010).

[115] W. R. Leo. *Techniques for nuclear and particle physics experiments* (Springer, 1994).

[116] HASYLAB, DESY, web presence, Hamburg, Germany. *Beamline: C (CEMO), Instrument Specification* (2010).

[117] Elettra, web presence, Trieste, Italy. *Beamline: SAXS, Instrument Specification* (2010).

[118] *Rat Tail Positions.* http://www.esrf.eu/UsersAndScience/Experiments/CRG/BM26/SaxsWaxs/Rattail (2008).

[119] Y. Yoneda. *Anomalous Surface Reflection of X Rays.* Physical Review, **131**(5), 2010 (1963).

[120] FEI Company. *xT Nova Nanolab User's Manual*, 5th edition (2006).

[121] B. Ravel and M. Newville. *ATHENA, ARTEMIS, HEPHAESTUS: data analysis for X-ray absorption spectroscopy using IFEFFIT.* Journal of Synchrotron Radiation, **12**(4), 537–541 (2005).

[122] M. Newville. *IFEFFIT: interactive XAFS analysis and FEFF fitting.* Journal of Synchrotron Radiation, **8**(2), 322–324 (2001).

[123] S. I. Zabinsky, J. J. Rehr, A. Ankudinov, R. C. Albers, and M. J. Eller. *Multiple-scattering calculations of x-ray-absorption spectra.* Physical Review B, **52**, 2995 (1995).

[124] E. Gullikson. *X-Ray Interactions With Matter.* http://henke.lbl.gov/opticalconstants/ (2008).

List of Publications

Meeting and Conference Contributions

- *Revealing the internal structure and ordering of Pt-containing colloidal bimetallic nanoparticles by synchrotron based X-ray techniques*– SRMS/MEDSI 2010, Oxford, UK, Oral Presentation

- *Multi-scale structural characterization of colloidal nanoparticle films* – E-MRS 2009 Spring Meeting, Symposium R: "X-ray Techniques for Advanced Materials, Nanostructures and Thin Films: from Laboratory Sources to Synchrotron Radiation", Strasbourg, France, Oral Presentation

- *TER-XSW & XRR investigation of $CoPt_3$ nanoparticle films on Si substrates*– DPG Spring Meeting 2008, Berlin, Germany, Oral Presentation

- *The structure of colloidal thin films*– Hymade Material Design Kick-off Meeting 2007, Bremen, Germany, Oral Presentation

- *Multi-Scale Structural Characterization of colloidal nanoparticle films*– Hasylab Users' Meeting 2009, Hamburg, Germany, Poster

- *Structural Characterisation of $CoPt_3$ nanocolloidal particles on Si substrates*– Hasylab Users' Meeting 2008, Hamburg, Germany, Poster

Publications in Peer Reviewed Journals

- A. Zargham, T. Laurus, M. Sauerbrey, E. Piskorska-Hommel, Th. Schmidt, J.I. Flege, Sarah Röhe, M. Bäumer and J. Falta, *Exposing the Internal Structure of Supported Bimetallic Nanoparticles and Their Vertical Ordering Using Synchrotron based X-ray Techniques*, in prep. (2010).

- A. Zargham, Th. Schmidt, J.I. Flege, M. Sauerbrey, R. Hildebrand, S. Röhe, M. Bäumer, and J. Falta, *On Reveling the Vertical Structure of Nanoparticle*

Films with Elemental Resolution: A Total External Reflection X-ray Standing Waves Study, Nucl. Instr. Meth. B., **268**(3-4), 325–328 (2010).

- S. Figge, J. Dennemarck, T. Aschenbrenner, A. Zargham, and D. Hommel, *Wave Guide Optimization for Homoexpitaxial Laser Diodes*, Physica Status Solidi (c), **4**(7), 2842–2845 (2007).

Others

- A. Zargham, Th. Schmidt, R. Hildebrand, S. Röhe, M. Bäumer, and J. Falta, *Characterization of $CoPt_3$ colloidal nanoparticle film on functionalized Au coated Si substrates*, Hasylab Annual Report, (2009)

- A. Zargham, T. Laurus, E. Piskorska-Hommel, Th. Schmidt, J. I. Flege, S. Röhe, M. Bäumer, and J. Falta, *XAFS study of local atomic structure of Pt containing bimetallic nanoparticles*, Hasylab Annual Report, (2008)

- A. Zargham, Th. Schmidt, R. Hildebrand, S. Röhe, M. Bäumer, and J. Falta, *Ordering of $CoPt_3$ nanoparticles on organic self-assembled monolayers*, Hasylab Annual Report, (2008)
- T. Laurus, E. Piskorska-Hommel, A. Zargham, J. I. Flege, S. Röhe, M. Bäumer, and J. Falta, *XAFS study of local atomic structure in $CoPt_3$ nanoparticles*, Hasylab Annual Report, (2008)

- . Zargham, Th. Schmidt, R. Hildebrand, B. Gehl , M. Bäumer and J. Falta, *Structural Characterisation of $CoPt_3$ nanocolloidal particles on Si substrates*, Hasylab Annual Report, p. 1205 (2007)

- R. Hildebrand, Th. Schmidt, A. Zargham, M. Speckmann, C. Kruse, D. Hommel and J. Falta, *XRR investigations of II-VI and III-nitride based DBR-structures, multilayers and superlattices*, Hasylab Annual Report, p. 1237 (2007)

- M. Speckmann, Th. Schmidt, R. Hildebrand, A. Zargham, and J. Falta, *XSW analysis of Ga adsorption on vicinal silicon surfaces*, Hasylab Annual Report, p. 1239 (2007)

Curriculum Vitae

personal information

Name: Ardalan Zargham

Date of birth: March 22, 1980

Place of birth: Tehran, Iran

Nationality: German, Iranian

Education

Apr. 2007 to present: University of Bremen

- Research assistant and Ph.D. student

Mar. 2007: University of Bremen and University of Kaiserslautern

- Dipl.-Ing., Electrical and Computer Engineering
- Thesis Topic: Opto-Electrical Characterization of short wavelength Semiconductor Laser Diodes

Oct. 2001 to Mar. 2007: University of Kaiserslautern

- Diplom course in Electrical Engineering

Jun. 1998: High school, Tehran, Iran

- Mathematics and Physics Branch